# Study of Reconstruction Methods for a Time Projection Chamber with GEM Gas Amplification System

Diploma Thesis
of
Ralf Diener
from Saarbrücken

submitted to the
Institute of Experimental Physics
University of Hamburg

prepared at
Deutsches Elektronen Synchrotron (DESY), Hamburg

May 2006

**Abstract**

A new $e^+e^-$ linear collider with an energy range up to 1 TeV is planned in an international collaboration: the International Linear Collider (ILC). This collider will be able to do precision measurements of the Higgs particle and of physics beyond the Standard Model. In the Large Detector Concept (LDC) – which is one proposal for a detector at the ILC – a Time Projection Chamber (TPC) is foreseen as the main tracking device.
To meet the requirements on the resolution and to be able to work in the environment at the ILC, the application of new gas amplification technologies in the TPC is necessary. One option is an amplification system based on Gas Electron Multipliers (GEMs). Due to the – in comparison with older technologies – small spatial width of the signals, this technology poses new requirements on the readout structures and the reconstruction methods.

In this work, the performance and the systematics of different reconstruction methods have been studied, based on data measured with a TPC prototype in high magnetic fields of up to 4 T and data from a Monte Carlo simulation. The latest results of the achievable point resolution are presented and their limitations have been investigated.

**Zusammenfassung**

Im Rahmen einer internationalen Kollaboration wird ein neuer $e^+e^-$ Linearbeschleuniger mit einer Schwerpunktsenergie bis zu 1 TeV geplant, der International Linear Collider (ILC). An diesem Beschleuniger werden Präzisionsmessungen des Higgs-Teilchens und von Physik jenseits des Standardmodells möglich sein. Im Large Detector Concept (LDC) – einem Detektorvorschlag für den ILC – ist eine Zeit-Projektions-Kammer als zentrale Spurkammer vorgesehen.
Um die Ansprüche an die Punktauflösung zu erfüllen und um im Umfeld des ILC arbeiten zu können, ist die Verwendung einer neuen Technologie zur Gas-Verstärkung in der TPC notwendig. Eine Option ist ein auf Gas Electron Multipliern (GEM) basiertes Verstärkungssystem. Die im Vergleich zu früheren Techniken räumlich sehr kleinen Signalbreiten dieser Technik stellen neue Anforderungen an die Auslesestruktur und die Rekonstruktionsmethoden.

Im Rahmen dieser Arbeit wurden die Leistungsfähigkeit und die Systematiken verschiedener Rekonstruktionsmethoden untersucht, basierend auf Messungen mit einer TPC-Testkammer in sehr starken Magnetfeldern bis zu 4 T und Daten von einer Monte-Carlo-Simulation. Die neuesten Ergebnisse der erreichbaren Punktauflösung werden präsentiert und ihre Beschränkungen untersucht.

# Contents

# Chapter 1

# Introduction

## 1.1 Particle Physics: a Brief History

The subjects of elementary particle (or *high energy*) physics are - as the name implies - the elementary particles and their interactions.

In ancient Greece, philosophers believed in indivisible particles as the constituents of matter. But it took about 2000 years before these speculations could be put on a solid scientific ground and our present idea of the basic constituents of our world has been developed (see Figure 1.1). This happened in the course of the following events and discoveries (and of course many other):

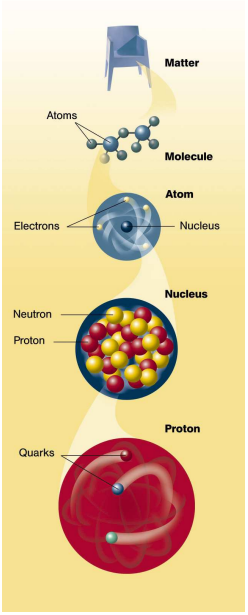


Figure 1.1: From matter to leptons and quarks.

Modern particle physics started in 1897 when J. J. Thomson discovered the *electron* ($e^-$), which was the first experimental sight of an elementary particle. At least, today we believe that the electron is an *elementary* particle, because there is no sign that the electron is divisible; but there is also no proof that it is indivisible.

The second elementary particle that was discovered was the *photon* ($\gamma$), which is the mediator of the electromagnetic force and the particle composing electromagnetic radiation (e.g. visible light). The important steps that led to its discovery and description were Planck's work on blackbody radiation (1900), Einstein's theory about the photo-electric effect (1905) and Compton's scattering experiment in 1923. The scattering experiments of Rutherford (1911), followed by the atom model of Bohr (1914) and Chadwicks discovery of the

*neutron* (1932) pushed forward the understanding of the substructure of the atom[1] and introduced the *proton* ($p$) and the *neutron* ($n$) as the particles in the atomic nucleus. These two particles together with the electron in the atomic shell are the constituents of the atoms: the matter that our world is made of. It seemed like the job was basically done and that all particles required to explain what matter is made of were on the table.
But this wasn't the end of the story: there was for example Pauli's suggestion of the existence of a *neutrino* (which he called *neutron*) for the reason of energy conservation in beta decays and Fermi's decay theory which incorporated this suggestion. Fermi called the particle *neutrino* ($\nu$). In fact it is an *anti*neutrino, but in the thirties the concept of antiparticles was not yet developed (see below).
Yukawa's theory of the strong force, the discovery of the *mesons* - by Anderson, Neddermeyer and Street, Stevenson (1937) - and of the *muon* ($\mu^-$) by Powel (1947) introduced new particles. Dirac theories from 1927 contained the idea of negative energy states and in the forties Stückelberg and Feynman interpreted these negative energy states as antiparticles.[2] The *positron* - the antiparticle partner of the electron - was detected in 1932 by Anderson. And even more particles showed up: in 1947 the first sight of the *Kaon* ($K^0$) was made by Rochester and Butler and in 1950 the *lambda* ($\Lambda$) was detected by Anderson. This was followed by the discovery of more heavy particles. So over the next years a number of new particles were found but an underlying systematic was lacking until in 1961 Gell-Mann introduced with the *Eightfold Way* an order to this collection of particles. This led him to the prediction of the *omega* ($\Omega^-$) which was experimentally discovered in 1964. Also in 1964 the quark model was proposed independently by Gell-Mann and Zweig. Back then with only 3 quarks: *down* ($d$), *up* ($u$) and *strange* ($s$). It asserted, that *baryons* consist of 3 quarks (and *anti*baryons of 3 *anti*quarks) and *mesons* of two (one quark and one *anti*quark). But it took until the discovery of the $J/\Psi$ - which includes a fourth quark: *charm* ($c$) - in 1974 until the quark model got the recognition it deserves.
Later on more of the now known particles were detected experimentally: the *tau* lepton ($\tau$) in 1975, the *gluons* ($g$) in 1979, the *bottom* (or *beauty*) quark in the early eighties, the $W^{\pm}$ and the $Z$ bosons in 1983 and finally the *top* quark ($t$) in 1994/5.

[1] An atom is the basic constituent of the chemical elements. In its core there is the nucleus which consists of protons and neutrons that are hold together by the strong force. Around this nucleus there is a shell which consists of an electron cloud that is bound to the core by electro-magnetic attraction.

[2] In the present picture of our world, every particle has an "antiparticle-partner". This is a particle with the same properties except that all chargelike properties have the opposite sign. The Feynman and Stückelberg interpretation states that a particle of negative energy that runs backward in time corresponds to an antiparticle which runs forward in time.

Of course many other experimental results and theories contributed to the picture we now have of our world and its basic constituents (a short overview is given in the next section). A more complete history and nice-to-read introduction to particle physics can be found in *Introduction to Elementary Particles* by D. Griffiths [Gri87].

## 1.2 The Standard Model of Particle Physics

All the discoveries mentioned in section 1.1 led to the development and refinement of the so-called *Standard Model* (SM) of particle physics which has been and still is very successful in explaining and predicting the experimental results since the late seventies. According to this model all matter is composed of the following elementary particles: the 3 lepton families (also called *generations*), consisting each of a lepton and a neutrino, and the 3 quark families, see Table 1.1.

| | **1.Generation** | **2.Generation** | **3.Generation** | **Charge** |
|---|---|---|---|---|
| **Quarks** | **u**p (5-15 MeV) | **c**harm (1.1-1.4 GeV) | **t**op (178 GeV) | $+\frac{2}{3}$ |
| | **d**own (3-9 MeV) | **s**trange (60-170 MeV) | **b**ottom (4.1-4.4 GeV) | $-\frac{1}{3}$ |
| **Leptons** | Electron ($e$) (511 keV) | Muon ($\mu$) (106 MeV) | Tau ($\tau$) (1.78 GeV) | $-1$ |
| | $e$-Neutrino $\nu_e$ ($<$3 eV) | $\mu$-Neutrino $\nu_\mu$ ($<$0.19 MeV) | $\tau$-Neutrino $\nu_\tau$ ($<$18.2 MeV) | 0 |

Table 1.1: Particles of the Standard Model: leptons and quarks, antiparticles not included (numbers in parentheses are mass values).

For each of these particles a corresponding antiparticle exists. Additionally for every kind of interaction between these particles - which is described by the Standard Model - there exists one or more mediator: the gauge bosons (see Table 1.2). Though gravitation is the most obvious force in our daily life, it is not described by the Standard Model.

All particles listed in Table 1.1 and Table 1.2 have been experimentally detected, but there is one particle in the Standard Model which has not been mentioned previously and that has not yet been experimentally detected, the *Higgs boson* [Hig64b, Hig64a, Hig66, EB64, GHK64]. Based on the Higgs-theory, this particle provides an explanation how the mediators of the weak force (the $W^{\pm}$ and $Z$) and the fermions develop mass through their interaction with the Higgs-field, which is hypothesized to fill the Universe.

In this theory - according to the gauge theory, which is the underlying principle of the SM - the $W^{\pm}$ and $Z$ bosons are originally massless and acquire mass through an electroweak symmetry breaking mechanism.

| **Force** | **Mediator(s)** | **Range [m]** | **Mass [GeV]** |
|---|---|---|---|
| strong | 8 Gluons ($g$) | $10^{-15}$ | 0 |
| electromagnetic | Photon ($\gamma$) | $\infty$ | 0 |
| week | $Z^0/W^{\pm}$ | $10^{-18}$ | 91,17 / 80,22 |
| gravitation | Graviton | $\infty$ | 0 |

Table 1.2: Particles of the Standard Model: force mediators (for completeness, the table includes the graviton, which is not described in the Standard Model).

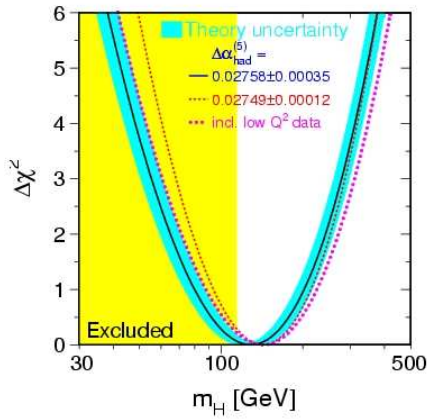


Figure 1.2: Delta-$\chi^2$ curve derived from high-$Q^2$ precision electroweak measurements, performed at LEP and by SLD, CDF, and D∅, as a function of the Higgs-boson mass, assuming the Standard Model to be the correct theory of nature. Figure taken from [LE05].

Since the Higgs is an essential feature of the Standard Model, the search for it and the measurement of its properties is a crucial task in today's particle physics. The lower limit for the mass range of the Higgs boson has been set through direct search at LEP (*Large Electron Positron collider*, CERN, Switzerland [CERN05]) to $m_{Higgs}$ >114.4 GeV (95 % confidence level limit). An upper limit can be derived through the combination of precision measurements done at LEP, SLD (*SLC collider, SLAC, USA*), CDF (*Collider Detector at Fermilab*) and D∅ (*Tevatron, Fermilab, USA*). They show that the mass of the Standard Model Higgs boson is lower than about 285 GeV. The preferred value for its mass is at 129 GeV, with an experimental uncertainty of +74 and -49 GeV. (Higgs mass values from [ALEPH03] and [LE05]; see Figure 1.2).

## 1.3 The International Linear Collider

### 1.3.1 Physics Motivation

Though being very successful and in excellent agreement with experimental data, the Standard Model has its limits. One problem is that astrophysical observations indicate that only about 5 % of the matter in our universe consists of the particles listed above. So a new theory, that includes the Standard Model but goes beyond and provides an explanation for the composition of the other 95 %, has to be developed and established. Nowadays theories state that about 25 % of the universe consist of *dark matter* [BHS05] and the remaining 70 % of *dark energy*.

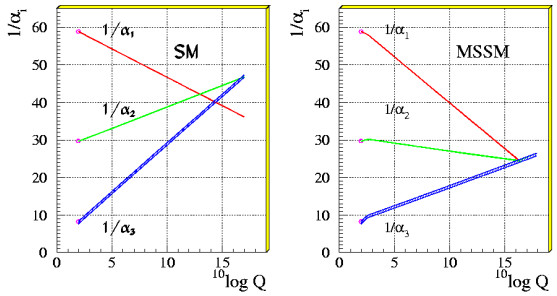


Figure 1.3: Extrapolation of the energy scaling of the coupling constants of electromagnetic, weak and strong force. Left: Standard Model without SUSY, right: *Minimal Supersymmetric Standard Model* (MSSM). Figure taken from [Kaz00].

A second problem are the *Grand Unification Theories* (GUT) which came up several decades ago, when the *running coupling constants* of the three forces (electromagnetic, weak and strong) were observed. These coupling constants set the strength of each of these forces, but they scale with the energy and are not universally constant. So "*running* coupling constants" means that the couplings become functions of a distance respectively dependent on an energy scale. For example the electromagnetic coupling constant $\alpha = 1/137$ has a value near $1/128$ at the LEP energy scale (about $10^2$ GeV). The GUT states that the three coupling constants would all meet at a universal value at an energy scale of about $10^{16}$ GeV.
In the past years these coupling constants have been measured very accurately and the extrapolation of these data according to the Standard Model does not unify all three forces at any energy scale. However this could be achieved through the introduction of new particles into the theory. *Supersymmetry* (SUSY, see below) is one possible way to do this and archives the unification of the coupling constants at the GUT scale, see Figure 1.3.

A third problem is the *Mass Hierarchy Problem*, which arises at the Planck scale (about $10^{19}$ GeV), where the strength of gravity becomes comparable to the other 3 forces. In the Standard Model without a new theory,

the *Higgs*, the $W^{\pm}$ and the $Z$ masses would rise to the Planck scale. Once again Supersymmetry could be the solution to this problem.
From section 1.2 we know that in the Standard Model a fermion acquires its mass through its interaction with the Higgs field. This mass is proportional to the strength of its coupling to the field. The Higgs boson itself also develops a mass through a "bare" mass term and its interactions with other particles. This leads to radiative corrections to the bare mass, which are - because of the scalar nature of the Higgs boson - as large as the largest mass scale in the theory squared. So the Higgs mass tends to be enormous. This would lead to the failure of perturbation expansion, which is used in all Standard Model calculations.
But if supersymmetric particles exist, the mass divergences from virtual particle loops from the virtual fermions and their virtual supersymmetric bosonic partners (and vise versa) are of the same size but with opposite sign. This leads to the cancellation of the corrections and automatically stabilizes the gauge theory. This theory requires that the masses of the supersymmetric partners are in the range from 100-1000 GeV.

As mentioned before, one promising theory candidate to explain many insufficiencies of the SM is *Supersymmetry* [HLS75, WZ74b, WZ74a, Mar97, Dre96]. This theory introduces a supersymmetric partner for every known particle, for every fermion a new boson an vise versa. The supersymmetric particles (also called *s*particles) should have the same mass as their partners. But since they have not been observed so far, the conclusion is that a *SUSY breaking mechanism*, which leads to the mass difference, is realized in nature. (One alternative theory - among others - to this breaking mechanism would be including gravity into SUSY).
Because *Supersymmetry* could solve many unsolved problems of the Standard Model, a big effort is put into the search for supersymmetric particles, like in the search for the Higgs particle.
The next accelerator where these researches are planned to take place is the LHC (*Large Hadron Collider*) at CERN. This particle accelerator which is being built at the moment is expected to start working in 2007. Two proton beams will collide with a collision energy of up to 14 TeV. Plans exist to increase this energy to up to 1150 TeV in the future.

While the LHC can reach enormous energies and therefore produce many new particles at energy scales which so far have been out of reach, it is limited in its precision, because of the substructure of the colliding protons. So another collider is currently planned, the ILC (*International Linear Collider*, [ILC06]). This will be an $e^+e^-$-collider with an energy range up to 500 GeV in the first stage and an upgrade option to 1000 GeV in a second stage. Though - in comparison with the LHC - the energy range of the ILC would be much more limited, its advantage lies in the well known initial state of the collision, the missing QCD-background and the resulting precision.

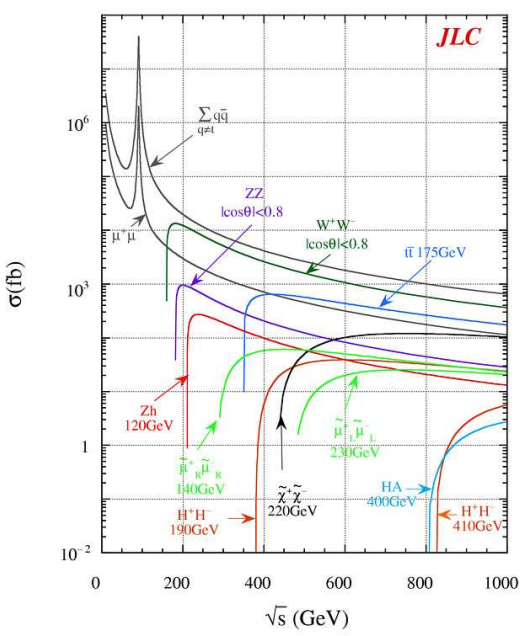


Figure 1.4: Cross sections of exp. ILC processes (ACFA Working Group [ILC06]).

For example the supersymmetric partners of the electron, the muon and the neutrinos as well as of the $\gamma$, $W$ and $Z$ bosons could be studied much more precisely at the ILC (their mass, for example, could be determined about the order of a magnitude better). This is very important to determine which supersymmetric theory is realized in nature.

Figure 1.4 shows an incomplete, but representative set of cross sections for processes that are expected to be observed at the ILC as a function of the Center of Mass Energy. The *neutralino*, which in some supersymmetric models like the *Minimal Supersymmetric Standard Model* (MSSM) is defined as the lightest supersymmetric particle, is one candidate for the dark matter. In figure 1.5 its simulated signature in the ILC detector is shown.

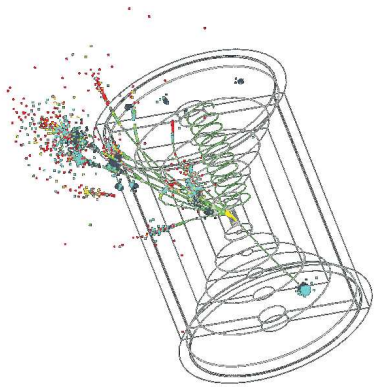

Figure 1.5: Simulation of neutralino signature (Norman Graf [ILC06]).

### 1.3.2 The Accelerator

The ILC will be built in a global collaboration and its development is based on the linear collider programs which originally started in Europe at DESY [DESY05] and CERN, in Japan at KEK [KEK05] and in North America at SLAC [SLAC05] and Cornell [Uni05, Phy05].

The different designs and technologies are now being amalgamated and further developed towards one global design. By now many more institutes than the ones mentioned above and working groups from all over the world participate in this *Global Design Effort* (GDE).

In contrast to LEP, where the highest beam energy was about 105 GeV, the ILC will not be built as a ring collider but consist of 2 linear colliders which accelerate the electrons and positrons towards a central collision point. The reason for this layout is, that accelerated charged particles on a curved track loose energy by synchrotron radiation. This limits the possible beam energy of a ring collider, since the energy loss per cycle is given by:

$$E_{rad.loss} = \frac{1}{r}\left(\frac{E}{m}\right)^4, \tag{1.1}$$

where $E_{rad.loss}$ is the energy loss, $r$ is the radius of the collider ring, $E$ the energy and $m$ the mass of the particle. As the energy dependence is $E^4$, the energy loss increases very fast with higher beam energy, which cannot be countered easily with a bigger radius since the dependency of the radius is linear. While at LEP ($r \approx$4.2 km) the energy loss was about 2 GeV (at 100 GeV beam energy), to get a similar energy loss at the planned collision energy of 500 GeV at the ILC the ring would have to have a radius of about 1000 km .

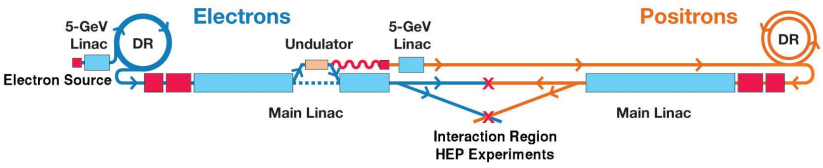


Figure 1.6: Basic ILC design scheme from the GDE (Global Design Effort). Drawing not to scale (figure from [ILC06]).

In Figure 1.6 the schematic layout of the ILC is shown. Escaping the source, the electron bunches are shaped into a more compact and uniform spatial distribution in the Damping Ring (DR). The linear electron accelerator (Linac) accelerates them to their final energy. Here the electrons pass an undulator, in which they are brought into a wavelike motion emitting lots of photons. These photons produce positrons when hitting a titanium alloy target and are lead though a second Damping Ring to the positron Linac in which they are accelerated. At the end of both Linacs is the interaction region with the high energy physics experiments.

Although the ILC is still in its planning phase some basic decisions and outlines are already made: Its energy should be scannable from 90 GeV to 500 GeV (1 TeV in the second stage) and the high luminosity range will be starting from about 200 GeV ($\mathcal{L} = 5 \cdot 10^{33} cm^{-2} s^{-1}$). Additionally an option of a modification, which would make it possible to scan the lower energy limit (90 GeV) with high luminosity, is still included in the plans.

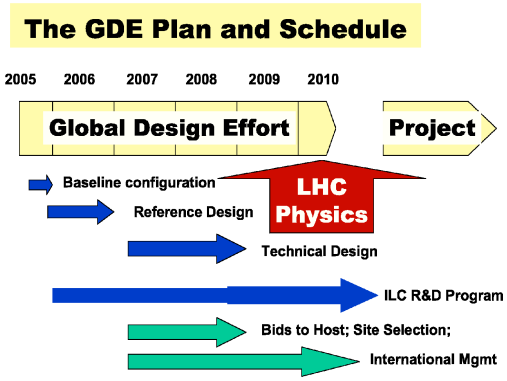


Figure 1.7: Timeline for the GDE and the ILC project (from [Bar05]).

The *International Technology Recommendation Panel* (ITRP) approved that the acceleration cavities should be based on superconducting radio frequency technology ("cold design"), similar to the technology used for the accelerator cavities in the TESLA design. This technology has a smaller power loss compared to the room temperature accelerating structures ("warm design") and allows the cavities to work at the moderate frequency of $f$ =1.3 GHz. Therefore the cavities can be larger which reduces the alignment requirements. An accelerator built with this technology and energy range will be 30 to 40 km long.
The beam of the ILC will not consist of a constant particle flow but the electrons and positrons will be accelerated in *bunches* with about 337 ns pause between two successive bunches and about $2 \cdot 10^{10}$ electrons respectively positrons per bunch. These bunches are grouped together in so-called

*bunch trains*. The bunch trains will consist of 2000 to 3000 single bunches and their rate will be about 5 Hz.

Many design decisions are still under discussion. Figure 1.7 shows the important future steps of the GDE in a timeline.

### 1.3.3 The Detector

#### The different detector concepts

The main task of the ILC will be to make high precision measurements. This leads to the following tasks for an ILC detector: reconstruct all available channels with highest efficiency and low systematics and show a negligible or low sensitivity to machine related background radiation. At the moment four different detector concepts, of which three originate from the different linear collider programs mentioned in the previous section and the fourth was proposed recently, are under consideration: the *Silicon Detector Concept*[3] (SiD) [SiD05], the *Large Detector Concept*[4] (LDC) [LDC05], the *Huge Detector Concept*[5] (GLD) [GLD05] and the *Fourth Detector Concept* [4th 05].

All of these concepts follow the typical composition of particle detectors at accelerators: The innermost layer consists of a vertex detector for high precision tracking near the interaction point. This is followed by the main tracking device - based on silicon technology in the case of the SiD and based on gaseous detection ($TPC$) for the three other concepts. After the tracking device follow the electromagnetic and hadronic calorimeters ($ECAL/HCAL$) for energy measurement and as the outermost layer the magnet coil including the muon system.

The main differences between the concepts are in the size of the detector and the magnetic field. Besides this, the SiD differs from the LDC and GLD - as mentioned in the previous paragraph - in the choice of the tracking technology: The SiD concept proposes five layers of silicon detectors for tracking, which results in only few measurements but these with very high precision, while the LDC/GLD concepts propose a TPC as central tracking device, which provides many measurements ($\sim$200 points per track) but only with medium resolution. The LDC and the GLD differ in the chosen ECAL technology and the Fourth Concept uses a different approach for calorimetry: the dual readout calorimetry (see [4th 05]). A short list of parameters of the four different concepts is shown in Table 1.3.

Figure 1.8 shows schematics of a quarter of each of the first three detector concepts (SiD, LDC and GLD), in which the structure of the detector

[3] Originating from the American small detector.
[4] Originating from TESLA and the American large detector.
[5] Originating from the GLC detector.

| Concept | outer radius of tracking | magnetic field ($BR^2$) | tracking technology |
|---|---|---|---|
| SiD | 1.3 m | 5 T ( 8.5 $Tm^2$) | Si |
| LDC | 1.7 m | 4 T (11.6 $Tm^2$) | TPC |
| GLD | 2.1 m | 3 T (13.2 $Tm^2$) | TPC |
| $4^{th}$ | 1.4 m (excl. Si-Strips) | 2 T ( 3.9 $Tm^2$) | TPC + 3 Si strip layers |

Table 1.3: List of parameters of the different detector concepts for the ILC.

layers can be seen. Three-dimensional views of these concepts are shown in Figure 1.9 (the size of the detectors are scaled in this figure and do not represent the real size differences between the different concepts). The *Fourth Concept Detector* is not shown in Figure 1.8 and 1.9 because there are no similar schematics available due to its early development status.

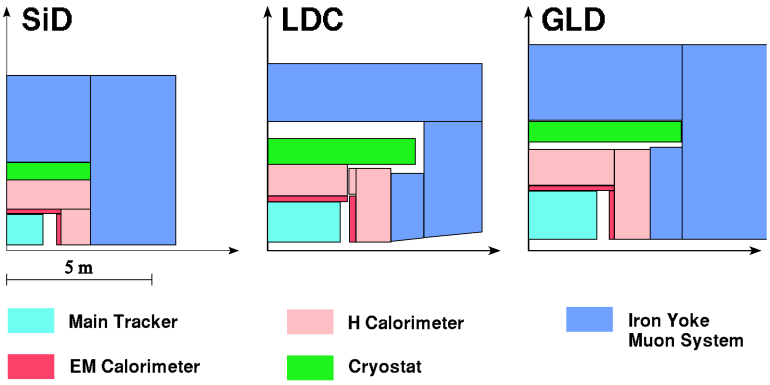


Figure 1.8: Quarter views of the SiD, LDC and GLD detector concepts.

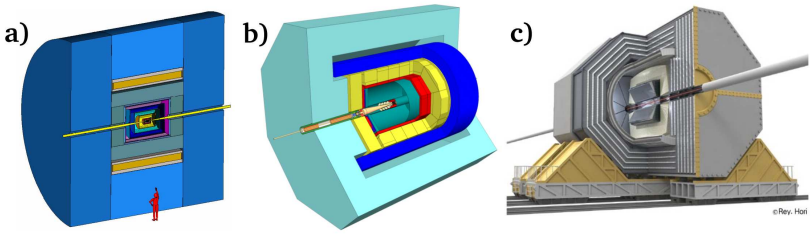


Figure 1.9: Three-dimensional views of the detector concepts:
a) SiD b) LDC and c) GLD (figures from [SiD05], [Vog05] and [GLD05]).

### The Time Projection Chamber in the LDC

Since this work has been done within the scope of the LDC, the requirements on the TPC in this concept will be described in the following in more detail. The working principles of a TPC will be described in Chapter 2, while here the requirements on a TPC at the ILC will be described. These requirements are driven by the momentum resolution needed for the physics analysis and the outline of the ILC accelerator.

One important task of the ILC will be precision measurements of the Higgs boson. These analyses include the task to precisely determine the Higgs mass from the recoil mass spectrum of the leptonic decay of the Z boson from a Higgsstrahlung process. The effect of the momentum resolution on the precision of the analysis is illustrated in Figure 1.10. The resulting requirements on the momentum resolution are:

$$\frac{\sigma_{p_t}}{p_t^2} \leq 0.5 \cdot 10^{-5}\,(\mathrm{GeV})^{-1}\ , \tag{1.2}$$

where $\sigma_{p_t}$ denotes the transversal momentum resolution and $p_t$ the transverse momentum.

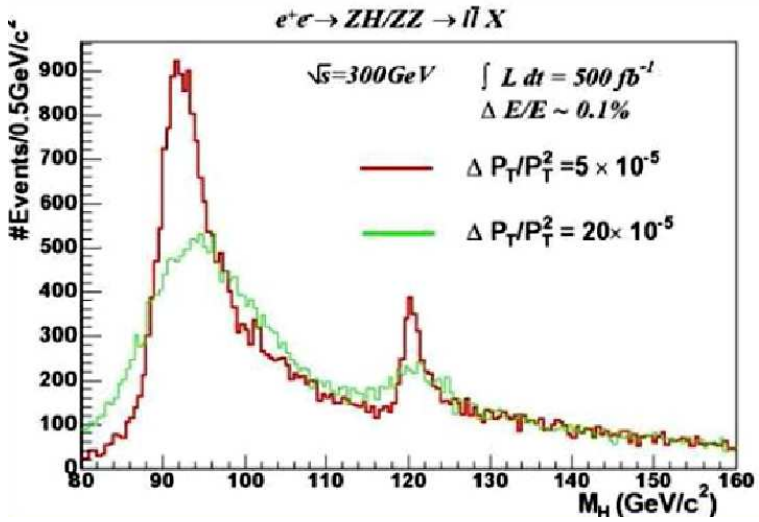


Figure 1.10: Measurement to determine the Higgs mass for two different momentum resolutions (figure from [Gar05] ).

To achieve the required momentum resolution given above for the whole tracking system including the vertex detector, the TPC alone has to meet the following requirement:

$$\left(\frac{\sigma_{pt}}{p_t^2}\right)_{TPC} = 2 \cdot 10^{-5}\,(\mathrm{GeV})^{-1}\ . \tag{1.3}$$

The momentum resolution of a TPC is related to the point resolution by the Gluckstern formula [Glu63]:

$$\frac{\sigma_{p_t}}{p_t^2} = \frac{\sigma_{r\phi}}{0.3L^2B}\sqrt{\frac{720}{N+4}}\,, \tag{1.4}$$

where $\sigma_{r\phi}$ denotes the point resolution, $L$ the length of the lever arm, $B$ the magnetic field and $N$ the number of measurement points. From this follow the point resolution requirements given in Table 1.4. Besides the point resolution, the table contains the requirements on the $dE/dx$ resolution (see Section 2.1.1) and the double pulse resolutions. All values have been taken from the TESLA TDR [Col01].
The high magnetic field of 4 T in the LCD is necessary to achieve the required momentum resolution.

Other requirements on the TPC in the LCD are that it has to work in an environment with a very high event rate (see Section 1.3.2), which poses high demands on the drift (field homogeneity and velocity) and on the amplification and readout technologies (see Section 2.3).

| Drift distance | 10 cm | 200 cm |
|---|---|---|
| $r\phi$ resolution | 70 $\mu$m | 190 $\mu$m |
| $z$ resolution | 0.6 mm | 1 mm |
| double pulse resolution in $r\phi$ | $\leq$ 2.3 mm | |
| double pulse resolution in $z$ | $\leq$ 10 mm | |
| $dE/dx$ resolution | 4.3 % for 200 pad rows | |

Table 1.4: Resolution requirements of a TPC in the LDC/ILC (values from [Col01]).

# Chapter 2

# Time Projection Chambers

In this chapter the principle of *Time Projections Chambers* (TPC) will be explained. Therefore, first the general principles of gaseous detectors will be described.

## 2.1 Principles of Gaseous Detectors

The working principle of all gaseous detectors is based on the interaction of charged particles[1] or photons with the detector gas. In these interactions, which – in the case of charged particles – can be described by a single virtual photon exchange, the charged particles deposit a part of their energy by ionizing the gas molecules. These *primary electrons* can carry enough energy to not only leave the shell of the gas molecule but also ionize further molecules through inelastic collisions setting free secondary electrons. Therefore the ionization electrons are usually produced in *clusters*.
In the processes that particles undergo traversing the gas volume two cases can be distinguished:

1. Inelastic scattering of the traversing particle at the bound electrons of the detector gas. The particle transfers enough energy to a bound electron to ionize the gas molecule. This process results in primary and secondary ionization.

2. Elastic scattering at the atomic nuclei of the detector gas, which leads to excited states of the nucleus.

In both processes only a small amount of energy is transferred. However, the inelastic scattering at the bound electrons leads to a significant energy deposition due to its large number.

[1] Neutral particles can only be detected indirectly by measuring charged particles that are produced in interactions between them and the neutral particles.

The free electrons are measured by applying an electric field that separates the electrons from the ions and and drifts them to the anode with a readout device. Depending on the strength of the electric field, this results in different effects:
In a small field the electrons are simply drifted to the readout device[2] (in a TPC, this field strength range is used in the drift volume). At higher field strengths, the electrons gain enough energy due to their acceleration to ionize other molecules on their way resulting in a cascade. In a certain range of the field strength, the measured signal is proportional to the primary ionization (*proportional mode*, this field range is applied in the amplification region of a TPC). In even higher fields, the signal will be nearly independent of the amount of primary ionization (*Geiger-Müller mode*).

### 2.1.1 Interaction of Charged Particles with Matter

Under the assumptions that the particle traversing the gas volume of the detector interacts electromagnetic, that the energy and momentum transfers do not change the direction of the ionizing particle, and that the shell electrons are free and initially at rest, the *Bethe-Bloch-Formula* can be derived [Leo94]. The assumption that the direction is not changed does only hold for particles with a much higher mass than the electron mass ($m \gg m_e$).

For relativistic particles ($v \lesssim c \Leftrightarrow \gamma \gg 1$) the so-called Fermi Density Correction has to be included, to account for the weakened electric field due to polarization caused by relativistic effects. Furthermore, the Shell Correction takes into account that for small particle energies only electrons in the outer shells can be excited.

Under the above assumptions and including the listed corrections the following Bethe-Bloch-Formula results, which describes the mean energy loss of the traversing particle per distance $x$ depending on its velocity and the properties of the absorber:

$$-\frac{dE}{dx} = \frac{e^2 N_A z^2}{\epsilon_0^2 \beta^2} \frac{Z}{A} \left[ ln\left( \frac{2 m_e c^2 \gamma^2 \beta^2}{I} \right) - \beta^2 - \frac{\delta}{2} - \frac{C}{Z} \right] \qquad (2.1)$$

[2]The case of a field that is so weak that the ions and the electrons are not separated but immediately recombine is of no interest for detectors, since this does not produce any signal at the readout.

with $dE/dx$ : energy loss per distance $x$

$e$ : electron charge $= (1.602189 \pm 5) \cdot 10^{-19} C$

$N_A$ : Avogadro's Number $= (6.02205 \pm 3) \cdot 10^{23} mol^{-1}$

$z$ : charge of the traversing particle in units of $e$

$Z$, $A$ : atomic and mass number of the absorber

$m_e$ : electron mass $= (9.10953 \pm 5) \cdot 10^{-31} kg$

$\epsilon_0$ : dielectrical constant of vacuum $= 8.8542 \cdot 10^{-12} AsV^{-1}m^{-1}$

$c$ : speed of light $= 299792458 ms^{-1}$

$\beta =$ $v/c = p/(mc)$

$v$ : velocity, $p$ : momentum and $m$ : mass of the particle

$\gamma =$ $(1 - \beta^2)^{-1/2}$

$I$ : average ionization energy of the absorber

$\delta, C$ : parameters of the Fermi Density and Shell Correction

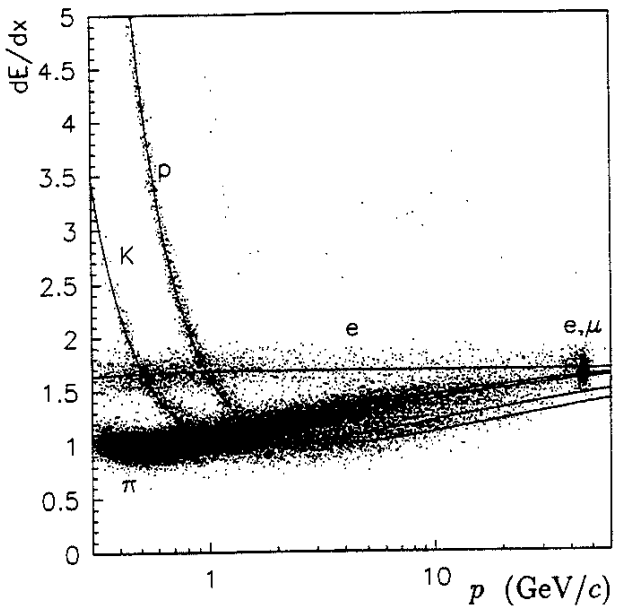


Figure 2.1: Energy loss of pions, kaons, protons and electrons measured by the *ALEPH* TPC [ALEPH95].
Solid lines: mean energy loss (Bethe-Bloch); dots: measured energy losses.

The solid lines in Figure 2.1 show some examples of the mean energy loss in dependency on the momentum of the ionizing particle. For low energies the function declines like $\beta^2$ until its minimum is reached at $\beta\gamma \approx 3 - 4$. Relativistic particles with a momentum corresponding to this minimum are called *Minimal Ionizing Particles* (MIPs). At higher momentum values, the function increases logarithmically.

The energy loss $dE$ of a particle traversing an absorber thickness $dx$ is a statistical process. The energy loss distribution can be described by so-called *straggling functions*. These functions depend on the thickness of the absorber layer $dx$, the absorber material and the velocity of the traversing particle. In the case of very thick absorber thicknesses, the *Central Limit Theorem* holds and the energy losses are distributed Gaussian around the mean value. For thin absorber thicknesses, the distribution can be described by the *Landau distribution* [Lan44]. The intermediate range is described appropriately by the *Vavilov distribution* [Vav57, SB64], which goes into a Gaussian distribution for large thicknesses and into a Landau function for thin thicknesses, see Figure 2.2.

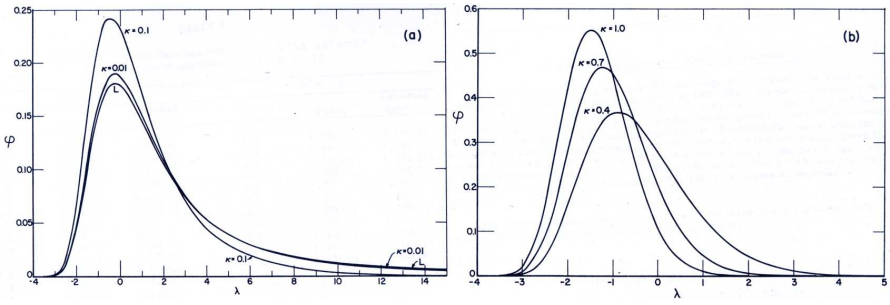


Figure 2.2: Vavilov distributions for various $\kappa$ (see text), [SB64]:
a) thin, Landau distribution for $\kappa = 0$ is also shown (denoted by the $L$).
b) thick, approach of the Gaussian limit for $\kappa \geq 1$ .

In this figure the distinguishing parameter is given by:

$$\kappa = \frac{\bar{\Delta}(x')}{W_{max}}\,, \tag{2.2}$$

where $\bar{\Delta}(x')$ denotes the mean energy loss in the whole absorber thickness $x'$ and $W_{max}$ the maximum energy transfer allowable in a single collision. The parameter $\lambda$ is given by:

$$\lambda = \frac{\Delta - \Delta_0}{\xi}\,, \tag{2.3}$$

where $\Delta$ denotes the energy loss, $\Delta_0$ the most probable energy loss and $\xi$ can be interpreted qualitatively as an energy loss exceeded, typically, in about one single collision in the thickness $x$ (Landau introduced and worked in units of $\xi$ for mathematical convenience).

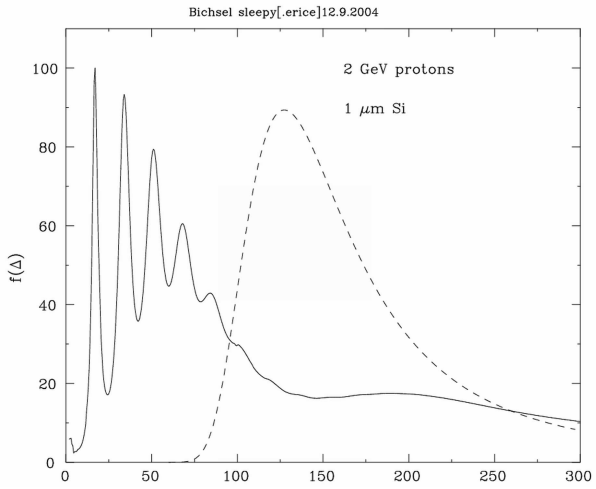


Figure 2.3: Energy straggling in very thin Silicon absorber (1 $\mu$m) for 2 GeV protons with $\langle\Delta\rangle = 400\,\text{eV}$ (Bethe-Bloch mean energy loss); solid line: straggling function from convolution method, dashed line: original Landau distribution.

In gaseous detectors, the absorber thickness used for a single energy loss measurement is usually very thin. Here, "very thin" means thinner than the thickness range where the original Landau theory holds. As an example, this corresponds to a thickness below $\approx 150\,(\text{cm}\cdot\text{atm})$ in the case of Argon gas and muons at 4 GeV, $\beta^2 = 0.9934$. In high energy physics, the straggling functions describing these cases are usually also called *Landau functions* because of their long tail to higher energies, which resembles the shape of the original Landau distribution. However, the most probable and the mean value as well as the width of the distribution can differ significantly from the original Landau distribution (see Figure 2.4). Below a certain thickness, the energy straggling distributions get sensitive to the details of the cross section: The shape of the distribution changes significantly and single bumps or spikes appear (see Figure 2.3).

The derivation of straggling functions for very thin absorber thicknesses can be done in several ways, which theoretically all lead to accurate results: The first method is the Laplace transform method, which was first ap-

plied by Landau [Lan44] to the Rutherford spectrum. Later on, Blunck and Leisegang [BL50], Vavilov [Vav57], Bichsel [Bic70] and Talman [Tal79] improved the method by applying various modifications of the primary collision spectrum. While it theoretically delivers accurate results, in practice numerical problems arise resulting from sharp resonance peaks in realistic primary collision spectra.

The use of Monte Carlo simulations [EKM77] is the second method, which however is quite time-consuming when aiming for accurate results. A comparison between the original Landau function, a Monte Carlo calculation by Ermilova, Talmans implementation of the Laplace transform method and experimental data is shown in Figure 2.4.

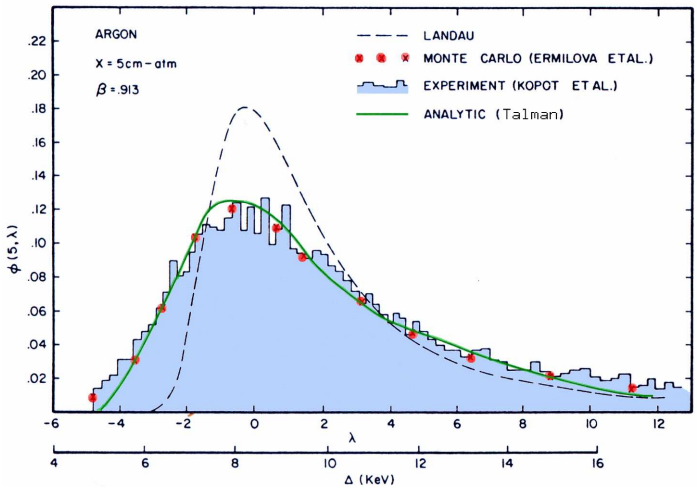


Figure 2.4: Comparison of energy straggling distributions derived by a Monte Carlo simulation, the Laplace transform method, Landau's original function and experimental data (figure from [Tal79]).

The third method is the *convolution method* described in [Bic88] and in [Bic06]. The energy straggling function for a thickness $x'$ can be calculated with repeated convolutions of the following kind:

$$f(2x, \Delta) = \int_0^{\Delta} f(x, \Delta - g) f(x, g) dg \,, \tag{2.4}$$

until $2x$ on the left side of the equation equals the desired $x'$. Here $f(2x, \Delta)$ describes the straggling distribution, $\Delta$ is the total energy loss and $x$ denotes the thickness. The initial distribution is calculated for an extremely thin absorber thickness $dx$, in which the probability of more than one collision is

negligible:

$$f(dx, \Delta) = \delta(\Delta)(1 - M_0 dx) + dx\sigma(\Delta)\,, \tag{2.5}$$

where $f(0, \Delta) = \delta(\Delta)$ and $M_0 dx = n_0 \approx 0.001$, $M_0$ equals the total collision cross section and $n_0$ denotes the average number of collisions in the absorber and $\sigma(E)$ the single collision spectrum. As shown in [BS75], no serious problems seem to arise when applying this method. Figure 2.5 shows straggling functions calculated with the convolution method for a very thin Argon gas absorber.

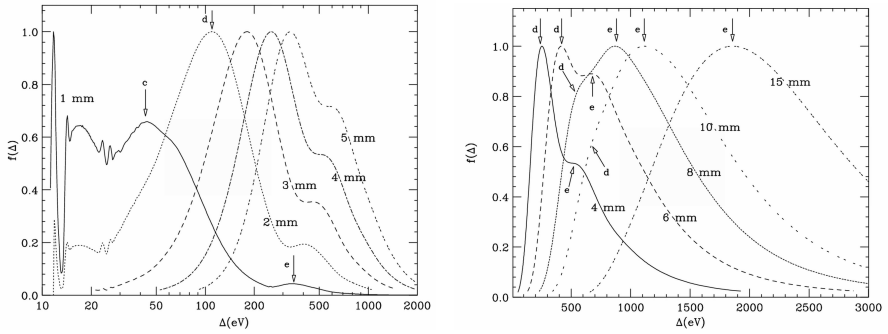


(a) 1 to 5 mm (b) 4 to 15 mm

Figure 2.5: Convolution method: energy straggling functions in very thin Argon gas absorber for singly charged particles with $\beta\gamma = 4.48$:
a) 1 to 5 mm absorber thickness b) 4 to 15 mm absorber thickness
The functions are normalized to 1.0 at the most probable value; the characters mark peaks resulting from the same cross section peaks (figures from [Bic06]).

Since the deposited energy cannot be measured directly, the relationship between the produced charge and the energy loss is important. The number of electrons produced in the primary ionization is proportional to the energy deposited by the traversing particle:

$$n_e(dx) = dE/dx \cdot W^{-1}\,, \tag{2.6}$$

where $n_e$ denotes the number of electrons, $dE/dx$ the energy loss in the thickness $dx$ and $W$ the average energy needed to produce an electron-ion pair. $W$ is larger than the ionization potential $I$, because a part of the deposited energy is transformed in excitation energy and in kinetic energy of the ion and the electron. Table 2.1 shows values for $W$, the mean ionization

potential $I$ and the mean excitation potential $X$ for different gases used in gaseous detectors. Energy conservation sets an additional constraint and the number of produced electrons is not Poisson distributed, so that the following standard deviation for the number of produced electrons results:

$$\sigma_{n_e} = \sqrt{n_e \cdot F}\,, \tag{2.7}$$

where $F$ denotes the *Fano factor* [Fan46, Fan47].

| **Gas** | $W$ **[eV]** | $I$ **[eV]** | $X$ **[eV]** |
|---|---|---|---|
| Ar | 26.3 | 15.8 | 11.6 |
| Ne | 36.4 | 21.6 | 16.6 |
| He | 42.3 | 24.6 | 19.8 |
| Xe | 21.9 | 12.1 | 8.4 |
| $CO_2$ | 32.8 | 13.7 | 10.0 |
| $CH_4$ | 27.1 | 13.1 | – |

Table 2.1: Average energy $W$ for electron-ion pair production and mean excitation (X) and ionization potentials (I) for different gases (values from [BR93], [Leo94]).

### 2.1.2 Detector Gas

The choice of the detector gas has an influence on the energy deposition and on the behavior of charged particles in the detector volume. In most cases noble gases are chosen as the main component of the detector gas because of their low ionization energies. Additionally, all noble gases are extremely chemically unreactive and not flammable making them easy to manipulate. Since in the amplification process photons with energies above the ionization potential are emitted, so-called *quencher gases* are added to the gas mixture to avoid permanent discharge. These quencher gases have a high cross section for photons in the right energy range and therefore "catch" the emitted photons. The absorbed energy is then transformed in elastic collisions, vibration and rotation states or in decomposition into simpler radicals. The addition of a quencher gas gives the possibility to operate the gaseous detector at a much higher gain (up to $10^6$).
The gas mixture has a strong influence on the detector properties such as the drift velocity, its dependency on the electric field and the diffusion of the charge cloud during the drift. Usually, the properties of the gas mixture are being calculated with Monte Carlo simulations. To derive the values given in this work, the program packages Garfield, MAGBOLTZ and Heed have

been used [Smi, ACPP, Vee84, Vee98].
For a correct calculation, gas impurities resulting from outgasing of the chamber materials and leakage have to be taken into account, since even small contaminations in the order of a few ppm can change the characteristics of the gas mixture significantly. Of course, this also should be taken into account when designing a gaseous detector and choosing the materials used in the drift volume. Also the pressure and temperature of the detector gas have an impact on the detector performance.

### 2.1.3 Drift Velocity

The drift velocity of a charged particle in an electric field (the *drift field*) can be described by the *Langevin equation* [LW92]:

$$m\frac{dv}{dt} = e\vec{E} + e\vec{v} \times \vec{B} - K\vec{v}\,, \tag{2.8}$$

where $m$ denotes the mass of the particle, $v$ its drift velocity, $t$ the time, $e$ its electric charge and $\vec{E}$ and $\vec{B}$ the electric and magnetic field. $K$ describes the "viscosity" of the gas and the term $-K\vec{v}$ is an approximation to a time dependent noise term $\vec{Q}(t)$, which takes into account the stochastic collisions with the gas molecules. The average time between two collisions is given by $\tau = m/K$.
Equation 2.8 has a steady ($dv/dt = 0$) solution for $\vec{v}_D = \langle\vec{v}\rangle$ averaged over a time $t \gg \tau$ :

$$\vec{v}_D = \frac{\mu E}{1+\omega^2\tau^2} \cdot \left[\hat{E} + \omega\tau\hat{E} \times \hat{B} + \omega^2\tau^2\big(\hat{E}\cdot\hat{B}\big)\hat{B}\right], \tag{2.9}$$

where $E = |\vec{E}|$, $B = |\vec{B}|$, $\hat{E} = \frac{\vec{E}}{E}$, $\hat{B} = \frac{\vec{B}}{B}$, $\mu = \frac{e}{m}\tau$ and $\omega = \frac{e}{m}B$ is the cyclotron frequency. The parameters $\mu$ and $\tau$ depend on the properties of the drift gas.

If the electric and the magnetic field are parallel – a situation given in most TPCs – the second term in Equation 2.9 equals zero:

$$\omega\tau\hat{E} \times \hat{B} = 0$$

and since $\vec{E} \| \vec{B}$ the last term can be written as

$$\big(\underbrace{\hat{E}\cdot\hat{B}}_{=1}\big)\hat{B} = \hat{B} = \hat{E}\,,$$

so that equation 2.10 follows, which equals the case without a magnetic field:

$$\begin{aligned}\vec{v}_D &= \frac{\mu E}{1+\omega^2\tau^2} \cdot \left[\hat{E}\big(1+\omega^2\tau^2\big)\right] \\ &= \mu\vec{E} = \vec{v_D}(\vec{B}=0)\,. \end{aligned} \tag{2.10}$$

Equation 2.9 applies to all charged particles that drift in an electric and magnetic field. The ions drift about 1000 times slower than the electrons since their mobility $\mu \sim 1/m$ is much lower due to their larger mass.
In the presence of a strong magnetic field, the term $\omega\tau$ gets large for drifting electrons and therefore the third term in Equation 2.9 becomes dominant. In this case the electrons will essentially follow the magnetic field lines, although the drift is caused by the electric field. Because the ions are much heavier, the impact of the magnetic field on their drift is much smaller ($\omega\tau \sim 1/m$) and they still follow the electric field lines.

Figure 2.6.a shows the dependency of the electron drift velocity on the electric field for two different gas mixtures. With increasing drift field the drift velocity increases fast until it reaches a maximum and then decreases slowly. This was first explained by Carl Ramsauer [Ram21], who observed the huge permeability of noble gases for slow electrons and introduced a collision cross section to explain this effect. Based on classical models the cross section should be decreasing monotonically with larger kinetic energy (and therefore larger velocity) of the drifting electron.
Ramsauer however observed that the cross section shows a strong dependency on the kinetic energy of the electron. This can be explained with de Broglie's hypothesis that all matter has a wave-like nature. Due to a resonance effect, the cross section increases if the electron has an energy that corresponds to a wave length which equals the size of the gas molecules[3].

Figure 2.6.b shows the effect of small amounts of water pollution in the drift gas on the electron drift velocity: With a larger water pollution, the maximum of the drift velocity gets smaller and a higher drift field is needed to reach it.

The relation between the gas pressure and the drift velocity is shown in figure 2.7. The mean free path length between two collisions of the electron with the gas molecules is dependent on the gas pressure $P$ like $\frac{1}{P}$. To take this effect into account, a "reduced field" $E/P$ can be introduced and from equation 2.10 follows that the drift velocity is inverse proportional to the gas pressure:

$$\vec{v}_D = \mu\hat{E}'(P) \text{ , with } \hat{E}'(P) = \frac{\hat{E}}{P}\,. \tag{2.11}$$

[3]Named after its discoverer, the Ramsauer effect is nowadays reckoned as the first experimental proof of the wave character of the electron.

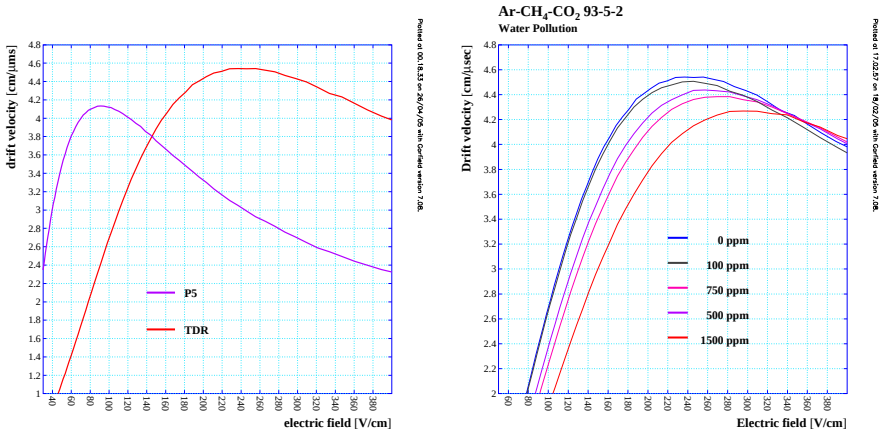


(a) P5 and TDR gas (b) Water pollution

Figure 2.6: Electron drift velocity in dependency on the electric field:
a) for P5 (95 % Ar, 5 % $CH_4$) and TDR (93 % Ar, 5 % $CH_4$, 2 % $CO_2$) gas
b) for different amounts of water pollution in TDR gas
(values simulated with GARFIELD, figure from [Lux05]).

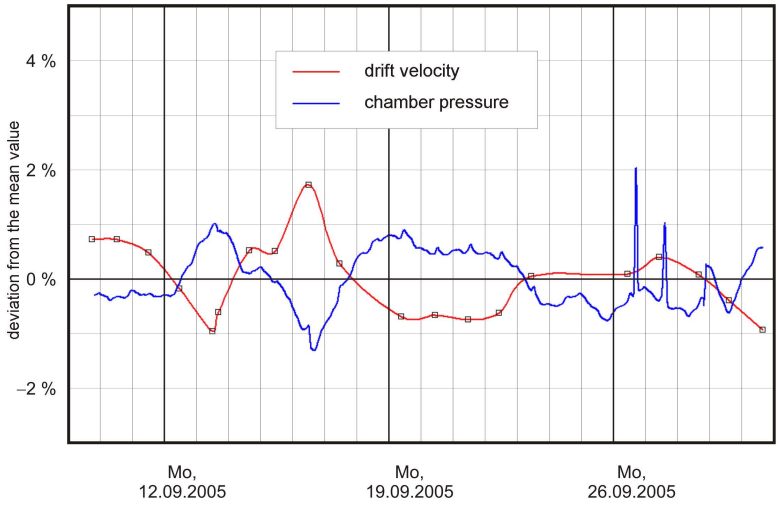


Figure 2.7: Relation between the drift velocity and the gas pressure;
(figure from [Sch05]).

Some examples of typical drift velocities in large TPCs are given in Table 2.2, together with the experiment name, the gas mixture, pressure and the drift field.

| Experiment | **LBL** | **ALEPH** | **DELPHI** | **STAR** | **ALICE** |
|---|---|---|---|---|---|
| Gas Mixture | 80:20 ($Ar:CH_4$) | 91:9 ($Ar:CH_4$) | 80:20 ($Ar:CH_4$) | 90:10 ($Ar:CH_4$) | 90:10 ($Ne:CO_2$) |
| Pressure [bars] | 8.5 | 1 | 1 | 1 | 1 |
| E-Field $[\frac{V}{cm}]$ | 650 | 110 | 180 | 148 | 400 |
| Velocity $[\frac{cm}{\mu s}]$ | 5 | 5.2 | 7 | 6 | 2.8 |

Table 2.2: Drift velocity including important parameters for different TPCs.

### 2.1.4 Diffusion

The drift velocity calculated in the previous section is only a mean value for drifting electrons. Isotropical diffusion processes due to the thermal energy of the electrons in the gas cause a smearing of the charge cloud around the mean position. The energy is given by the Maxwell-Boltzmann distribution which leads to the following equation for the mean velocity without outer fields:

$$v = \sqrt{\frac{8kT}{\pi m_e}} \text{ , with } k \;:\; \text{Boltzmann constant} \tag{2.12}$$

$$T \;:\; \text{gas temperature}$$

$$m_e \;:\; \text{electron mass}\,. \tag{2.13}$$

As in the previous section, $\tau$ is the mean time between collisions so that the probability that an electron didn't undergo a collision at the time $t$ is $\frac{1}{\tau} \cdot exp(-\frac{t}{\tau})$. With $\lambda$ denoting the mean free path and with the distance the electron can fly until the first collision given by the fraction $\frac{t}{\tau}\lambda$, it follows for the spread of the charge distribution:

$$\delta_0^2 = \frac{1}{3}\int_0^\infty \frac{dt}{\tau} \exp\left(-\frac{t}{\tau}\right) \cdot \left(\lambda\frac{t}{\tau}\right)^2 = \frac{2}{3}\lambda^2\,. \tag{2.14}$$

Here the drift velocity has been assumed to be the same for all electrons. After a time $t \gg \tau$ corresponding to a large number of collisions, the spread is given by

$$\sigma_0^2(t) = \frac{2}{3}\lambda^2\frac{t}{\tau}\,.$$

A diffusion coefficient can be defined as $D' = \sigma^2(t)/2t$ so that follows:

$$D'_0 = \frac{\sigma_0^2(t)}{2t} = \frac{1}{3}\frac{\lambda^2}{\tau} = \frac{1}{3}v\lambda\,, \tag{2.15}$$

where the subscript "0" denotes the field-free case.

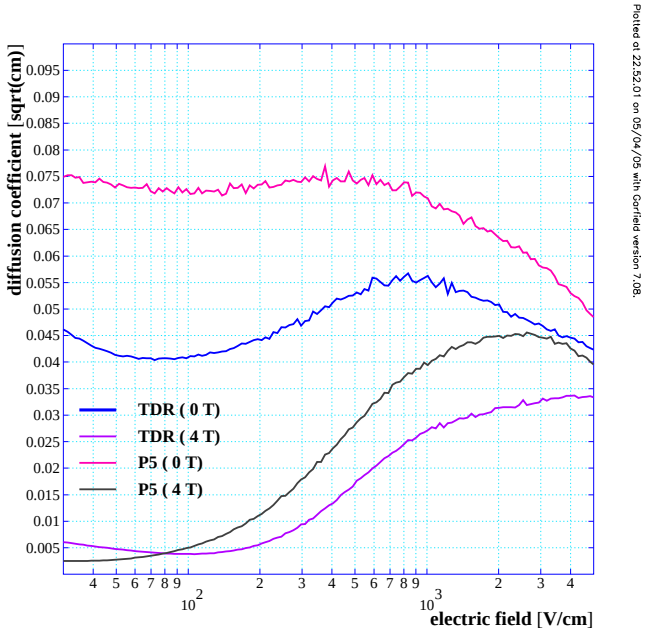


Figure 2.8: Longitudinal and transverse diffusion in dependency of the electric field; simulated with *Garfield* for TDR and P5 gas (figure from [Lux05]).

In the presence of an outer electric field the thermal movement and the movement due to the field superimpose and two cases have to distinguished. In "cold" gases (e.g. $CO_2$) the thermal movement is dominant up to very high field strengths and the diffusion stays independent from the outer field. In other gases like e.g. Argon this is not true and the movement due to the outer field is dominant even at low field strengths. Since the electrons at the leading and the trailing edge of the charge cloud have different energies and hence different collision rates, the longitudinal diffusion changes and differs from the transverse diffusion[4] [WDH67]. This dependency of the longitu-

[4]Longitudinal and transverse denote the directions in respect to the applied electric field.

dinal and transverse diffusion coefficients on the electric field is shown in Figure 2.8.
In this case the following definition of a diffusion coefficient is more convenient:

$$\sigma_D = D\sqrt{L}\,, \tag{2.16}$$

where $L$ denotes the drift length and $D$ is related to the previous defined coefficient $D'$ by:

$$D = \sqrt{\frac{2D'}{v_D}}\,. \tag{2.17}$$

If an magnetic field is applied, the longitudinal diffusion parallel to the field is unchanged. But since the magnetic field causes a force perpendicular to its direction, the transverse diffusion coefficient is dependent on the field strength.
The transverse path of the electrons can be described by a circular arc with the radius $\rho = v_T/\omega$, where $v_T^2 = 2/3 \cdot \lambda^2/\tau^2$ denotes the mean transverse velocity.
After flying a path length of $s = v_t t$ the transverse distance of the electron is given by $2\rho \cdot \| \sin(s/2p) \|$ (see Figure 2.9).

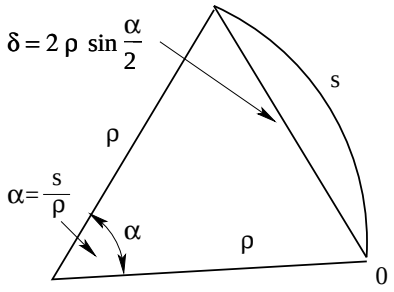


Figure 2.9: Sketch of the transverse distance of the electron in a magnetic field

The spread of the charge distribution can be given analogous to the field-free case in equation 2.14 as:

$$\delta^2(B) = \frac{1}{2}\int_0^\infty \frac{dt}{\tau}\exp\left(-\frac{t}{\tau}\right)\cdot\left[2\rho\sin\frac{tv_T}{2\rho}\right]^2 = \frac{1}{2}\frac{\tau^2 v_T^2}{1+\omega^2\tau^2}\,. \tag{2.18}$$

Again calculating the spread after a time $t \gg \tau$ leads to:

$$\sigma^2(B,t) = \frac{t}{2}\frac{\tau v_T^2}{1+\omega^2\tau^2} = t\frac{D_0}{1+\omega^2\tau^2} \tag{2.19}$$

and following from that

$$D_T(B) = \frac{D_0}{1+\omega^2\tau^2}\,, \tag{2.20}$$

where $D_0$ equals the coefficient $D$ from Equation 2.17. So the transverse diffusion coefficient is by the factor $\frac{1}{1+\omega^2\tau^2}$ smaller than the diffusion coefficient

in the field-free case. Figure 2.10 shows the dependency of the longitudinal and transverse diffusion coefficients on the magnetic field.

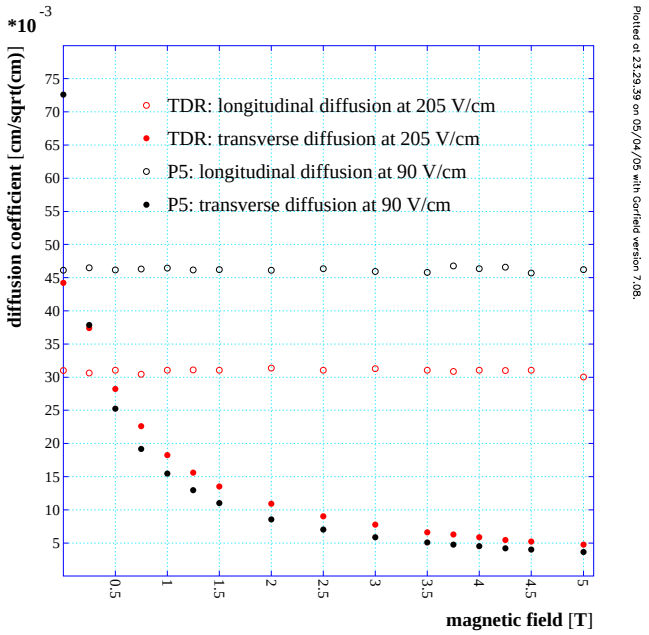


Figure 2.10: Longitudinal and transverse diffusion in dependency on the magnetic field; simulated with *Garfield* for TDR (93 % Argon, 5 % $CH_4$, 2 % $CO_2$) at $E = 205\frac{\mathrm{V}}{\mathrm{cm}}$ and P5 gas (95 % Argon, 5 % $CH_4$) at $E = 90\frac{\mathrm{V}}{\mathrm{cm}}$ (figure from [Lux05]).

### 2.1.5 Gas Amplification

If, through the acceleration in the electric field, the drifting primary electrons gain enough energy between two collisions, they can ionize the gas molecules releasing secondary free electrons. This effect starts at electric field strengths above a few 10 kV/cm. Both the primary and the secondary electrons are continuously accelerated during their drift and ionize further molecules leading to an avalanche process. This process can be described by the following equation for the number of electrons $N$ after a distance $x$:

$$N(x) = N_0 \cdot e^{\alpha x}\,, \tag{2.21}$$

where $\alpha$ is the probability of one ionization per unit length. $\alpha$ is called the Townsend coefficient and depends on the drift gas and the strength of

the electric field. If the detector is operated in proportional mode, the gain factor

$$G = \frac{N(x_f)}{N(x_0)} = \exp\left(\int_{x_0}^{x_f} \alpha(x)dx\right) \tag{2.22}$$

is an important parameter. Here $x_0$ and $x_f$ denote the starting and the end points of the avalanche process and since the electric field is usually inhomogeneous in the gas amplification region, the Townsend coefficient gets dependent on the position: $\alpha = \alpha(x)$.

## 2.2 Principles of a Time Projection Chamber

The Time Projection Chamber (TPC) has been introduced in 1976 by D. R. Nygren [Nyg]. It consists of a gas filled sensitive volume, usually with a central cathode that divides the volume into two identical halves. On both sides are anodes with readout systems. The cathode is at a potential that results in a field strength of some 100 $\frac{\text{V}}{\text{cm}}$ (see Table ) while the anode is at ground potential[5]. In $4\pi$-detectors[6] at high energy experiments, the drift volume is usually cylindrical and the beam pipe goes through the rotation axis of the TPC with the interaction point being at the center.

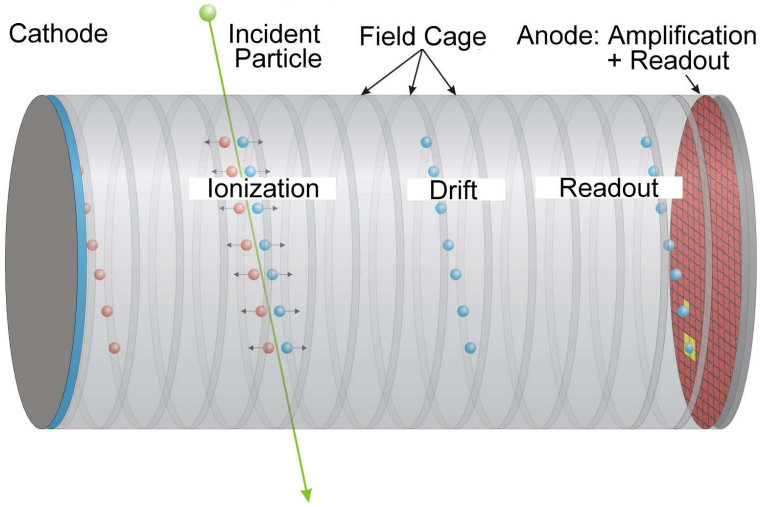


Figure 2.11: Sketch of a Time Projection Chamber and its working principle (figure from [Sch05]).

[5] Typically, this leads to a potential of some 10 kV at the cathode.
[6] $4\pi$-detectors are detectors that cover (nearly) the whole solid angle.

Figure 2.11 shows a sketch of one half of a TPC. When the incident charged particle crosses the sensitive volume it ionizes the gas molecules. In the electric field between the cathode and the anode, the produced electrons and ions are being separated and drifted to opposite ends of the TPC. In front of the anode is a gas amplification device which creates an electron avalanche and operates in proportional mode. The amplification is necessary because the amount of primary electrons is too small ($\sim 100 \frac{e^-}{\mathrm{cm}}$) to create a measurable signal. Behind the amplification region is a segmented readout system, that measures the produced charge. The amplification and the readout systems will be described in more detail below.

In the following, a cylindrical coordinate system with the $z$ axis being the rotation axis of the cylindrical volume will be used. The coordinates in the plane perpendicular to this axis are given by the radius $r$ and the angle $\phi$. On the readout plane, the projection of the path of the incident particle to the $r\phi$ plane is measured. The $z$ coordinates of the path can be determined using the time information:

$$z = v_D \cdot (t_2 - t_1)\,, \tag{2.23}$$

where $t_2$ is the time when the signal has been measured on the readout plane and $t_1$ is the time when the incident particle crossed the sensitive volume. The second time information $t_1$ has to be measured with an additional detector. To be able to apply Equation 2.23, the drift velocity $v_D$ should be constant. Since the drift field should be homogeneous, the sensitive volume is enclosed by a field cage. Furthermore the gas mixture should be chosen in a way that the drift velocity $v_D$ has a moderate dependency on variations of the drift field in a certain range around the applied field strength. Therefore the chamber is usually operated at field strengths that correspond to the maximum of the drift velocity curve in Figure 2.6.a. This also has the advantage that the electrons drift as fast as possible to the readout plane, so that the sensitive volume is "emptied" fast.
In general, a magnetic field is applied parallel to the $z$ axis, so that the incident charged particles are forced on a curved trajectory (respectively a helix in three dimensions). By measuring the radius $\rho$ of the $r\phi$ projection of the trajectory, the transverse momentum of the particle can be determined:

$$p_t\,[GeV] \approx 0.3 \cdot \rho\,[m] \cdot B\,[T]\,. \tag{2.24}$$

Using $p_t$ and the $z$ information it is possible to calculate the total momentum $p$ of the incident particle. Another positive effect of the magnetic field is, that it limits the transversal diffusion, so that a better spatial resolution and two track separation can be achieved.

Using a TPC as central tracking device has several advantages. Since the detector consists mostly of a gas filled volume, the TPC has a low material budget and particles traversing it deposit only very little energy. This allows for a very precise measurement of the particle energy in a following calorimeter.

Furthermore, a large number of three-dimensional space-points can be reconstructed and therefore a reliable three-dimensional reconstruction of the particle trajectory is possible. This is especially important if more than one particle crosses the detector at the same time, which is usually the case in high energy experiments.

Another advantage is that it is possible to identify the measured particles:
As explained above in section 2.1.1, the produced charge is proportional to the deposited energy of a particle. Since the gas amplification device is being operated in proportional mode, the deposited energy $dE$ per distance $dx$ of a particle can be determined.
Because the energy deposition is a statistical process, the $dE/dx$ calculation is done for all segments of the readout plane. With these values and the appropriate energy straggling distribution it is possible to calculate the mean energy loss of the particle very accurately. Using the calculated momentum value, the identity of the measured particle can be determined using the Bethe-Bloch Equation 2.1, since the mean energy loss $dE/dx$ at a given momentum is different for different kinds of particles.
As shown in figure 2.1 the $dE/dx$ curves of several particles can be very close. So the accurate determination of the mean energy loss value and therefore the knowledge of the correct energy straggling distribution are very important for a reliable particle identification.

Compared to a silicon tracking detector, one disadvantage of a TPC is that it is a quite slow detector. This can lead to difficulties in environments with a high particle occupation, e.g. if the event rate is very high. Also, in such environments the slowly drifting ions can pose a problem, since their accumulated charge can lead to distortions in the electric field.

The space-point measurement is much more accurate in a silicon tracking detector. But usually, the number of space-point measurements in a silicon detector is limited by the constraint of the material budget before the calorimeter:
A layer of silicon including the needed readout electronics has a much higher density than gas. Taking this into account, the disadvantage of a less accurate point reconstruction can be countered in the track reconstruction by the availability of more point measurements. Also, the quasi-continuous measurement of the trajectory makes the reconstruction of events with particle decays (two or more tracks originating from one) or scattering events

(abrupt changes of flight direction[7]) more easy. The large number of available measurement points per track is an advantage in the $dE/dx$ calculation, too.

## 2.3 Amplification Devices

In this section the gas amplification devices mentioned in the previous sections will be described in further detail. Up to now proportional wires have been the standard device used in TPCs for gas amplification. Some drawbacks of this technique lead to the development of new amplification structures, so-called micro-pattern gas detectors. Two different technologies of micro-pattern devices are under investigation for their use in a TPC at the ILC: MICROMEGAS and Gas Electron Multipliers (GEMs). The studies in this thesis have been based on measurements with the GEM technology, which is described in Section 2.3.2. An overview over MICROMEGAS can be found in [GRRC96].

### 2.3.1 Proportional Wires

The gas amplification with proportional wires is and has been a widely used technique. It is illustrated in Figure 2.12. The setup consists of 3 wire grids and a pad plane.

The wire grid that is closest to the pad plane consists of amplification and field wires. The amplification wires are at a positive potential that is in a range, in which a proportional gas amplification near the wires starts. The arriving electrons are "drawn" to it and multiplied in an avalanche process. This process needs about 1 ns until all produced electrons are collected on the wires. The produced ions drift back towards the drift region and the cathode. The energy change of the field due to the ion charge cloud produces the main part of the signal and since the ion drift velocity is very slow, the signal is very long compared to the electron drift and signal. This induced, very broad signal is not only measured at the wires but – to improve the resolution – also at a pad plane. The field wires are thicker and are at a lower potential, so no gas amplifications happens. They are used to stabilize the electric field.

The shielding wires are the second wire grid and they serve to straighten the electric field at the transition between the amplification and the drift region.

The third wire grid consists of the gating wires. They are necessary to collect the ions produced in the amplification region and stop them from

[7] In the case of scattering, even small changes of the flight direction can make the reconstruction difficult if not many measurement points are available.

reaching the drift region. As mentioned before the accumulation of the ions has a negative effect on the field homogeneity and could furthermore "catch" drifting electrons and reduce the signal. When the gate is open the gating wires are at the same potential as the field in this region. In this state, drifting electrons (and ions) pass this grid without disturbance. To close the grid and collect the ions, the potential of neighboring wires is set alternating to $\pm$ (50 - 100) V. In this setting, the drifting ions and electrons are collected on the wires.
Normally this gate is closed. If – based on an external trigger – the decision is taken that an event is interesting, the gate is opened and a measurement is done. After this, the gate is closed again to prevent the ion back-drift.

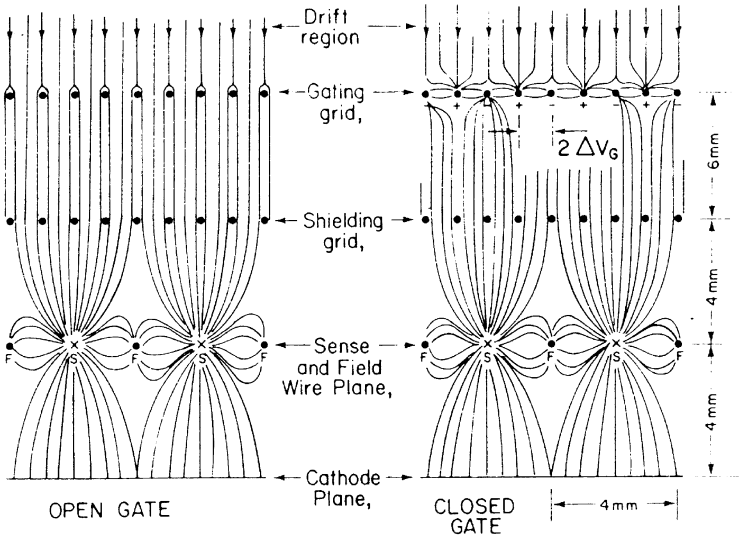


Figure 2.12: Sketch of the principle of gas amplification with proportional wires (figure from [B$^+$80]).

The proportional wire technique has some disadvantages. First, the ion signal is very broad on the pad plane and the distance between two wires is mechanically limited. This makes it difficult to separate two nearby tracks. Furthermore, the broad width and the slow signal set limits to the possible $r\phi$ and time resolution.
A second disadvantage is the high material budget of the support structures that hold the wires. To provide a perfectly parallel alignment of the wires they have to be mounted under very high tension. This demands for a very solid mounting system with a high material budget and sets limits to the minimal distance between two wires.
Third, the gating is problematic in experiments with a high event rate, where

the time between two events is too short for the gating and measurement cycle. If the events do overlap, which means the drift needs longer than the time between two events, gating becomes impossible.

In the case of the ILC all these three problems are realized. A good two-track separation and precise time resolution is needed to achieve the physics goal of the project. To be able to make a very precise energy measurement in the calorimeter, the material budget is very limited. Furthermore, the event rate of the bunch trains is so high that the gating with a grid would not work anymore. Therefore a new amplification technique is needed, that will be described in the next section.

### 2.3.2 Gas Electron Multipliers (GEM)

The GEM technology, which has been introduced by F. Sauli in 1996 and is in use in high energy and medical physics [Sau97, B$^+$00], provides the possibility to avoid the problems mentioned in the previous section.

GEMs consist of a thin Kapton foil ($\sim 50\,\mu$m) which is coated on both sides with copper layers ($\sim 5\,\mu$m). This structure is perforated with holes that typically have a diameter of $70\,\mu$m and a pitch of $140\,\mu$m. The holes are arranged in a hexagonal pattern and due to the production process, in which the holes are etched, they have a double conical shape with an inner diameter of about $55\,\mu$m. Figure 2.13.a shows a picture of a GEM that has been taken with an electron microscope.

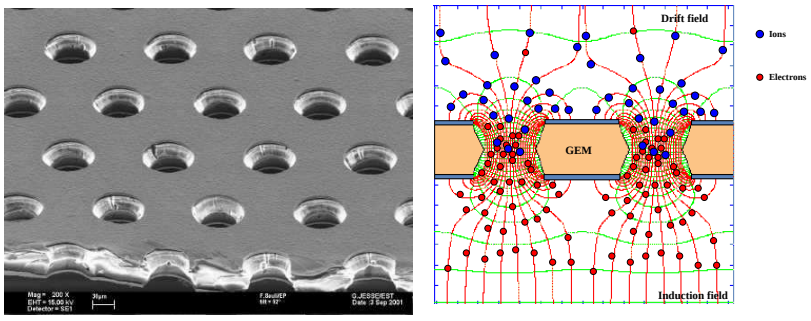


(a) (b)

Figure 2.13: Gas Electron Multiplier:
a) photo of structure taken with an electron microscope (photo from [GC])
b) sketch of the working principle (figure from [Lux05]).

The working principle of the GEMs is shown in Figure 2.13.b. Between the two copper coatings a voltage of a few 100 V is applied. Since the field lines are focused in the holes, here the resulting electric field strength is in the order of some 10 kV/cm which is high enough for the gas amplification. It is possible to achieve an amplification up to ten thousand, but usually a setup consists of two or three successive GEMs which are operated at a lower voltage and therefore run more stable.
The field in the region towards the cathode is lower than the field towards the anode. So most field lines of the electric field in the first region end on the GEM surface while on the other most lines go into the direction of the anode. The ions which are produced during the gas amplification in the GEM holes are drawn to and collected on the GEM surface while most of the electrons are extracted out of the GEM holes by the higher field after the GEM and drift towards the readout plane. The electron extraction is intensified if additionally a magnetic field is applied perpendicular to the GEM plane. As shown in Section 2.1.3, the electrons tend to follow the magnetic field lines which go straight through the GEM plane. The intrinsic ion back-drift suppression is one of the main advantages of the GEMs and makes a gating grid unnecessary [K$^+$04].
The effective gain of the GEM amplification is different from the gain in the GEM holes: Some electrons are not drawn into the GEM holes and end on the GEM surface before the amplification process. After the amplification some electrons produced in the GEM holes follow the field lines to the GEM surface and are collected there.
Another advantage of the GEM amplification are the fast signals. While in the case of the proportional wires the influence signal of the slow drifting ions is measured on the pad plane, here the direct electron signal is measured on the pad plane. This leads to a better time (respectively $z$) resolution.
That the GEM signal on the pad plane is narrower than the signal in the case of the proportional wires is an advantage in the two-track separation, but also poses new problems in the $r\phi$ resolution. The pads have to be smaller, so that a narrow signal still hits enough pads for a good reconstruction in the $r\phi$ plane (see Section 5.1.2). However, the number of pads is limited by the feasible number of readout channels and the signal height. If the area of a pad is too small, the collected charge on the pad produces a too small signal relative to the noise.
The broadening of the charge cloud by diffusion in the amplification region (between the first GEM and the readout plane) is called *defocussing*. It differs from the diffusion in the drift region because of the different electric field strengths and because it is independent of the drift length. The most important difference is that the statistics per pad of the primary ionization is degraded by the diffusion in the drift region, since the number of electrons is (more or less) constant while their spatial distribution is broadened. This

results in less primary statistics on a single readout pad. In the case of the defocussing, the statistics is not degraded since the number of electrons is increased due to the amplification which counters the effect of the broadening.
More detailed descriptions of the GEM amplification and their properties are given in the following theses and publications: In [Lux05] and [Jan04] the setup and GEMs used in the context of this work are described. In [BBSV03], [Sob02] and [Web03] the gas amplification and the ion back-drift have been studied.

# Chapter 3

# Data Acquisition and Simulation

In this chapter the data pool used in the analysis will be described. This includes a short introduction of the measurement setup and the properties of the taken data. After that follows a description of the Monte Carlo simulation, which has been used to study the reconstruction methods by simulating the measurement setup and possible effects in future setups.

## 3.1 Measurement Setup

To study if a TPC with a GEM amplification device could meet the requirements of a TPC in the LDC, several prototypes have been build. In this study the measurements with the so-called MediTPC prototype have been analyzed. This prototype was built to be used in a magnet test stand to do measurements in high magnetic fields up to 4 T. A detailed description of the prototypes and their properties can be found in [Lux03, Jan04, Lux05]. Here only the basics and important facts will be described.

Figure 3.1 shows a picture of the MediTPC prototype. The prototype has a length of 800 mm and a diameter of 270 mm. The sensitive volume of the setup is $666.0 \times 49.6 \times 52.8\,\mathrm{mm}^3$. The last two numbers give the size of the pad readout plane in the vertical and horizontal direction. The sensitive volume is illustrated as yellow area in Figure 3.3.

The GEMs are arranged in a triple-GEM amplification structure (Figure 3.2.a) with the distance between the single GEMs being 2 mm and between the last GEM and the readout plane 3 mm. Around the first GEM at the transition to the drift field, there is a metal shield which is at the same potential as the upper surface of that GEM on the side of the drift field. The fields between the GEMs are called *transfer fields* and the field between the last GEM and the readout plane the *induction field*.

The pad plane consists of 28 × 12 pads (see Figure 3.2.b). The outer two columns and rows are connected with the surrounding metal plane over 100 kΩ resistors to avoid cross-talk, leaving 192 pads that have been read out (24 columns × 8 rows). The pads have a size of 6.0 × 2.0 mm$^2$. The space between two pads is 0.2 mm on all sides, so that a pitch of 6.2 respectively 2.2 mm results. The pitch is the important specification in the analysis because the field lines do not end between, but only on the pads. Therefore the effective size of a pad is given by the pitch.

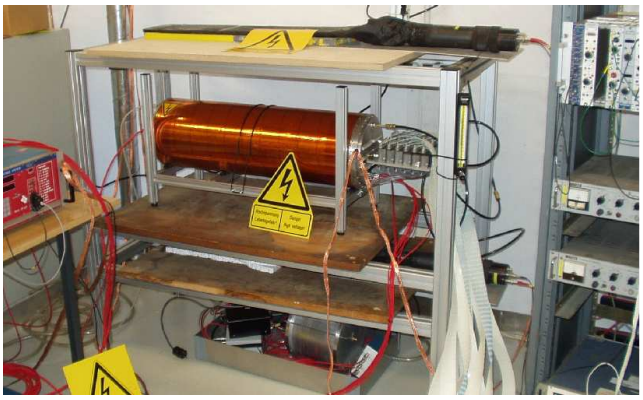

Figure 3.1: Picture of the MediTPC prototype (figure from [Lux05]).

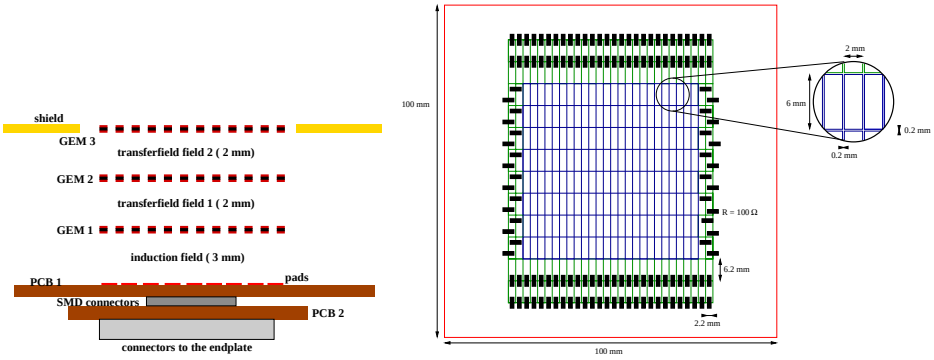


(a) GEM tower (b) Pad plane

Figure 3.2: Sketch of the readout structures:
a) GEM tower [Lux05] and b) pad plane [Jan04].

A sketch of the magnet test stand is shown in Figure 3.3. It shows the MediTPC prototype mounted in the magnet. The magnet can produce a magnetic field of up to 5.25 T and is based on superconducting technology. Therefore it needs Helium for cooling. The Helium supply lines go in on the top and, as shown in the sketch, this prevents a symmetric alignment of the trigger system. The trigger consists of two scintillators on the top and the bottom of the magnet. The light flash a passing particle produces in the scintillator is measured by a photomultiplier on the end of the trigger and then the signal is electronically processed.

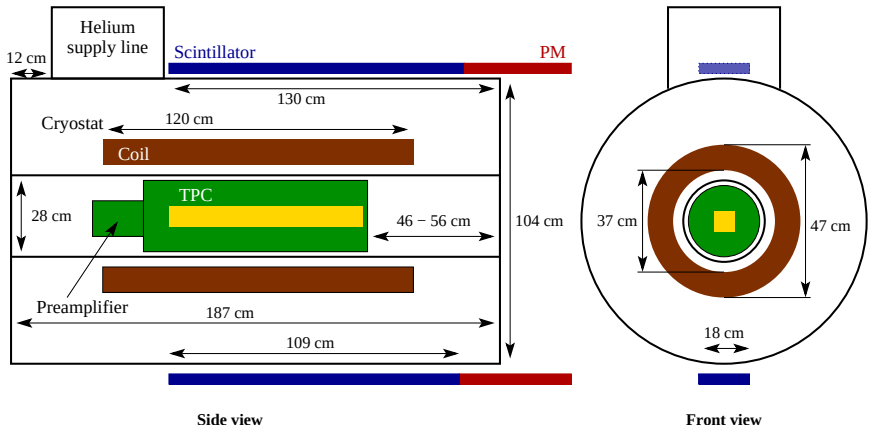


Figure 3.3: Sketch of the magnet test stand with the TPC prototype including dimensions (figure from [Lux05]).

The electronics used for the readout of the pad signals have been developed for, and used in the ALEPH experiment at LEP [Bow95]. Since it was used originally for a proportional wire amplification system it has been modified to fit the needs of the MediTPC measurement setup [BNJW04]. The signal of the pads gets first to the time-integrating pre-amplifiers, which have a time constant of 2 $\mu$s. The form of the amplified signal describes a fast increase followed by an exponential decrease. In the next step, this signal is changed by the *Shapers* into a Gaussian shape, which shortens the long tail. The differential shaper signal has a length of about 400 ns and is converted into a digital signal by the Time Projection Digitizer (TPD). The *Flash Analog Digital Converters* (FADC) in the TPDs have a sampling rate of 12.5 MHz, so that a time step of 80 ns results.
The TPD is read out and controlled by a Fast Intelligent Controller (FIC 8234), which sends the data to a PC where they are saved for the later analysis.

## 3.2 Measurement Runs

In all measurement runs used in this work the trajectories of cosmic muons have been measured. Primary cosmic radiation is produced in stars and the secondary radiation in the interaction processes with the atmosphere. Muons pose the largest fraction of charged particles that reach the earth surface. The mean energy of the muons is 4 GeV and their spectrum results from the energy spectrum before the production and the decay rate and energy loss on their way through the atmosphere.

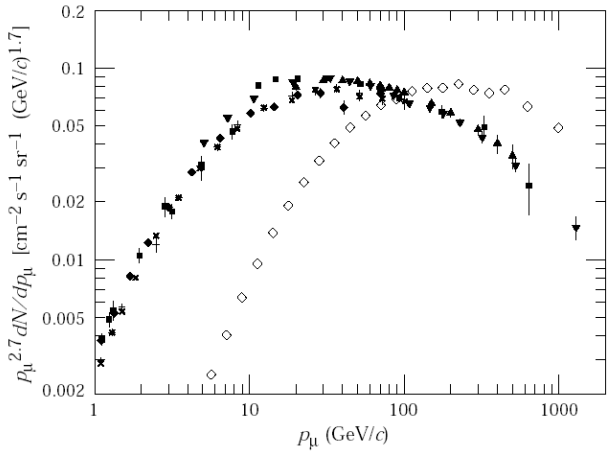


Figure 3.4: Spectra of cosmic muon on sea level for angles of incidence $\theta = 0°$ (solid markers) and $\theta = 75°$ (open markers) (figure from [Par02])

Figure 3.4 shows two muon spectra for two angles of incidence $\theta$ relative to the plumb line: $\theta = 0°$ and $\theta = 75°$. Since larger angles correspond to a longer way through the atmosphere, the spectrum gets shifted to higher energies at a larger angle because more low-energy muons decay. This is due to the effect that the high-energy muons are faster and therefore the relativistic time dilation is larger.

After passing the first trigger, the cosmic muons have to travel through the magnet test stand and the TPC prototype before they reach the second trigger and a coincidence signal triggers the readout. An estimation of the material budget between the two triggers leads to a minimal energy of the registered muons (see [Jan04]):

$$\left(\frac{dE}{dx}\right)_{min} \cdot \rho \cdot l \approx 230\text{MeV}\,, \tag{3.1}$$

where $\rho = 7.87\frac{\text{g}}{\text{cm}^3}$ is the density of iron and $l$ the thickness the muons have to pass (here the simplification has been made that the joke and the coil of

the magnet consist completely of iron). The geometry of the setup leads to a second energy limit in a magnetic field which is given by the curvature of the trajectory and the restriction that the muon has to pass both triggers. This leads to a minimal momentum of about 1 GeV/c in a magnetic field of 4 T (see [Jan04]).

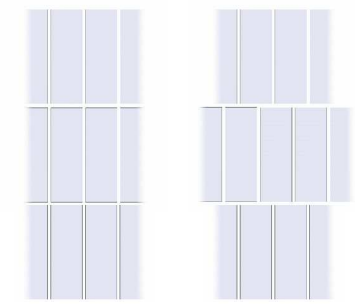

(a) non-staggered (b) staggered

Figure 3.5: Sketch of the used pad layouts.

Several measurement runs have been taken with the measurement setup in the magnet test stand. The first measurements were done with TDR gas (93 % Argon, 5 % $CH_4$, 2 % $CO_2$), which was optimized for the conditions described in the TESLA Technical Design Report [Col01]. For reference, P5 gas (95 % Argon, 5 % $CH_4$) has been used as a second gas mixture in later measurements.
In the measurements using TDR gas, both a staggered and a non-staggered pad layout have been used (see Figure 3.5). These layouts have been chosen because they represent the two extreme pad row alignments which will be realized in a circular readout plane in a large TPC detector. The P5 measurements were done only for the staggered pad layout.
For all setups described before, measurement runs were done for the four magnetic field strengths of 0, 1, 2 and 4 T.

Table 3.1 lists values of the used drift field, the resulting drift velocity $v_D$ and the diffusion and defocussing coefficients $D$ and $\sigma_0$ for the MediTPC setup with the two gas mixtures. The pressure of the setup is in all cases 1 bar. The diffusion and defocussing coefficients are listed for different magnetic field strengths and are defined by the following equation for the width $\sigma$ of the signal:

$$\sigma^2 = D^2 L + \sigma_0 \,. \tag{3.2}$$

The listed values show that, with a magnetic field, in TDR gas the diffusion is larger while the defocussing is smaller than in P5 gas.

| **Gas Mixture** | | | **TDR** 93:5:2 (Ar:$CH_4$:$CO_2$) | **P5** 95:5 (Ar:$CH_4$) |
|---|---|---|---|---|
| E-Field | $[\frac{\mathrm{V}}{\mathrm{cm}}]$ | | 203 | 92 |
| Velocity $v_D$ | $[\frac{\mathrm{cm}}{\mu\mathrm{s}}]$ | | 4.4 | 4.1 |
| Diff. Coeff. $D$ | $[10^{-4}\mathrm{mm}]$ | at 0 T | 202.00 | 571.00 |
| | | at 1 T | 34.10 | 24.50 |
| | | at 2 T | 11.50 | 7.24 |
| | | at 4 T | 3.00 | 1.92 |
| Defoc. Coeff. $\sigma_0$ | $[\mathrm{mm}^2]$ | at 0 T | 0.180 | 0.288 |
| | | at 1 T | 0.142 | 0.227 |
| | | at 2 T | 0.110 | 0.190 |
| | | at 4 T | 0.070 | 0.140 |

Table 3.1: Parameters of the MediTPC measurement setups.

As mentioned before, the outer pads have been connected with the surrounding metal plane to avoid cross-talk. This setup did not work perfectly and therefore on each side one additional column has been excluded from the analysis. In the top and the bottom row the same problem arises, but due to reasons discussed in Section 5.3.1, they have been used nevertheless in some of the studies.

An arriving charge cloud of a signal produces an induction signal before reaching the pad plane (see Figure 3.6.a). This signal is much broader than the electron signal and therefore its maximum is much smaller. So it has no big effect on the small pads. On the surrounding metal plane, which has a much larger area than the pads, this signal is integrated over a larger area and the induced electric signal is strong enough to cause cross-talk with the outer pads.
This causes the effect that the signals on the outer pads are usually measured earlier than the signals on the inner pads and show a broader structure, which leads to a less accurate and reliable hit reconstruction.
Figure 3.6.b shows a Lego diagram of the number of pulses on a pad integrated over the time of a measurement run. Here the excess of pulses on the outer pads is visible as well as some "damaged" pads, where no pulses are registered, in the central region. In all measurement runs some of the pads were not working. They are referred to as damaged pads. The damaged pads can easily be found in diagrams like in Figure 3.6.b. They are taken into account during the reconstruction process by including the information in the MultiFit configuration (see Section 4.1).

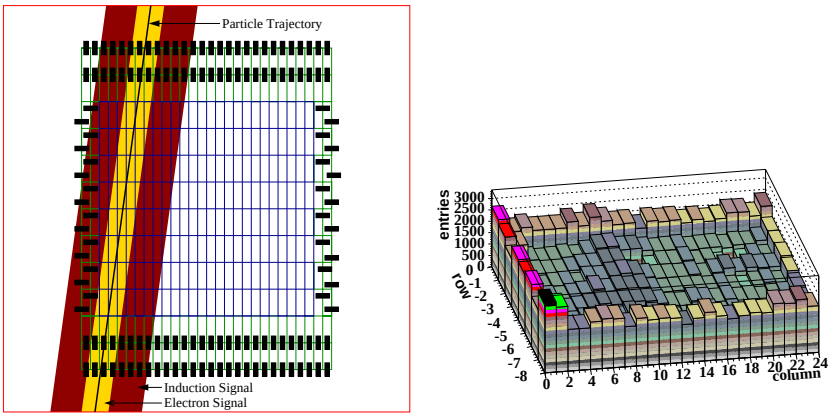


(a) (b)

Figure 3.6: Cross-talk between outer pads and surrounding plane:
a) electron (yellow) and induction signal (red) on the pad plane and the surrounding plane (figure from [Jan04])
b) number of pulses per pad integrated over a measurement run (figure from [Lux05]).

## 3.3 Monte Carlo Simulation

The Monte Carlo simulation has been used in several analyses of the reconstruction methods in this work. Its main advantages are that in the simulated data the true track trajectory is known[1]. This makes some examinations possible which help in the understanding of the effects of several reconstruction techniques. In addition, the simulation was used to analyze the effects of a different pad setup with more rows and the effect of the damaged pads. In future studies it will be used to analyze the effects of different pad shapes and sizes as well of longer drift distances.

The simulation works in several steps. In the first step the incident particles are simulated. Here the simulation of electrons in a test-beam setup (fixed mass, momentum and straight tracks at defined angle and position) and the simulation of cosmic muons are possible.
The *muon generator* simulates cosmic muons with realistic angular and energy spectra. The angular spectrum is the one used in the BaBar simulation [Bri] and the energy of a generated muon is read in from a list that has been produced by a CORSICA simulation [HKC+98].

[1] This is not the case in the measured data since the setup does not contain an external reference like a hodoscope.

After this step the trigger setup and the geometry of the chamber is taken into account to filter the relevant muons trajectories. The simulated trajectories are straight tracks, even in a setup with a magnetic field.

In the following steps, the gas properties like the mixture, the water content and the pressure are taken into account. The primary ionization along these tracks is simulated with HEED [Smi]. In this process the effects of the electric and magnetic field are not considered which leads to straight tracks and a field independent, three-dimensional distribution of the resulting electron cloud. The resulting drift velocity of the electrons and the diffusion coefficients are simulated with GARFIELD [Vee84, Vee98] (here the electric and the magnetic field are considered).

The position evolution of these primary electrons in the drift field is done separately for every electron and a Gaussian smearing is used in each of the three dimensions:

$$\begin{aligned} x_i' &= x_i + RND_{Gauss} \cdot \sqrt{l_{drift}} \cdot C_{diff}^T \\ y_i' &= y_i + RND_{Gauss} \cdot \sqrt{l_{drift}} \cdot C_{diff}^T \\ z_i' &= z_i + RND_{Gauss} \cdot \sqrt{l_{drift}} \cdot C_{diff}^L \,, \end{aligned} \tag{3.3}$$

where $x$, $y$ and $z$ denote the coordinates of the electron $i$ before the smearing, the primed coordinates denote the positions after the smearing, $RND_{Gauss}$ denotes a Gaussian distributed random number, $l_{drift}$ the drift length and $C_{diff}^T$ and $C_{diff}^L$ the transverse and longitudinal diffusion coefficients.

The electrons reaching the first GEM are "forced" into the closest GEM hole, where the amplification is simulated by applying an effective gain value which is smeared with a Polya distributed random number. Usually, the value of the effective gain is adjusted in several iterations by comparisons of the measured charge between the Monte Carlo results and the measured data.

The new electrons, that are produced during the amplification, are smeared flat inside the GEM hole. The position smearing (see Equation 3.4) is applied again for the drift between two GEMs and these processes are repeated for the three GEMs. Figure 3.7 shows two examples to illustrate the evolution of the electron cloud.

After the GEM amplification the produced electrons are drifted to the pad plane (here the smearing algorithm from Equation 3.4 is applied again), where they are collected on the pads. Here different pad layouts and sizes can be simulated. This process is followed by a simplified simulation of the readout electronics. A more detailed description of the working principle of the Monte Carlo simulation will be included in the forthcoming PhD thesis of A. Imhof.

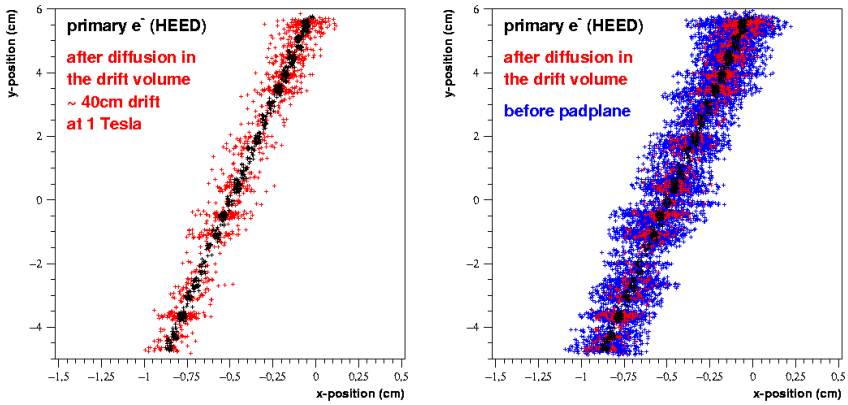


(a) after 40 cm drift, before GEMs

(b) after amplification, before pad plane

Figure 3.7: Diffusion evolution of the electron cloud during drift in Monte Carlo simulation for a magnetic field of 1 T (figure from [Imh06]):
black crosses: primary electrons from HEED; red crosses: electrons after drift; blue crosses: electrons after amplification.

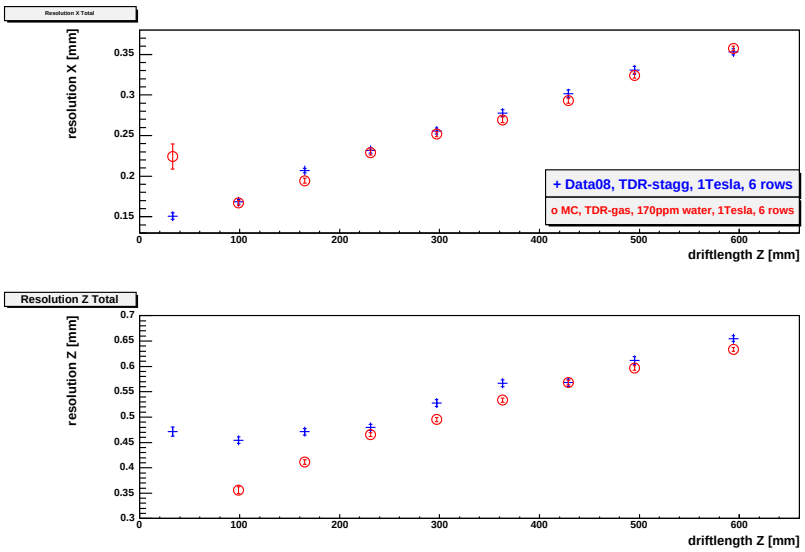


Figure 3.8: Comparison of point resolution results between a measurement (blue crosses) and Monte Carlo simulation (red circles) for TDR gas and 1 T magnetic field; six rows used in the reconstruction (figure from [Imh06]).

The Monte Carlo simulation is still under development. To illustrate the performance of the current status, some results are presented here. A comparison of the point resolution (see Section 4.2) resulting from an analysis of a measurement and simulated data is shown in Figure 3.8. The agreement is quite good for the $x$ resolution, except at the shortest drift distances, while a discrepancy can be seen in the $z$ resolution at short drift distances. The cause of the disagreement in the $z$ resolution is topic of an ongoing study. Figure 3.9 shows a comparison of the signal width between a measurement and a simulation. The comparison shows a quite good agreement.

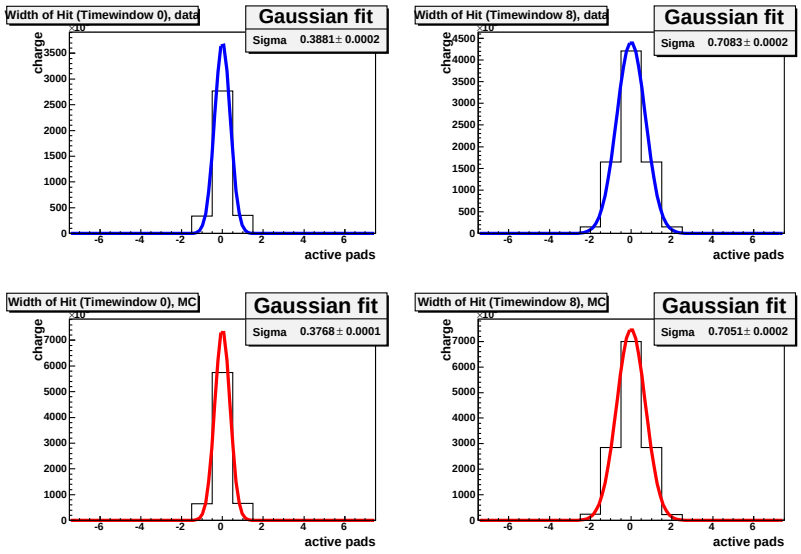


Figure 3.9: Comparison of signal width between measurement (top, blue) and Monte Carlo simulation (bottom, red) for two different drift distance ranges: left side 0-75 mm, right side 525-600 mm; values for TDR gas and 1 T magnetic field (figure from [Imh06]).

The Monte Carlo data used in this work has been produced for P5 gas with 0 ppm water content, a staggered pad layout and for two magnetic fields of 2 and 4 T. Since the water content was set to zero and no extensive adjustment to the measured data was made, the results do no reflect the measurements perfectly. The main goal of the study was to analyze systematics in the used methods and for this task the simulated data were sufficient.

# Chapter 4

# Analysis Methods

In this chapter, the reconstruction software MultiFit and methods for the point resolution calculation are described.

## 4.1 MultiFit: Reconstruction and Analysis Software

The fitting software *MultiFit* has been developed within the scope of the diploma thesis of M.E. Janssen [Jan04] and is maintained by him. Its main task is to reconstruct particle tracks from measured charge signals and to calculate the values that are needed in the analysis of the detector performance. The software package has been designed to be adjustable to different prototype layouts and to be able to reconstruct multiple tracks in one event. Furthermore is provides detailed output on the reconstruction to have the possibility to analyze the effects and systematics of the reconstruction process and the detector.

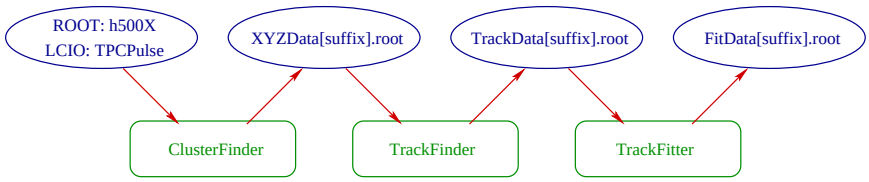


Figure 4.1: The reconstruction modules of the fitting software MultiFit (figure taken from [Jan04]).

The MultiFit software is written in C++ and makes use of the ROOT [ROOT05] and the LCIO ("Linear Collider I/O", [LCIO05]) frameworks, which are both necessary for compilation and running the program. The data input formats are the ROOT and LCIO based data formats, the output is written in the ROOT format. The reconstruction is implemented as a three step process (see Figure 4.1):

**ClusterFinder:** row-wise reconstruction of primary charge depositions by combination of measured charge signals and three-dimensional position calculation

**TrackFinder:** finding of particle tracks and basic reconstruction by combining the points from the ClusterFinder module

**TrackFitter:** track fitting and calculation of the track parameters and the values needed for further analysis

Each of the software modules belonging each to one of the three reconstruction steps, writes its results in a separate output file. The modules need only the data of the previous module as input and run independently otherwise. The reconstruction steps and the implemented algorithms will be described in further detail in the following sections.

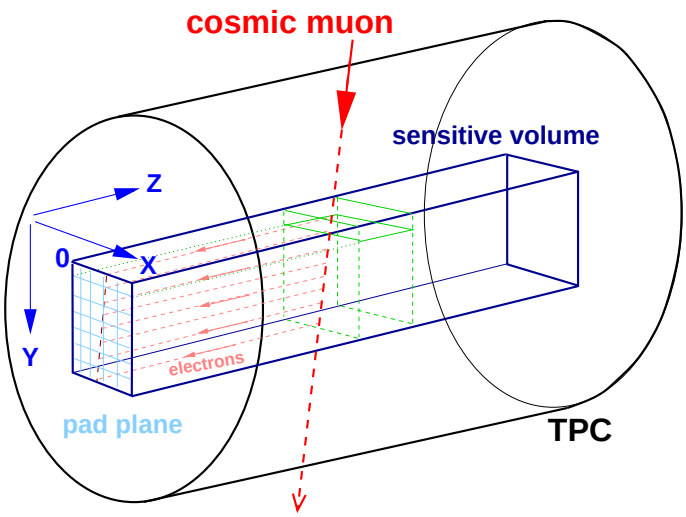


Figure 4.2: The coordinate system used in the calculations of MultiFit together with a sketch of the TPC prototype.

The coordinate system used for the calculations in MultiFit is shown in Figure 4.2, together with a sketch of the TPC prototype for an easier allocation. It's a right-handed coordinate system, where the $z$ axis runs along the drift direction of the electrons in the TPC, the $x$ axis runs parallel to the pad rows and the $y$ axis perpendicular to them. The origin of this coordinate system lies in the top left corner of the pad plane.

The different steering parameters needed for the reconstruction are given to MultiFit in a configuration file. This file contains the informations on the pad geometry and layout, parameters and limits for the different algorithms used in the reconstruction process, information on the input and output files and data on the details of the measurement like the drift velocity, pedestals and calibration factors for each pad, the scale of the ADC information and – if needed – gas properties like diffusion and defocussing coefficients. A detailed description of the possible input parameters can be found in [Jan04].

To be able to monitor the reconstruction process and to examine single events, MultiFit provides the possibility to switch on a graphical display which shows the process event-wise in a window on the screen and gives the possibility to save screenshots to files in various output formats (Postscript, EPS, Gif and ROOT C-script or data file).

### 4.1.1 MultiFit ClusterFinder

In the first reconstruction step, *the ClusterFinder*, the measured charges on the pads are being combined pad-wise to *pulses* for every event. A "pulse" denotes the time-integrated charge deposition (the sum over all charge signals belonging to the pulse in the $z$ direction) of the primary ionization of one track on a pad.

The input for this reconstruction process are the ADC output data of the charge deposition, the number of the pad channel and the time information. The mapping of the ADC channels to the pad positions is set in the configuration file. In addition, single pads can be declared as damaged, so that signals measured on these pads will be neglected and these pads will be treated specially in the reconstruction process. Other parameters are the pitch and the layout of the pads as well as the length of the ADC timing interval and the scaling factor between charge and ADC counts.

With these inputs each channel number gets assigned to a pad. The $z$ coordinate of the ADC signal can be calculated from its timing information and the drift velocity. The pulses are detected pad-wise by searching for values that rise above a certain threshold. For this threshold different values for the beginning and the end of a pulse can be chosen. Additionally to the $z$ bins, that are between the two threshold limits, some bins before and after can be added to the pulse. The number of bins that get added before and after the threshold limits can be set independently from each other in the

configuration file. From the resulting collection of bins the integrated charge of the pulse and its time information (respectively $z$ coordinate), which is set to the inflexion point of rising slope (= mean of positive derivative), are determined. This process is illustrated in Figure 4.3.

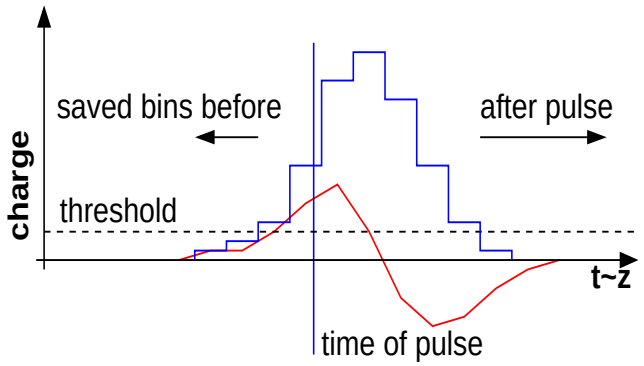


Figure 4.3: Illustration of the pulse reconstruction in MultiFit (figure from [Jan06]).

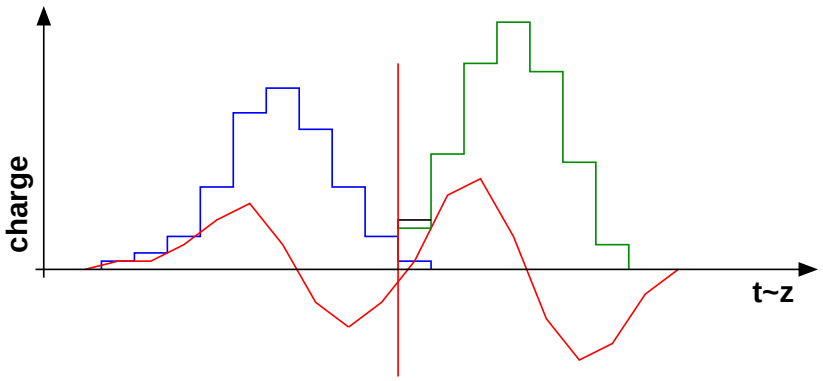


Figure 4.4: Illustration of the pulse separation in MultiFit (figure from [Jan06]).

For events in which two pulses overlap or follow each other very closely, a separation algorithm has been implemented: During the pulse search the change in the slope is detected and the $z$ coordinate of the zero-crossing of the derivative is taken to be the boundary between the two pulses (see Figure 4.4). In this process variations in the order of a noise parameter are being ignored.

These pulses are then combined to *hits*, which are the (in the $x$ direction) integrated charge information of the pulses in one pad row, that belong to the primary ionization. In this row-wise process the charge deposition and the three dimensional position of the hit are being determined.

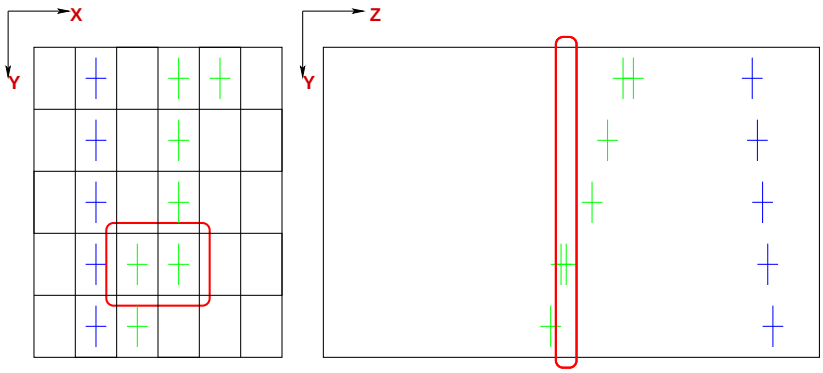


Figure 4.5: Illustration of the hit reconstruction in MultiFit (figure taken from [Jan04]).

The hit search algorithm starts at the pulse with the highest charge. In the following, only pulses that lie inside a certain time window around that pulse are being considered. The size of the time window can be set in the configuration file. A large time window has an influence on the ability to separate two tracks, and a small time window could lead to the erroneous separation of pulses belonging to the same hit in the $z$ direction. Starting from the central pulse, the algorithm searches for smaller pulses, that are not already assigned to another hit, which are then added to the *hit collection*. In this process the error $\sigma$ of the charge information $Q$ is taken into account:

$$Q_{pulse} - F \cdot \sigma_{Q,\,pulse} \overset{!}{<} Q_{central\ pulse} + F \cdot \sigma_{Q,\,central\ pulse} \tag{4.1}$$

where $F$ can be set by the user. Like the size of the time window, $F$ should be small enough to be able to separate hits from different tracks, but large enough to ensure no erroneous separation due to fluctuations in the statistics of primary electrons. Every new pulse, that has been added to the hit, is used as a new starting point for this algorithm to search for the next pulses belonging to the hit. The time window is not changed during this process. Pads that have been marked damaged, get assigned a fake charge and time information that corresponds to the central hit of the current algorithm cycle. During the merging process these fake pulses get assigned to the hit and serve as a starting point for an separate algorithm cycle.

When no more pulses can be added to the hit, the search algorithm stops and the coordinates of the hit are being calculated. The vertical center of the row is taken as $y$ coordinate. The $x$ coordinate of the hit is calculated by a *Center of Gravity* method, that uses the charge informations $Q_{i,\,pulse}$ and the $x$ positions $x_{i,\,pulse}$ of the pulses:

$$x_{hit} = \frac{\sum_i^{pulses} [\, Q_{i,\,pulse} \cdot x_{i,\,pulse} \,]}{\sum_i^{pulses} Q_{i,\,pulse}} \,. \tag{4.2}$$

The $z$ coordinate of the hit is being calculated by the same method from the time information of the single pulses. The error of the coordinates is derived from the error of the charge information. For the $z$ coordinate, the errors of the time informations of the pulses are also taken into account. The fake charge and time information from damaged pads are not being considered during the coordinate calculation and are being deleted after the hit reconstruction. However their number gets included in the error calculation of the coordinate to take into account the uncertainty due to the missing information:

$$\sigma_{x,\,hit} \;=\; \sigma_{x,\,hit} \cdot \frac{N}{N-M} \tag{4.3}$$

with $N$ : number of pulses in the hit collection
$M$ : number of damaged pads

The described hit reconstruction method is called *HitMerge* method. To avoid confusion in respect to the *Center of Gravity* method and naming conventions in former publications about MultiFit, it should be stated, that in older versions of the ClusterFinder another hit reconstruction method was implemented, that was called the *CenterOfGravity* method. Since the HitMerge method yields better results regarding the $z$ resolution and is less CPU-intensive, the *CenterOfGravity* method has been removed from MultiFit. In this work the expression "Center of Gravity" is only used for the described calculation of the $x$ positions within the HitMerge method.

The most recent change in the ClusterFinder is the implementation of a Pad Response Correction in the calculation of the $x$ position of a hit. This method takes into account the dependency of the measured pad signals on the width of the charge cloud and the pad geometry. In the case of narrow charge clouds it yields more accurate results for the $x$ position of a hit. The Pad Response Correction, the reasons for its implementation and its effects are described in detail in section 5.1.2.

### 4.1.2 MultiFit TrackFinder

The second software module of MultiFit is the *TrackFinder*. In this step particle tracks get detected and the hits are combined into a track collection. The implemented search algorithm assumes an approximately straight track, that enters the chamber from the top and crosses the top and bottom side of the sensitive volume. This assumption is valid since the particle tracks of the observed cosmic muons in the used magnetic fields have a minimal radius of 900 mm, which corresponds to a curvature of about $1.1\,\mathrm{m}^{-1}$ and over the height of the sensitive volume ($\approx$50 mm) to a maximum sagitta of 340 $\mu$m (see Section 4.2 and Appendix B of [Jan04]). Deviations of this order of magnitude do not have an influence on the track-finding algorithm.

The search algorithm uses a so-called *track following* method. Since the particle trajectories are assumed to run vertical in the $xy$ projection, the implementation of this algorithm works row-wise. It is initialized by choosing two hits and then fitting a three dimensional straight track hypothesis to them. Based on the track hypothesis the most probable position of the next hit is calculated and the algorithm searches for hits in the next row, that lie inside in a search window around that position and that are not already assigned to another track. The size of the search window can be set separately for the $xy$ and the $yz$ projections in the configuration file[1]. If more than one hit is found inside this area, the hit, for which a straight line fit including that hit results in the smallest $\chi^2$, is chosen, where:

$$\begin{aligned} \chi^2 \;&=\; \chi^2_{xy} + \chi^2_{yz}\ \text{, with: } \chi^2_{xy} = \chi^2 \text{ of the } xy \text{ track projection} \\ &\qquad\qquad\qquad\qquad\quad \chi^2_{yz} = \chi^2 \text{ of the } yz \text{ track projection}\,. \end{aligned} \tag{4.4}$$

In the next step a new track hypothesis is calculated including the newly added hit and the algorithm searches for the next hit to be included. If no hit is found inside the search window or all hits that are found result in a probability below a certain limit, the algorithm counts this as a missing hit and continues its search in the next row. When the last row is reached, the algorithm starts again in the opposite direction to find hits above the upper initialization hit. The algorithm is started with any two hits, that meet the configurable boundary conditions of a maximum and minimum distance. Besides that, the maximum of successive rows without a hit and the minimum of hits a track must have to be saved can be set.

[1] As before, the chosen search window size influences the ability of two track separation as well as erroneous splitting of one track into two.

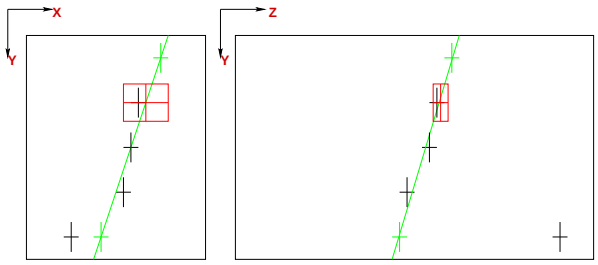


(a) Initialization hits and first track hypothesis (in green) and first search window (red rectangle)

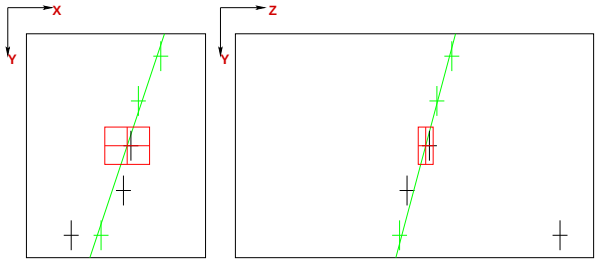


(b) Track hypothesis resulting from newly added hit (green) and next search window (red rectangle)

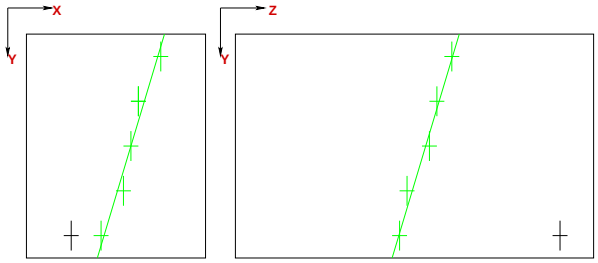


(c) Completed track collection (green)

Figure 4.6: Illustration of the track following algorithm (figures from [Jan06]).

This track following algorithm is illustrated in Figure 4.6. On the left side, the $z$ and on the right side the $x$ projection of the track is shown. The hit positions are illustrated by "+" symbols. 4.6.a shows the two hits used for initialization, the track hypothesis based on these two hits and the first search window. The next step with the track hypothesis including the newly added hit and the next search window is shown in 4.6.b. The complete resulting track collection is shown in 4.6.c.

### 4.1.3 MultiFit TrackFitter

In the TrackFitter module a selectable hypothesis for the track shape is fitted to the track collections, that have been combined by the TrackFinder. In MultiFit two different track fitting methods are implemented: the *Chi Squared Method*, which is based on a chi-squared minimization method, and the *Global Fit Method*, which is based on the maximization of a likelihood function describing the track. Both methods are implemented for a straight as well as for a curved track assumption, so that data taken with and without magnetic field can be fitted appropriately. The implemented, selectable fit methods are:

**ChiSquared:** Analytical $\chi^2$ minimization of a straight line fit both in the $xy$ and in the $yz$ projection. Results: position of crossing point of the track and the $xz$ plane at $y = 0$ (intercept) and slope in $xy$ and $yz$ planes.

**ChiSquaredRoot:** Numerical $\chi^2$ minimization of a straight line fit in the $xy$ as well as in the $yz$ projection using methods from the ROOT framework. Results: intercept and slope in $xy$ and $yz$ planes.

**ChiSquaredCurved:** Numerical $\chi^2$ minimization of a circular arc fit in the $xy$ and a straight line fit in the $yz$ projection using methods of the ROOT framework. Results: curvature and center of circle in $xy$ plane, intercept and slope in $yz$ plane. Additionally the intercept and the slope in the $xy$ plane are calculated from the fitted curvature and center of the circle.

**GlobalStraight:** Numerical log likelihood maximization of a fit function describing the charge distribution of a straight track in the $xy$ and a $\chi^2$ minimization of a straight line fit in the $yz$ projection using methods of the ROOT framework. Results: intercept, slope in $xy$ and $yz$ planes, width of the charge cloud $\sigma$.

**GlobalCurved:** Numerical log likelihood maximization of a fit function describing the charge distribution of a curved track in the $xy$ and a $\chi^2$ minimization of a straight line fit in the $yz$ projection using methods of the ROOT framework. Results: intercept, slope and curvature in $xy$ plane, intercept and slope in $yz$ plane, width $\sigma$ of the charge cloud of the track in the $xy$ plane at $z = 0$. Additionally the center of the circle in $xy$ plane is calculated from the fitted values.

A detailed description of the Chi Squared Method is given in section 5.1. The Global Fit Method including its underlying principle, the fit function

and its effects and results is described in detail in section 5.2. In addition to the track parameters, the distance and the residuals (see section 4.2) of the hits belonging to a track are being calculated. Furthermore, if in one event more than one track has been reconstructed, the minimum of the distance of hits belonging to two separate tracks will be calculated and saved.

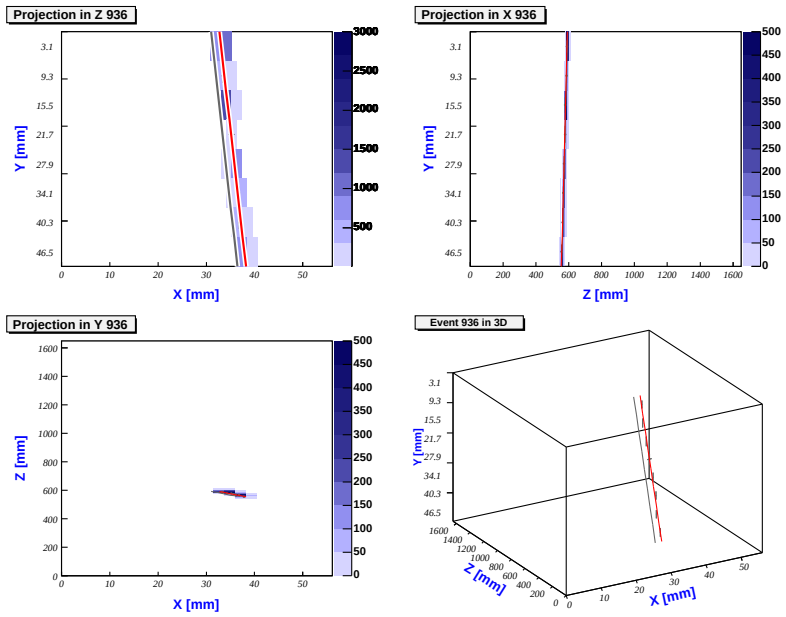


Figure 4.7: Event display of the TrackFitter

Figure 4.7 shows an event display of the track fitting module. The display shows the different projections in the $xy$, the $xz$ and the $yz$ plane and a three dimensional view of the event. The reconstructed pulse charges are shown in different colors and the hit positions are drawn as "+" signs. The fitted track is drawn as a red line and, if the reconstruction is based on Monte Carlo data, the Monte Carlo truth is drawn as a black line (for this example an Monte Carlo event has been chosen, in which the fitted track has been reconstructed in some distance from the Monte Carlo track, so that both lines are clearly visible).

## 4.2 Point Resolution

The parameters that have an influence on the achievable resolution of a TPC are the gas and field properties, the gas amplification and the readout system. In the $r\phi$ plane the transversal diffusion and defocussing, which depend on the gas and the magnetic and electric fields, the pad size, geometry and layout set limits on the possible resolution. In the $z$ direction the longitudinal diffusion, the signal shape after the gas amplification and the timing of the readout electronics set the limits.

A problem that arises in the definition of the resolution is, that in the used prototype setup no external reference for the real position of the particle trajectory, like for example a hodoscope, is included. Therefore the resolution estimates have to be derived from the fitted track parameters and the reconstructed hit positions, that are spread around the track following a Gaussian distribution. The width of this Gaussian is a measure for the single point resolution. But since the real track is not known, the definition of the distance between a hit and the track is not straight forward. To solve this problem several methods, that will be explained in the following, have been under consideration.

### 4.2.1 The Triplet Method

This is a very simple, robust and easy to understand method. Its advantages lie in the fact, that systematics can be seen and understood very well.
To determine the resolution, the residuals of the hits are calculated. The residual of a hit is defined here as the distance in the $x$ direction a hit has to a straight line that is drawn through the two adjacent hits in the row above and below (see Figure 4.8). Then a Gaussian is fitted to the distribution of the residuals. If one assumes that the error of all three hit coordinates is the same, the point resolution results from:

$$\sigma_{res} = \sqrt{\frac{2}{3}} \cdot \sigma_{Gaussian} \ . \tag{4.5}$$

Due to its principle, the triplet method can only calculate residuals for hits that are not in the top or bottom row. The same applies for tracks, that contain missing hits. Here the residuals of the hits next to the row with the missing hit can't be calculated.

Several cuts can be applied to the input data, to make the results more reliable. The $x$ region of considered tracks can be limited by a range on the left and right side of the sensitive volume, that is as broad as half of the maximum expected width a charge cloud can have after the amplification.

This ensures that the $x$ position of the hits belonging to these tracks are well reconstructed, since their complete charge deposition has been detected and taken into account for the position reconstruction. Further hits that contain damaged pads can be filtered out. And finally, the maximum number of tracks reconstructed in one event can be set to one to filter out noisy events.

The triplet method does not always provide the most accurate results, as the track and the straight line used for the residual calculation do generally not coincide (see Figure 4.8). This is especially valid for curved tracks.

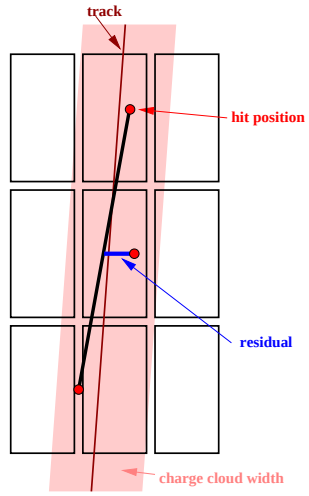


Figure 4.8: Triplet Method: sketch of residual definition (figure from [Lux05]).

### 4.2.2 The $\chi^2_{res}$-Method

Another possible method to determine the point resolution from the reconstructed data is the $\chi^2_{res}$-method[2]. This method makes use of the minimized $\chi^2$ of the reconstructed tracks. Since the $\chi^2_{res}$-method uses the information of the whole track, a study of row-wise effects is not possible.
For the mean of the $\chi^2$ the following relation applies:

$$\langle \chi^2 \rangle = \left\langle \sum \frac{(f(x_i) - x_i)^2}{\sigma_i^2} \right\rangle = F = N_R - N_P \,, \tag{4.6}$$

[2]To avoid confusion with the $\chi^2$-method used for track fitting, the $\chi^2$-method for the point resolution determination is denoted here with the subscript "$res$".

where $f(x)$ denotes the fit function, $x_i$ the hit coordinates with error $\sigma_i$ and $F$ is the number of degrees of freedom, that results from the difference of the number of rows $N_R$ and the number of free parameters of the fit function $N_P$ ($N_P = 2$ for a straight line fit and 3 for a curved fit).
Assuming that the resolution of all hits and therefore their errors are approximately the same, which means $\sigma_i = \sigma \,\forall\, i$, it follows:

$$\widetilde{\chi}^2 = \chi^2 \cdot \sigma^2 \quad \text{, with} \quad \widetilde{\chi}^2 = \sum \left(f(x_i) - x_i\right)^2 . \tag{4.7}$$

So $\widetilde{\chi}^2$ denotes a $\chi^2$ calculated with all errors set to 1. The same linear relation that holds for the $\chi^2$ holds for its mean:

$$\left\langle \chi^2 \right\rangle = F = \left\langle \widetilde{\chi}^2 \right\rangle / \sigma^2 \quad \Rightarrow \quad \sigma^2 = \left\langle \widetilde{\chi}^2 \right\rangle / F \, . \tag{4.8}$$

This means, that if the number of degrees of freedom is known, the resolution can be calculated from the mean value of $\widetilde{\chi}^2$. If the $\chi$ is replaced by $(\chi/\sigma)$ in the $\chi^2$ distribution:

$$P\left((\chi/\sigma)^2, n\right) = \frac{2^{-\frac{F}{2}}}{\Gamma(\frac{F}{2})} (\chi/\sigma)^{F-2} e^{-\frac{(\chi/\sigma)^2}{2}} \tag{4.9}$$

and the resulting distribution is fitted to the $\widetilde{\chi}^2$ distribution, the point resolution $\sigma$ can be determined directly. In this fit the normalization factor also has to be set as a free parameter, since the scaling by the factor $\sigma$ affects it in a non-trivial way.

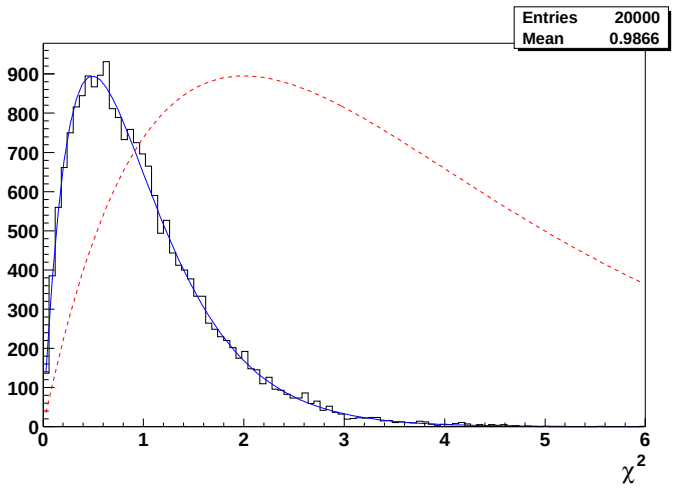


Figure 4.9: Point Resolution by Chi Squared Method: fit of the $P\left((\chi/\sigma)^2, n\right)$ distribution (figure taken from [Jan04]).

Figure 4.9 shows as an example a $\chi^2$ distribution that has been calculated from 20,000 straight line fits to straight tracks, which have been simulated and which each contain six hits that have a spread of 0.5. The errors of the hit positions have been set to 1 and and the parameter $F$ equals 4 (since $N_R = 6$ and $N_P = 2$). The result of the fit of $P\left((\chi/\sigma)^2, n\right)$ to the distribution is drawn as a blue, solid line and the red, dotted line shows the expected distribution $P\left(\chi^2, 4\right)$ with the same normalization factor. The scaling by the factor $0.5^2 = 0.25$ is clearly visible.

### 4.2.3 The Geometric Mean Method

Here "*distance*" denotes the difference between the $x$ coordinate of a hit and the reconstructed track at the same $y$ coordinate, when the hit is included in the track fit. "*Residual*" denotes the difference between the $x$ coordinate of the hit and the track, that has been reconstructed excluding this hit. In the reconstruction excluding the hit, all track parameters are fitted again. The horizontal lines in Figure 4.10 show the definition of the distance and of the residual used in MultiFit together with the reconstructed tracks belonging to these values. In the point resolution calculation the values are multiplied with $\cos(\varphi)$ to get the minimal distance and residual between the hit and the track ($\varphi$ denotes the angle of the track to the $y$ axis).

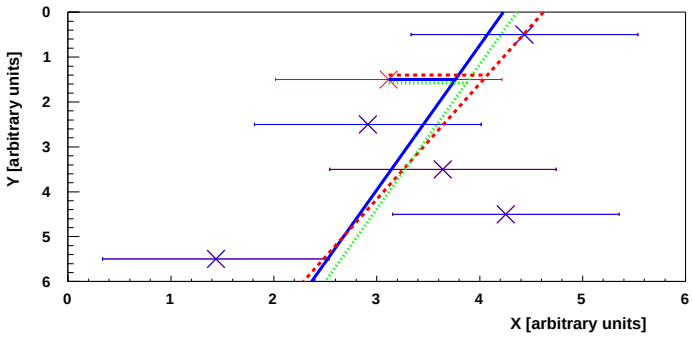


Figure 4.10: Distance (blue, solid) and residuals with one parameter (green, dotted) and all parameters refitted (red, dashed); (figure taken from [Jan04]).

Since the hit coordinates generally do not lie exactly on the reconstructed track, the distance usually will give smaller results than the true deviation of the hit from the track, because the considered hit "pulls" the reconstructed track in the direction of its deviation. In contrast, the residual will give

larger values, since the track reconstructed without the hit is "pulled" away from the hit by the remaining hits (see section 5.3 in [Jan04]). So the distribution of the distance has a smaller width and the distribution of the residual a larger width than the distribution of the deviation of the hits from the true track position. The calculation included in the Appendix A of [C$^+$05] proves analytically for straight tracks, that the geometric mean of both widths gives the true resolution:

$$\sigma = \sqrt{\sigma_{distance} \cdot \sigma_{residual}} \quad . \tag{4.10}$$

For curved tracks a simple Monte Carlo Simulation has been used. This simulation produced curved tracks with a radius between 500 mm and 2000 mm. The tracks go through the center of the sensitive volume and no pad effects have been included. The result is shown in Figure 4.11: As expected the residuals are in general too large while the distances are too small. The geometric mean of both reproduces the Monte Carlo truth correctly.
This way to determine the single point resolution, which is in this context often referred to shortly as "resolution", is called the *Geometric Mean Method*.

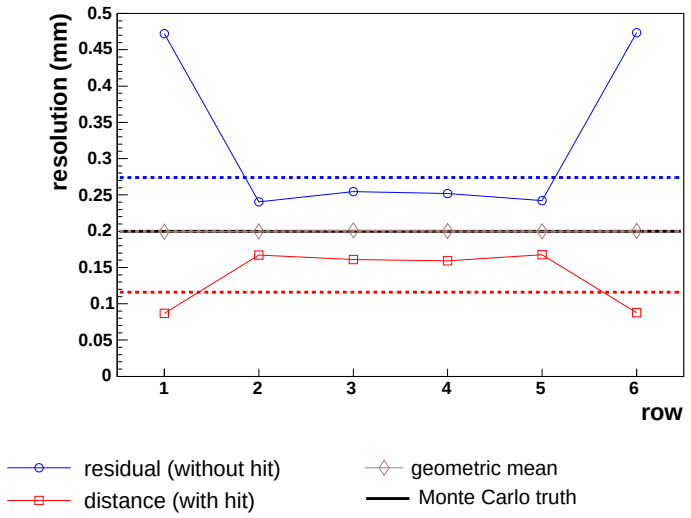


Figure 4.11: Point Resolution: distance, residual and geometric mean for curved Monte Carlo tracks (figure taken from [Jan06]).

Since the Geometric Mean Method gives very reliable resolution results as well as the possibility to examine row-wise effects, it is used for the single point resolution calculations in this work and, if not stated otherwise, all resolution values and plots shown in the following sections have been calculated using this method.

# Chapter 5

# Track Fit Methods

The high resolution needs in a TPC for the ILC and the GEM amplification technique with its narrow signal widths pose new requirements on the reconstruction methods. Therefore several reconstruction methods have been studied regarding their performance and systematics.
In this chapter, two different track fit methods – the Chi Squared Method and the Global Fit Method – and their systematics are introduced. After this, the resulting point resolution is presented including a comparison between the fit methods. The last section contains a study of edge effects.

## 5.1 Chi Squared Fit Method

### 5.1.1 Principle

The first track fitting method that has been implemented in MultiFit, is the $\chi^2$-method. This fit is based on the *least squares method*, which is often referred to as *chi-squared minimization*[1]. The least squares method states that the parameters $a_j$ for which the sum

$$\chi^2 = \sum_{i=1}^{n} \left[ \frac{x_i - f(y_i; a_j)}{\sigma_i} \right]^2 \tag{5.1}$$

with $x_i$ : measured values, with errors $\sigma_i$ taken at $y_i$ , $i = 1 \dots n$

$a_j$ : parameters of the fit function:
$f(y; a_j)$ , $j = 1 \dots m$ and $m < n$

is a minimum, are the values for which the function $f(y; a_j)$ best describe the measured data. The number of data points $n$ has to be higher than

[1] Strictly speaking, this is only correct if the variables $x_i$ in equation 5.1 are Gaussian distributed with mean $f(y_i; a_i)$ and variance $\sigma_i^2$, so $S$ is a true *chi-square*.

the number of parameters of the fit function $m$. This fit method is implemented in MultiFit for two assumptions on the track shape: a straight line for measurements done without magnetic field and a curved track, for which its projection in the $xy$ plane can be described by a circular arc[2], for measurements done in a magnetic field.

The most simple assumption for a track is a straight line, which leads to the following equations for the least squares method:

$$\begin{aligned} x = &\quad f(y) = a \cdot y + b \\ \Rightarrow \quad \chi^2 = &\quad \sum_{i=1}^{n} \left[ \frac{x_i - a \cdot y_i - b}{\sigma_i} \right]^2 \quad , \end{aligned} \tag{5.2}$$

where $a$ = Intercept $X_0$ and $b$ = Slope X = $\tan(\phi)$ denote the line parameters[3], $x_i$ the measured hit $x$ positions with their errors $\sigma_i$, $y_i$ the vertical center of the row of the hit and $n$ the number of measured hits (see Figure 5.1).

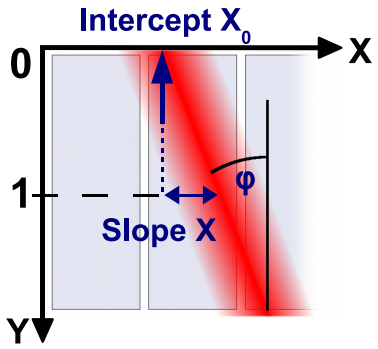


Figure 5.1: Parameters of the straight line fit.

The second possible track assumption is a curved track. For this assumption, two $\chi^2$-methods are implemented in MultiFit. The first method uses a second degree polynomial as an approximation to a circular arc. Due to the choice of the coordinate system (see Figure 5.2), $x$ is fitted in dependency of $y$ and the following fit function results:

$$x = f(y) = a \cdot y^2 + b \cdot y + c\,. \tag{5.3}$$

[2]The three dimensional track describes a helix.

[3]In MultiFit Slope X is defined as the difference between the $x$ coordinate at the point, where the track $y$ coordinate is 1, and the Intercept $X_0$.

In MultiFit, only the fitted parameter $a$ is used to calculate the radius of the circle with $R = a/2$ and the curvature results from $C = 1/R$. The center $(x_0, y_0)$ of the circle is calculated by solving the equation:

$$(x - x_0)^2 + (y - y_0)^2 = R^2 \tag{5.4}$$

for two points $(x_1, y_1)$ and $(x_2, y_2)$ on the circular arc. This fitting method is very fast, but is only an approximation to the shape of a real particle track.

The second method to fit curved tracks is to directly fit a circular arc (see Equation 5.4) to the measured data. This gives a better description of the measured track, since a particle trajectory in a homogeneous magnetic field follows a helix which results in a circular arc in the $xy$ projection. The fit is done in the same rotated coordinate system like the second degree polynomial fit, and uses the results of that fit for initialization, to have reasonable start values for its parameters $C$ and $(x_0, y_0)$. The fit function of this method is given by

$$x = f(y) = x_0 \pm \sqrt{\frac{1}{C^2} - (y - y_0)^2} \quad , \tag{5.5}$$

where the sign before the square root expresses a positive respectively negative curvature. In the fitting procedure the function is fitted with both signs and the fit with the best $\chi^2$ is chosen.

Figure 5.2 shows a sketch of the results of both fitting methods for curved tracks in the rotated coordinate system. To be comparable, the curvature of both graphs is the same. One can see that the second degree polynomial gives an good first approximation to the circular arc, but for the accuracy needed in the analysis it is not sufficient.

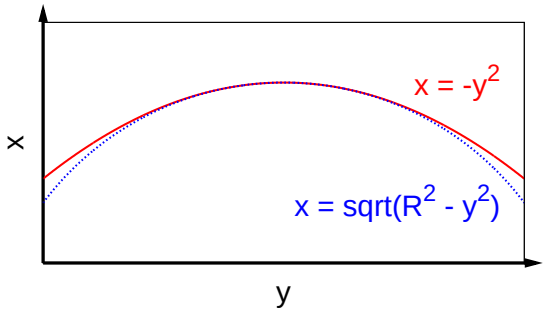


Figure 5.2: Curved chi-squared methods: Rotated coordinate system and sketch of the fit functions: red, solid line: circular arc; blue, dotted line: second degree polynomial.

The fit with the *least squares method* used in the $\chi^2$-method is a simple and well understood fit method. Since the maximum number of free parameters of the implemented fit functions is three and the minimum of active rows to take a measured event into account is set to at least five, the track fit with this method should work on almost all measured events.
A more detailed description of the *least squares method* and the *chi-squared minimization* can be found in [Leo94].

### 5.1.2 Pad Response

Using GEMs for gas amplification creates a much narrower signal than using proportional wires for amplification. In our current setup this leads to the effect that the width of the signal at the pad plane can get as narrow or even narrower than the width of a single pad. This small *charge sharing*[4] can lead to incorrect determination of the reconstructed $x$ position of the hit. If the charge sharing is large enough, the $x$ position of the signal can be determined very accurately by use of the *Center of Gravity*[5] method (CoG) in the ClusterFinder. CoG method means here, that measured signals on the pads multiplied with the $x$ position of the pad are being summed up and the result is divided by the total signal:

$$CoG = \frac{\sum_i^{pads}[signal_i \cdot x_i]}{\sum_i^{pads} signal_i} \,. \tag{5.6}$$

This sum includes all signals that are higher than an adjustable threshold.

#### Effects of Small Signal Widths

If the signal width is narrower than a few pads, the $x$ position of the signal is not reconstructed correctly anymore by this simple method. This problem is illustrated in Figure 5.3: In the top half (5.3.a) the charge cloud of a narrow track signal on the pad plane is shown. In the bottom half (5.3.b), the created signal on the single pads is shown as a histogram together with the Gaussian describing to the charge cloud[6]. The two vertical lines in the histogram show the true $x$ position of the track at the middle of the Gaussian (left, red line) as well as the reconstructed $x$ position (right, green line). As is clearly visible, due the *Center of Gravity* method the position of the signal is reconstructed wrongly towards the middle of the pad with the highest signal, instead of at the true position.

[4] *Charge sharing* is an expression for the condition in which the charge of the hit is spread over several pads; *small* means that only a few and *large* that many pads are hit.
[5] This should not be confused with a method used to combine pulses to a hit that was implemented in older versions of MultiFit and was also called *Center of Gravity* method.
[6] Assuming that the charge distribution of the track shows a Gaussian behavior.

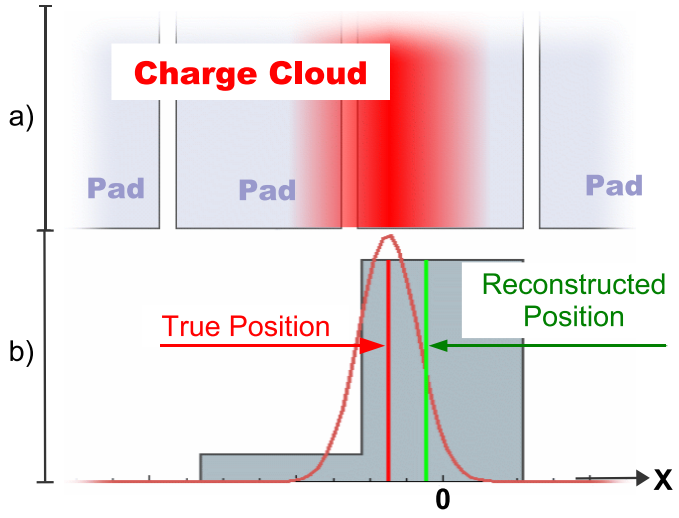


Figure 5.3: Pad response: reconstructed and true position of a narrow signal.

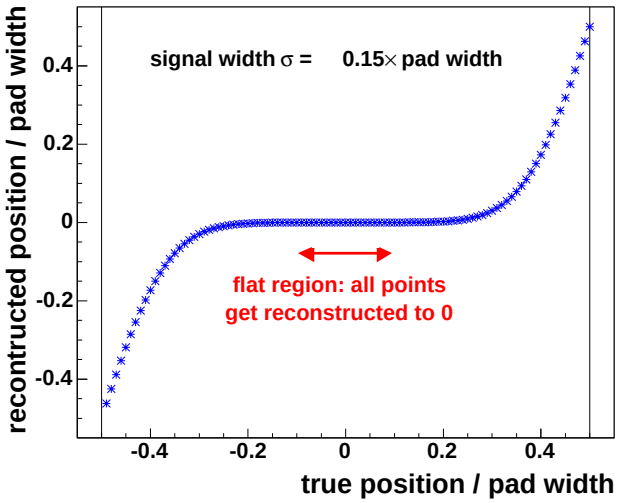


Figure 5.4: Pad response: reconstructed position as a function of the true position (axis normalized to pad width).

In Figure 5.4 this effect is illustrated as a function of the reconstructed hit position in dependency on the true position[7]. The $x$ and $y$ axis are normalized to the pad width. In the case of very narrow signals this function has a flat area around the middle of the pad (red arrow in Figure 5.4). In this range all values get reconstructed to zero, which makes it impossible to determine the true position from the reconstructed one. In this area there is a real loss of information.

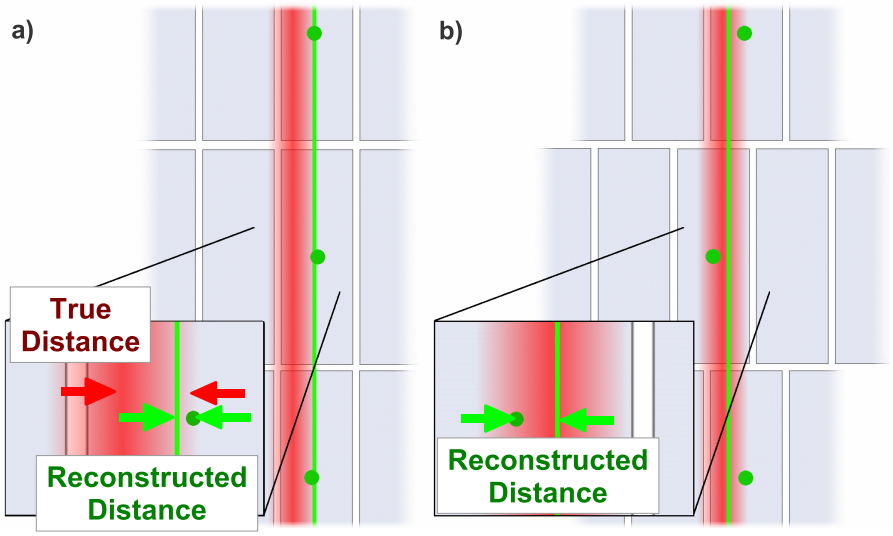


Figure 5.5: Pad response: effect of CoG method on residual calculation for a) non-staggered and b) staggered pad layout.

The error in the hit reconstruction leads to different effects on the determination of the point resolution depending on the pad layout. For the non-staggered pad layout all hits of the track get reconstructed wrongly in the same direction. Therefore the whole reconstructed track "gets drawn" in that direction. In consequence the residuals calculated from these values of the hits and the track are smaller than the real distance between the reconstructed points and the true track (see Figure 5.5.a).

In case of the staggered pad layout the hits get reconstructed wrongly in opposite directions for adjacent pad rows. So the errors of the wrong hit position reconstruction cancel each other out pairwise in the track re-

[7]In this calculation all pads with a signal fraction that is smaller than 1 % of the total signal have not been included. The value of 1 % is chosen according to the noise threshold implemented in MultiFit by M.E. Janssen [Jan06]. This value is supported by the analyses in Section 5.2.3.

construction[8]. In consequence the track is being reconstructed – more or less – at the true position while the hits are reconstructed in some distance from their true position. The resulting residuals are bigger than the distance between the true points and the reconstructed track (see Figure 5.5.b; the resulting resolution will be shown below in Figure 5.8 in section 5.1.4).

### 5.1.3 The Pad Response Correction (PRC)

For a correct reconstruction of the $x$ positions of the hits and resulting from this a correct calculation of the track and the residuals, the *Pad Response Function* (PRF) has to be taken into account. The *Pad Response Function* is the function that describes the measured charge on a pad in dependency on the original signal and the pad geometry (see [LW92]). The PRF is derived from folding the *pad function*, which consists of two $\Theta$-functions in the case of rectangular pads, with the function describing the spatial charge distribution of the signal, which is assumed to be Gaussian distributed[9]:

$$Q_{\mathrm{pad}}(y) = \int_{-\infty}^{\infty} \underbrace{\left(\Theta\left(\psi - \frac{\Delta}{2}\right) \cdot \Theta\left(-\psi + \frac{\Delta}{2}\right)\right)}_{\text{pad}} \cdot \underbrace{\left(\frac{Q_{\max}}{\sqrt{2\pi}\sigma_S} \exp\left[-\frac{(y-\psi)^2}{2\sigma_S^2}\right]\right)}_{\text{signal}} d\psi\,, \quad (5.7)$$

where $\Delta$ denotes the width of the rectangular pad, $Q_{\max}$ the height of the signal, $\psi$ the integration variable in the $y$ dimension and $\sigma_S$ the width of the signal.

In this work, the function which is used to unfold the reconstructed position and determine the true position is called the *Pad Response Correction* (PRC). To derive that function, the PRF is used to simulate the pad signal a Gaussian charge cloud of a certain width would produce for different positions of its center relative to the pads. Signals below a threshold of one percent are not taken into account[10]. From these signals the $x$ position of the hit is determined with the Center Of Gravity method described in section 4.1.1.

[8] This is an approximation, which is only true if an even number of rows is used for the reconstruction and the track is straight and perpendicular to the rows.

[9] Assuming a Gaussian shape for the signal function is a good approximation for most TPCs [LW92].

[10] As before, the 1 % value is an educated guess on the noise in the measured data (see forthcoming PhD thesis of M. E. Janssen and Section 5.2.3).

As mentioned before, the function describing the reconstructed position in dependency on the true position has a flat region for small signal widths. In the following steps these two cases must be distinguished. Therefore two different functions are fitted to the values from the Center Of Gravity method: the function $F_{noflat}$ (5.8a) for the case, when there is no flat area around the middle of the pad, and the function $F_{flat}$ (5.8b) for the case, when there is a flat area.

$$F_{noflat} = P_1 x + P_2 \cdot \sqrt{x} + \left( \frac{1 - P_1}{2} - \frac{P_2}{\sqrt{2}} \right) \cdot \sqrt[3]{2x} \qquad (5.8a)$$

$$F_{flat} = P_0 + P_2 \cdot \sqrt{x} + \left( \frac{1 - 2P_0}{2} - \frac{P_2}{\sqrt{2}} \right) \cdot \sqrt[3]{2x}\,, \qquad (5.8b)$$

where $P_0$, $P_1$ and $P_2$ are fitting parameters and $x$ denotes the $x$ coordinate. Since the functions are symmetric relative to 0, they are only fitted in the positive domain.

In Figure 5.6 simulated values and the belonging fitted function $F_{(no)flat}$ for several signal widths are shown (it should be annotated that in this figure the axis are exchanged in comparison to Figure 5.4).

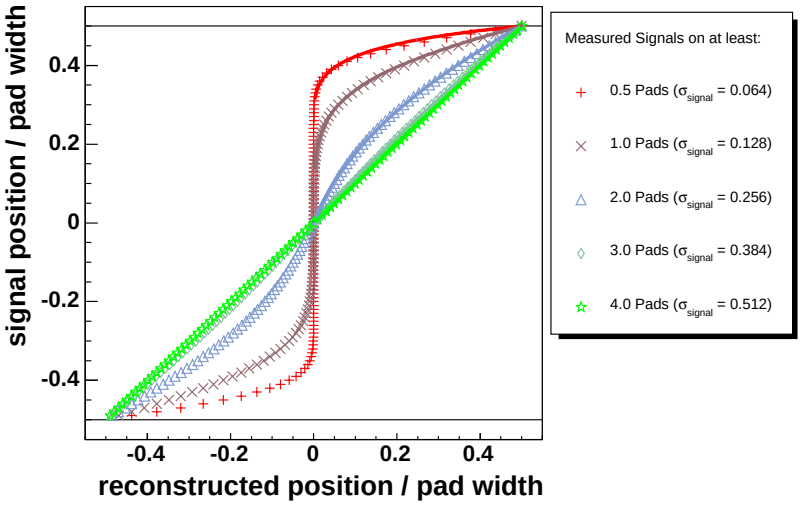


Figure 5.6: Pad response: true $x$ position of a signal as function of the reconstructed position for different signal widths. Simulated values (markers) and fit functions (lines) are shown (axis normalized to pad width).

The values and fit functions are plotted for several widths $\sigma$ of the Gaussian describing the charge distribution of the hit. In the legend the minimum of the number of pads[11] that show a signal for a given $\sigma$ is listed.

There are two important signal widths: The width of 0.128 in units of the pad width[12] corresponds to the situation, where the charge of the hit is spread at least over the full width of one pad for any $x$ position of the signal. This is the limiting case for the occurrence of a flat area; for all larger widths, the functions have no flat range anymore. This is a very important value, since for all values below this limit there is a loss of information in the flat range.
The second important signal width is 0.512 [pad width]. For a signal of this width or more, which corresponds to charge deposition on at least 4 pads, the function becomes a straight line. In this case the unfolding is no longer needed to determine the correct $x$ position of the signal, since the reconstructed position is the same as the true signal position.

The error of the hit position $\sigma_{x,unfolded}$ is calculated applying Gaussian error propagation. This leads to a scaling of the original error values with a linear function which has the slope of the used function $F_{(no)flat}$ at the hit $x$ position $x_{hit}$ and crosses the point $x_{hit}$, $F_{(no)flat}(x_{hit})$:

$$\sigma_{x,unfolded} = a \cdot \sigma_x + b \quad \text{, with } a = \frac{dF_{(no)flat}}{dx}(x_{hit}) \tag{5.9}$$

$$b = \frac{F_{(no)flat}(x_{hit})}{a \cdot x_{hit}} \tag{5.10}$$

The values of the parameters $P_0$ to $P_2$ together with the $\chi^2$ value of the corresponding fit are plotted in Figure 5.7. In the plot for $P_2$ one can clearly see the limiting case of the signal width of 0.128 [pad width]. The $\chi^2$ plot shows a significant increase for $F_{noflat}$ below this limit; above the $\chi^2$ of $F_{flat}$ is slightly bigger than the one of $F_{noflat}$. Since the errors are not considered in the $\chi^2$ plot, only the comparison of both values is valid.

The functions 5.11.a-d, which are dependent on the signal width $\sigma$, are fitted to these parameter values in the domain where the belonging $\chi^2$ is the smallest.

[11] How many pads get hit by a signal of a certain width depends on the $x$ position of the signal relative to the pads.
[12] The width of the signal is the $\sigma$ of the Gaussian distribution describing the signal.

$$P_{0,flat}\ (\sigma) = a_{01} \cdot \big((1-\sigma)/a_{00}\big) \quad (5.11a)$$
$$P_{1,noflat}(\sigma) = a_{15}\sigma^5 + a_{14}\sigma^4 + a_{13}\sigma^3 + a_{12}\sigma^2 + a_{11}\sigma + a_{10} \quad (5.11b)$$
$$P_{2,flat}\ (\sigma) = a_{26}\sigma \quad (5.11c)$$
$$P_{2,noflat}(\sigma) = a_{25}\sigma^5 + a_{24}\sigma^4 + a_{23}\sigma^3 + a_{22}\sigma^2 + a_{21}\sigma + a_{20} \quad (5.11d)$$

where $a_{ij}$ denote fit parameters and $\sigma$ denotes the width of the Gaussian describing the signal normalized to the pad width. $P_{k,(no)flat}$ denote the functions belonging to the parameters $P_k$ and "$flat$" respectively "$noflat$" denote the domains of the parameter functions. The functions $P_{k,(no)flat}$ are drawn as black lines in the graphs of the parameters $P_n$ (Figure 5.7).

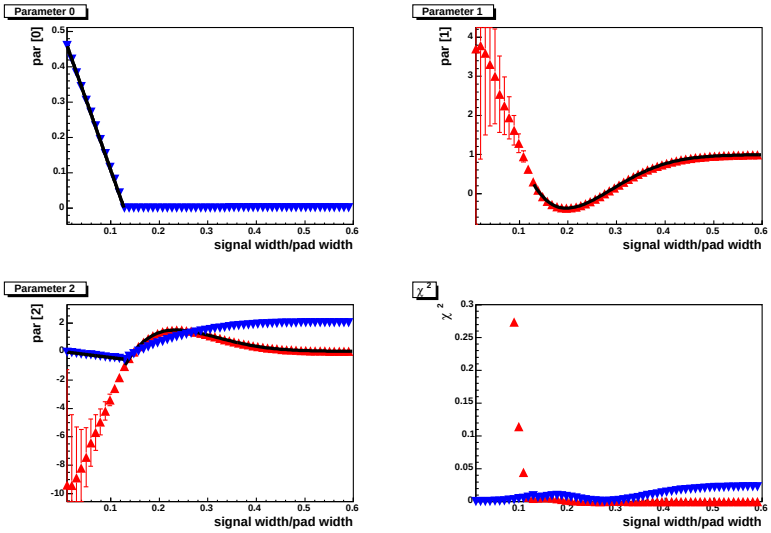


Figure 5.7: Pad response: parameter $P_0$, $P_1$, $P_2$ and $\chi^2$ value of the functions $F_{noflat}$ (red triangles pointing up) and $F_{flat}$ (blue triangles pointing down) derived from fits with different signal widths (X axis normalized to pad width).

The functions $P_{k,(no)flat}$ are implemented in MultiFit with the fitted parameters given in Table 5.1. The width of the Gaussian distribution for a certain hit is calculated from its $z$ position using values for the diffusion and defocussing coefficients that have been computed by a Monte Carlo simulation with MAGBOLTZ [MAGB05, Bia99]. The diffusion and defocussing coefficients for a certain magnetic field are given to MultiFit through the

configuration file. After the computation of the parameters $P_n$, these values are used in the function $F_{noflat}$ respectively $F_{flat}$ to calculate the true signal position from the reconstructed one.

| **Func.** | **Parameters** | | | | | |
|---|---|---|---|---|---|---|
| $P_{0,flat}$ | $a_{01}$ | $a_{00}$ | | | | |
| | 0.49900 | 0.12800 | | | | |
| $P_{1,noflat}$ | $a_{15}$ | $a_{14}$ | $a_{13}$ | $a_{12}$ | $a_{11}$ | $a_{10}$ |
| | −832.538 | 1936.17 | −1739.82 | 739.665 | −141.994 | 9.52257 |
| $P_{2,flat}$ | $a_{26}$ | | | | | |
| | −4.21678 | | | | | |
| $P_{2,noflat}$ | $a_{25}$ | $a_{24}$ | $a_{23}$ | $a_{22}$ | $a_{21}$ | $a_{20}$ |
| | 1398.15 | −3350.91 | 3126.27 | −1399.78 | 292.479 | −21.2726 |

Table 5.1: Parameter values of the functions $P_{k,(no)flat}$ implemented in MultiFit.

### 5.1.4 Results of Unfolding with the PRC

In this section, the effects of the PRC on the point resolution are presented. In Figure 5.8 some typical results for the calculated point resolution in dependency on the drift distance $z$ are shown. In the reconstruction and calculation of these values, the Pad Response Correction was not used in the hit reconstruction. The measurements were done for staggered and non-staggered pad layouts, with a pad pitch of 6.2 mm (Y direction) and 2.2 mm (X direction), in a 2 T magnetic field and with TDR gas in the drift volume.

In the left graph (5.8.a), the result for the non-staggered pad layout is shown. The values of the point resolution as well as their dependency on the drift distance have the expected shape. With smaller drift distances the point resolution gets better.

In contrast, the point resolution values for the staggered layout in the right graph (5.8.b) show a different behavior. While the values for drift distances that are larger than about 400 mm are comparable to the results of the non-staggered layout, which was expected, the graph shows a different dependency on the $z$ coordinate for smaller distances. The point resolution gets worse, from about 200 $\mu$m up to about 440 $\mu$m at $z \approx 15$ mm.

The reasons for this behavior have been pointed out in Section 5.1.2 (see Figure 5.5): With decreasing drift distance the signal width decreases, too (see Section 2.1.4). As shown in Figure 5.6 in the previous section, this causes a stronger effect of the pad response. Therefore the hit reconstruction without using the *PRC* produces increasing deviations of the hit coordinates from the true positions for decreasing drift distances. This results in larger values of the calculated residuals and distances.

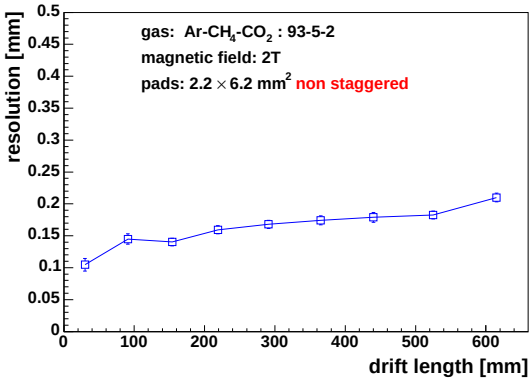


(a) non-staggered pad layout

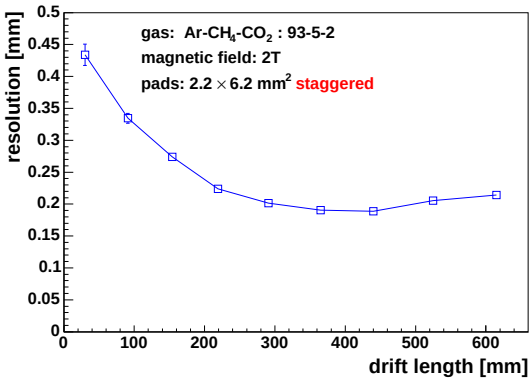


(b) staggered pad layout

Figure 5.8: Point resolution for TDR gas, 2 T magnetic field, track fit with $\chi^2$-method, no PRC used in the hit reconstruction, 6 rows used in the reconstruction and the resolution calculation.

If the *PRC* is used to unfold the results of the hit coordinate, the increase in the point resolution at short drift distances vanishes. This is shown in Figure 5.9, in which the point resolution values for the staggered pad layout are plotted again, this time with and without the correction of the $x$ coordinates with the PRC (the point resolution has been calculated from the same data as in the right graph of Figure 5.8).

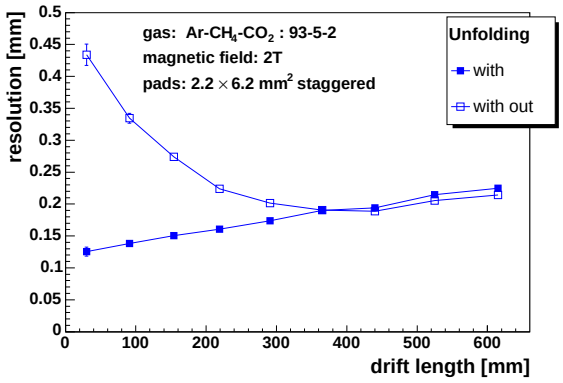


Figure 5.9: Point resolution: comparison of hit reconstruction with and without PRC for TDR gas, 2 T magnetic field, track fit with $\chi^2$-method and 6 rows used in the reconstruction and the resolution calculation.

Point resolution results for different magnetic fields are shown in Figure 5.10 for TDR gas and both pad layouts. As expected, the results for the non-staggered and staggered pad layout get comparable. For drift distances below about 200 mm, the point resolutions calculated from measurements in a magnetic field of 4 T still show an increase with decreasing Z. This might indicate, that in this range – due to the low diffusion in the 4 T field – the signal width is so small compared to the pad width, that there is a flat area in the *PRF*. Therefore the correct hit position can't be reconstructed in a certain range of the true signal position around the middle of the pad.

Figure 5.11 shows results for P5 gas and staggered pad layout (for P5 gas and non-staggered pad layout, no measurement run has been taken). While the diffusion coefficient at 4 T is smaller for P5 gas than for TDR gas (see Figure 2.10 in Section 2.1.4), the defocussing is much stronger due to the increase in the diffusion coefficient in high electric fields (see Figure 2.8 in Section 2.1.4). Therefore the increase towards smaller drift distances is not as significant as in the graphs of the TDR data. But the resolution results of the 4$T$ data still show higher values than the 2 T results for $z$ coordinates below about 120 $\mu$m.

In this context it would be very interesting to test the behavior of the reconstruction with the PRC unfolding for smaller pad sizes. A future examination – based on Monte Carlo simulations – of the effects of different pad sizes as well as different pad shapes and layouts is planned. In addition, measurements with smaller pads are planned for the following months.

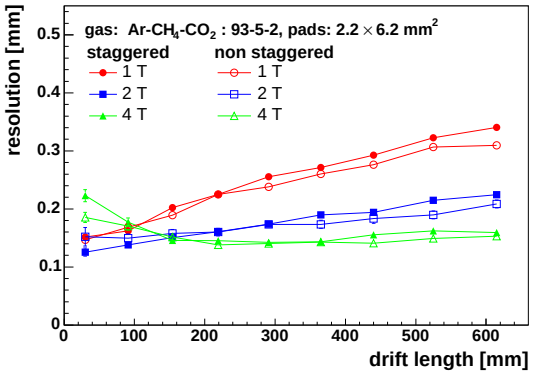


Figure 5.10: Point resolution for TDR gas, 1-4 T magnetic field, track fit with $\chi^2$-method and 6 rows, PRC used to unfold the hit coordinates. Filled markers: non-staggered pad layout; hollow markers: staggered pad layout.

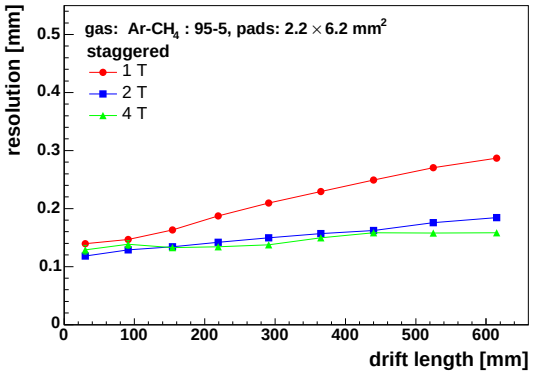


Figure 5.11: Point resolution for P5 gas, 1-4 T magnetic field, staggered pad layout, track fit with $\chi^2$-method and 6 rows, PRC used to unfold the hit coordinates.

### 5.1.5 Study of the Effects of the PRC by Use of a Monte Carlo Simulation

A study based on Monte Carlo simulations (see Section 3.3) shows very clearly the positive effects of the unfolding using the PRC in the reconstruction process. Two simulations have been run for a staggered pad layout (pitch: 2.2 mm x 6.2 mm) with nineteen rows and twenty-four columns and P5 gas with 0 ppm water contamination in the drift volume. The magnetic field strength has been set to 2 and 4 T. In the following analysis only eight of the nineteen rows have been used for the reconstruction process to make the results comparable to the measured data. For the track fit the Chi Squared Method implementation for a straight track hypothesis has been used, since the Monte Carlo simulation produces only straight tracks.

#### Intercept X

In Figure 5.12.a the Intercept $X_0$ of tracks fitted with the $\chi^2$-method with and without the unfolding as well as the Monte Carlo truth are shown. On the left side (Figure 5.12.a) one can see that the Intercept $X_0$ reconstructed with the unfolding shows a good agreement with the Monte Carlo distribution. The deviation of the calculated Intercept $X_0$ from the Monte Carlo truth is plotted in Figure 5.12.b. Here a significant improvement by the use of the unfolding is seen.

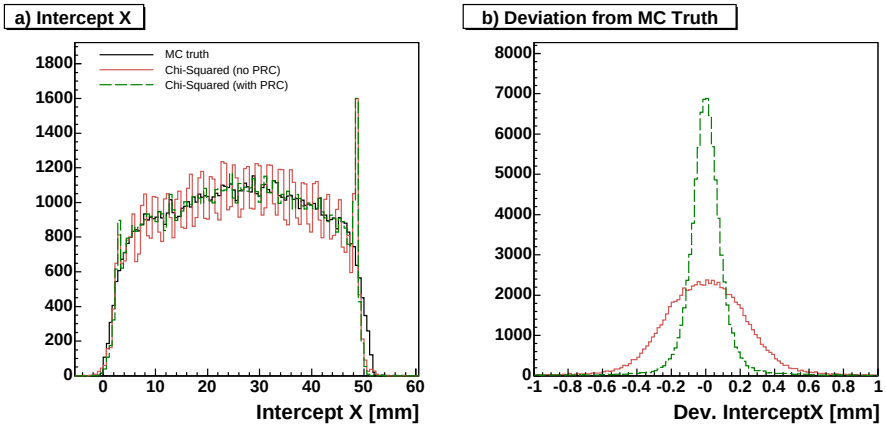


Figure 5.12: Intercept $X_0$ for fit with (green, dashed) and without (red, solid) PRC unfolding: a) comparison of both fits with the Monte Carlo truth (black) b) deviation of reconstructed values from the Monte Carlo truth.

In Figure 5.12.a, there is a pattern of 25 peaks and 24 dips in the histogram of the Intercept $X_0$ reconstructed without the unfolding. This pattern is an effect of the incorrect hit positions reconstructed without the PRC unfolding and will be explained in the next few paragraphs. The large peaks at both sides of the sensitive area (2.2 mm and 50.6 mm) are edge effects (see Section 5.4).

In Figure 5.13 the mean deviation of the reconstructed hits from the Monte Carlo track is plotted exemplarily for the first three rows[13] in dependency on the Monte Carlo Intercept $X_0$ and the Monte Carlo Slope X (converted to an angular scale). The Intercept values are plotted modulo the pad pitch (=2.2), so that the values with the same position relative to a pad in the first row are summed up. In the plot in the top left corner it is clearly visible, that – with a slight dependency on the angle of the track – the hits on the left side of a pad tend to get reconstructed towards bigger $x$ values and vice versa on the right pad side. This means that the hits tend to get reconstructed towards the middle of a pad.

This effect is also visible for the following rows. But there the angular dependency gets larger with each row, because tracks with different angles result in different positions relative to the pads depending on the $y$ coordinate of the pad row. If the track has an angle of zero, the deviation is the same for all even respectively all odd rows. This can be seen in Figure 5.13: the hit deviations at zero angle are the same for row one and three, while it is inverse in row two. In row two the gap between two pads lies in the middle of the histogram because of the staggered pad layout.

The reconstruction with the unfolding of the hit positions shows an improvement (right side of Figure 5.13): the deviation pattern is limited to a narrower range and the deviation values are much smaller. The little "dark dots" in Figure 5.13 result from some very few events with a deviation larger than $\gg$0.6 mm, where *delta electrons*[14] or other effects play a role. These events show no systematics but are coincidental and make up less than 2% of all events.

The dependency on the Intercept $X_0$ of the mean hit deviations per row do not cancel out when averaged over all rows, but still give a mean hit deviation which is non-zero. This is shown in Figure 5.14, where the mean hit deviation from the MC track is plotted against the Intercept $X_0$ modulo the pad width.

[13] The values look similar for the other rows.

[14] Electrons produced by primary ionization which have a high momentum and can travel a significant distance from their origin producing a measurable signal on this way.

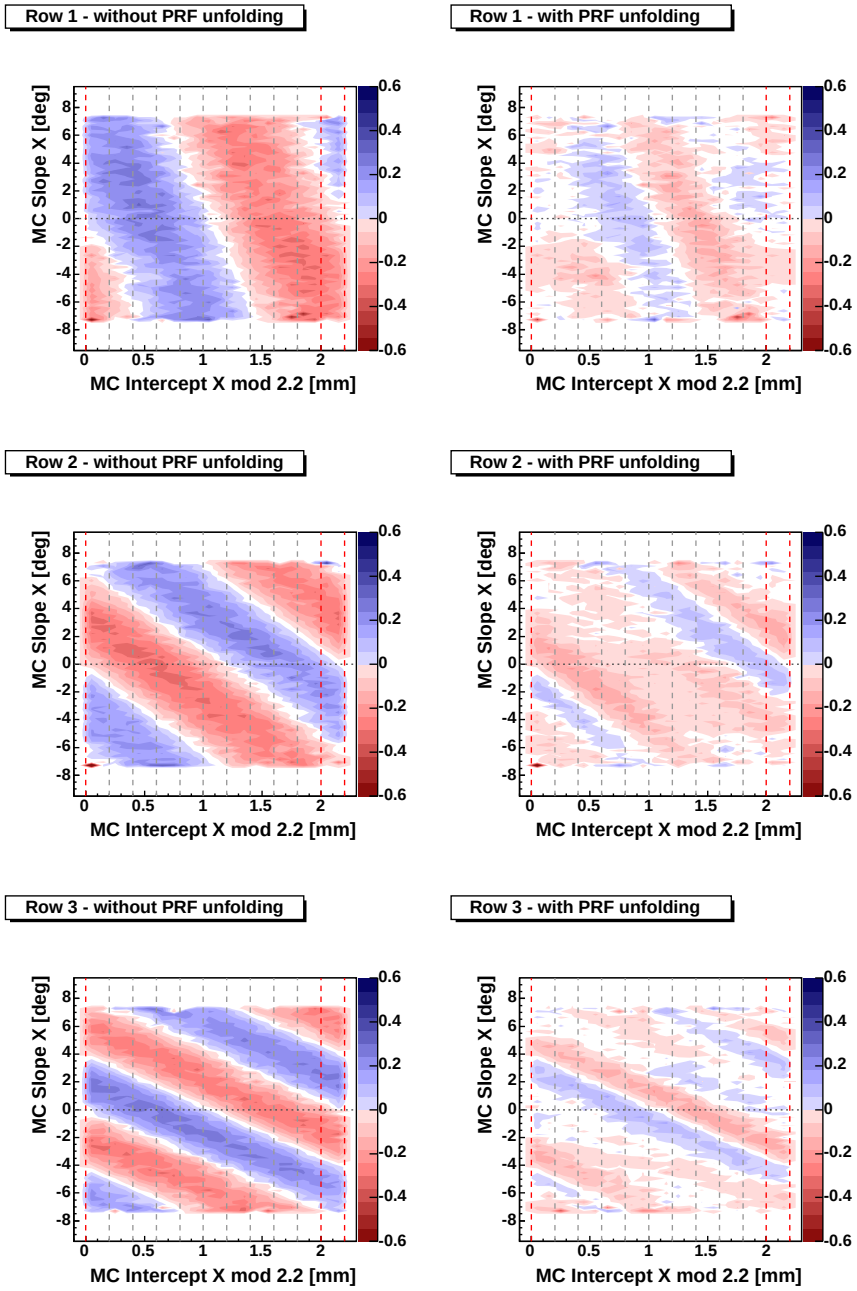


Figure 5.13: Mean hit deviation [mm] from Monte Carlo truth with and without PRC unfolding depending on MC Intercept $X_0$ and Slope X for the first three rows.

The reconstruction of hit positions from narrow signals towards the centers of the pads in the first row (respectively the center of pads in all uneven rows) shown in Figure 5.14 causes an accumulation of Intercept $X_0$ values in this area. This accumulation is naturally combined with a lack of values in the adjoining regions at the pad edges. The resulting uneven distribution of Intercept $X_0$ values causes the pattern shown in Figure 5.12.

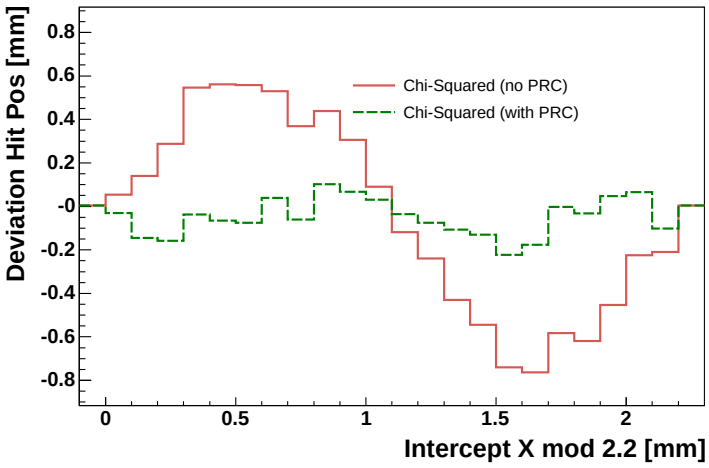


Figure 5.14: Mean hit deviation [mm] from Monte Carlo truth with (green, dashed) and without (red, solid) PRC unfolding depending on MC Intercept $X_0$.

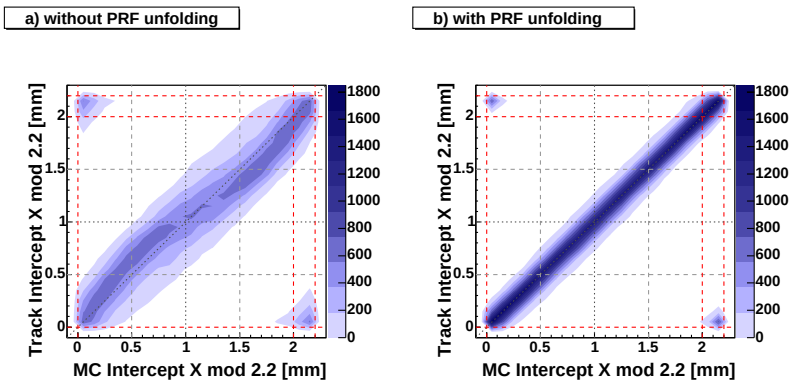


Figure 5.15: Reconstructed Intercept $X_0$ plotted against Monte Carlo truth: a) with and b) without PRF unfolding.

The deviation of the reconstructed Intercept $X_0$ values from the Monte Carlo truth is plotted in a two-dimensional histogram in Figure 5.15 (the Intercept $X_0$ values are plotted modulo the pad pitch). The chosen representation also illustrates the direction of the deviation. Figure 5.15.a shows that the Intercept $X_0$ tends to be reconstructed to bigger $x$ values on the left side of the pad and to smaller $x$ values on the right side, which results in the observed accumulation near the pad center. With the unfolding of the hit $x$ positions, the Intercept $X_0$ values are reconstructed without such a systematic (see 5.15.b). The values in the top left and bottom right corners of both histograms are overlaps from the neighboring pads.

### Slope X

The use of the Pad Response Correction for the unfolding of the hit $x$ positions also has a positive effect on the calculated angles of the reconstructed tracks. In Figure 5.16.a the distribution of the Slope X values (converted to angle values) of the Monte Carlo truth and the reconstructed values with and without unfolding are plotted.

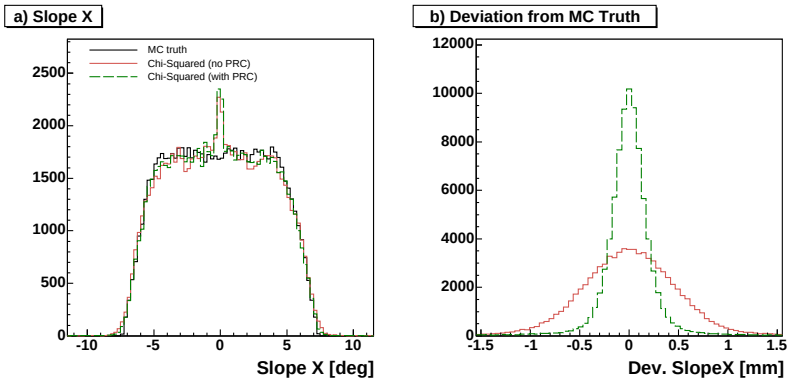


Figure 5.16: SlopeX for fit with (green, dashed) and without (red, solid) PRC unfolding: a) comparison of both fits with the Monte Carlo truth (black, solid); b) deviation of reconstructed values from the Monte Carlo truth.

In this representation, the values of both hit reconstruction methods are in good agreement with the Monte Carlo truth, while the values reconstructed with the unfolding match the Monte Carlo truth a little better. At angle values of about -0.5° to -1.0° a little bump can be observed, which derives from an geometry effect at the edges of the sensitive volume, where

the angles are mostly reconstructed to values in this range (see Section 5.4). In the histogram on the right side (5.16.b), where the deviation of the reconstructed Slope X values from the Monte Carlo Truth is shown, one can see that the distribution of the Slope X values reconstructed without the unfolding is significantly broader than with the unfolding.

This effect is also shown in Figure 5.17, where the distribution of reconstructed values is plotted in the dependency on the deviation of the Slope X and the Intercept $X_0$ modulo the pad pitch.

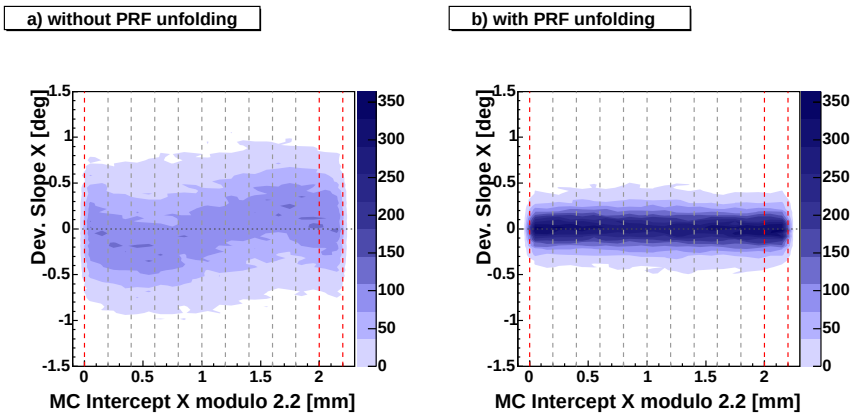


Figure 5.17: Reconstructed Slope X plotted against Monte Carlo Truth: a) with and b) without PRC unfolding.

It is clearly visible that for the reconstruction without the unfolding the reconstructed Slope X is – like the reconstructed Intercept – dependent on the Intercept $X_0$ position of the Monte Carlo truth. For a Monte Carlo Intercept $X_0$ that is between than the center and the left edge of a pad in the first row, the reconstructed angles tend to be smaller than the Monte Carlo angles and vice versa if the Intercept $X_0$ is between the pad center and its right edge. For Intercept $X_0$ values that lie on the middle of a pad or between two pads, there is no angle deviation in a special direction, but the distribution of the deviations is in general much broader than for the values derived from the reconstruction with the PRC unfolding (5.17.b).

### Hit position

A histogram of the absolute deviation of the reconstructed $x$ position of the hits from the position of the Monte Carlo track at the corresponding $y$ coordinate is plotted in Figure 5.18. The data used for this plot has been simulated for a 4 T magnetic field, since in this case the diffusion is very small and the PRC shows a strong effect.

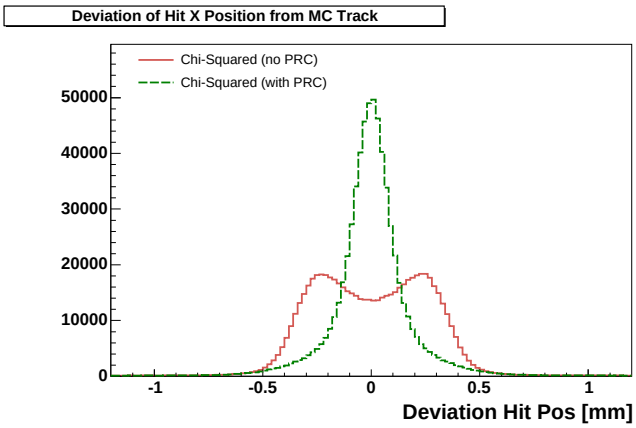


Figure 5.18: Distance of the $x$ coordinates from the Monte Carlo track of hits reconstructed with (green, dashed) and without (red, solid) PRC unfolding (magnetic field: 4 T).

The distribution shows the behavior expected from the previous results: The deviations of the hits reconstructed without PRC unfolding from the Monte Carlo truth show two maxima for hits getting reconstructed wrongly in opposite directions depending on the position of the Monte Carlo track to the pad. The hits which have been reconstructed using the unfolding show one peak which is centered at the position of the Monte Carlo track.

In Figure 5.19 two histograms of the absolute deviation of the reconstructed hit positions from the Monte Carlo truth are plotted for two different ranges of the drift length. One range is close to the readout plane (5.19.a) and the other lies on the opposite side of the drift volume (5.19.b). For this analysis, data from a Monte Carlo simulation run with a magnetic field of 2 T has been used. At this magnetic field the difference is clearly visible, because at small drift distances there is very small charge sharing, while at large drift distances the charge sharing is so large that the unfolding is not needed for almost all hits.

As shown in Figure 5.9, the first range corresponds to the situation, where there is a significant difference between the resulting resolutions for

reconstruction with and without the unfolding. Here it becomes visible again that the deviations from the Monte Carlo track of the reconstruction without unfolding differ significantly from the unfolded results and show a two maxima structure. As expected, in the domain of the second range the distributions are very similar. Here the deviations of the hit $x$ positions from the Monte Carlo track are nearly the same for both reconstruction methods.

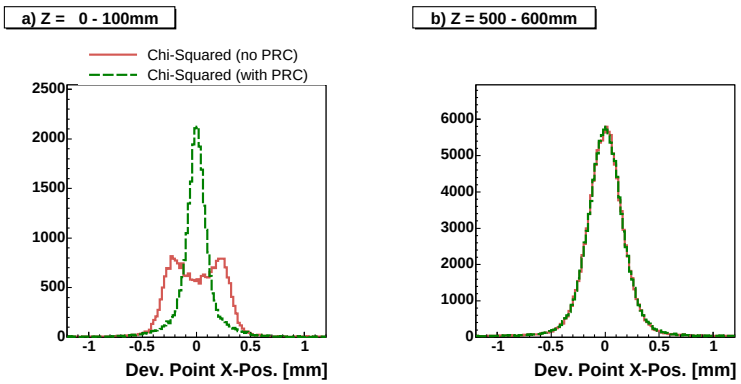


Figure 5.19: Distance of the $x$ coordinates from the Monte Carlo track of hits reconstructed with (green, dashed) and without (red, solid) PRC unfolding (magnetic field: 2 T); Drift length: a) 0-100 mm; b) 500-600 mm.

### Conclusion

From the results shown above follows that the use of the Pad Response Correction in the hit reconstruction improves the calculation of the hit $x$ position significantly. It leads to more accurate reconstructed hit coordinates and therefore to a better track fitting. From both these improvements follow more reliable results from the point resolution calculation.
The current implementation of the PRC does not include a dependency on the track angle and is only accurate for tracks that are parallel to the $y$ axis. For a correct handling of tracks that have a non-zero angle to the $y$ axis, the simulated Gaussian describing the charge distribution of the signal would have to be rotated in the $xy$ plane to be perpendicular to the track. This would lead to deviant signal magnitudes on the pads and therefore the parametrization of the functions $F_{(no)flat}$ respectively $P_{k,(no)flat}$ would have to be modified. In the Global Fit Method (see next section) this dependency is included is planned to implement this dependency in a near future upgrade of the MultiFit ClusterFinder.

## 5.2 Global Fit Method

As mentioned in section 4.1.3, there are currently two track fitting methods implemented in MultiFit: the $\chi^2$-method (see Section 5.1) and the *Global Fit Method* (GFM) [KPR05]. The idea for the second method has been developed by Dean Karlen and his research group [Kar05, LC T05] at the High Energy Physics (HEP) department of the University of Victoria, Canada [Vict05]. It was implemented first in a Java based simulation, fitting and analysis program – called *JTPC* – from the same working group. For a better understanding of the underlying algorithms, their systematics and reconstruction effects as well as for comparisons with the $\chi^2$-method, the GFM has been implemented as an additional fitting method in MultiFit.

### 5.2.1 Principle

The Global Fit Method is based on the maximization of a likelihood function describing the charge distribution of the track[15].
The parameters in this fit are the Intercept $X_0$ and the angle $\phi$ of the track, as well as the width of the Gaussian describing the charge distribution along the trajectory $\sigma$. In both implementations, $\sigma$ can be a free parameter or be set to a fixed value, that is calculated depending on the $z$ coordinate using given diffusion and defocussing coefficients. These three parameters are shown in Figure 5.20. The curvature $C$ of the track can be set as an additional fit parameter for data, that was taken in a magnetic field, or be fixed to zero for straight tracks (the center $X_C$,$Y_C$ of the circle belonging to this curvature and track position is determined by $C$, $\phi$ and $X_0$).

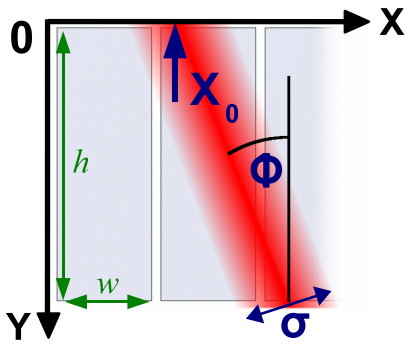


Figure 5.20: Sketch of parameters of the likelihood function.

[15] Although the MultiFit implementation of the Global Fit Method works on the data from the Cluster- and TrackFinder, the input for the fit algorithm are not the hit positions but the charge information from the single pads.

In the model used by the Global Fit Method, the charge density function describing the distribution of the primary ionization along the track is assumed to be uniform in each row. Ionization fluctuations in this range are disregarded. The distribution due to diffusion is described by a two-dimensional, isotropic, Gaussian probability density function. The width $\sigma$ of the Gaussian is assumed to be constant over the length of the track, if it is a free fitting parameter. In the case of the fixed $\sigma$, it is assumed to be constant per row.

The convolution of these two functions leads to the charge distribution on the pad plane (see Figure 5.21). Furthermore, it is assumed that the curvature $C$ of the track is much bigger than the height of the pads, so that the track can be approximated by a straight line in each row (see Figure 5.22).

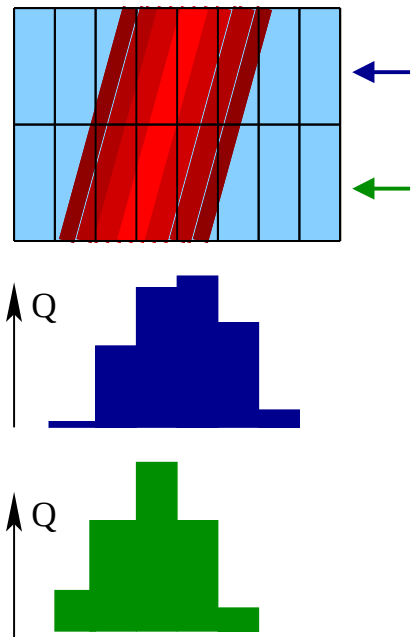


Figure 5.21: Histogram of expected charge on pad plane from Gaussian distributed charge cloud.

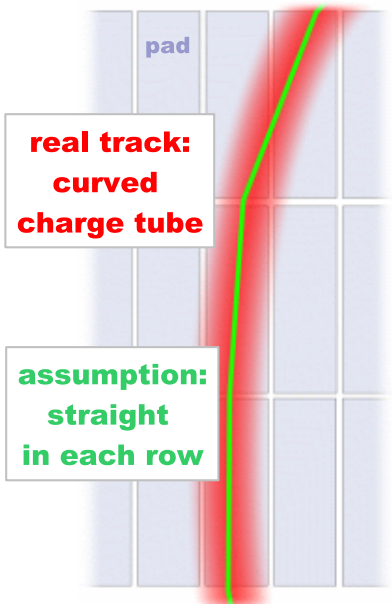


Figure 5.22: Sketch of a curved track (red charge cloud) approximated by a straight line (green line) in each row.

The charge deposition on one pad $Q_{\text{pad}}$ is calculated by integrating the distribution function over the physical area of the pad and is proportional to:

$$Q_{\text{exp}} = \int_{-h/2}^{h/2} dy \int_{-w/2}^{w/2} dx \; \frac{1}{2\pi\sigma} \times \exp\left(\frac{[(x - X_d)\cos\phi_{row} + y\sin\phi_{row}]^2}{2\sigma^2}\right), \quad (5.12)$$

where $h$ is the height and $w$ the width of the pad, the integration variables $x$, $y$ follow the axis of the coordinate system, $X_d$ is the horizontal distance between the pad center and the track position in that row and $\phi_{row}$ is the azimuthal angle of the straight line assumption in that row (see Figure 5.20). $\phi_{row}$ can be calculated from the $\phi_0$, which is the track angle at the point, where the track crosses the $x$ axis ($y = 0$, $x = X_0$), by applying the following equation:

$$\sin\phi = \sin\phi_0 \; - \; \frac{y_{row}}{r}, \qquad \text{with } r = \frac{1}{C} \; , \quad (5.13)$$

where $y_{row}$ is the $y$ coordinate in the vertical center of the row.

The fit function is the product over all pads of the likelihood functions of the charge deposition on each pad $\mathcal{L} = p_i^{n_i}$. $p_i = Q_{\text{exp}}/(\sum_{pads} Q_{\text{exp}})$ is the probability of the association of a primary ionization electron to the pad and $n_i = N_i/G$ is the number of primary electrons associated to the pad ($N_i$ = number of measured electrons on the pad; $G$ = gain value of GEM amplification). This leads to the following binned log likelihood function used in the track fit:

$$\log\mathcal{L} = \sum_{m=1}^{rows} \sum_{n=1}^{pads/row} Q_{\text{measured}}^{n,m} \cdot \log\left[\frac{Q_{\text{exp}}^{n,m}}{\sum_{n=1}^{pads/row} Q_{\text{exp}}^{n,m}}\right]. \quad (5.14)$$

The log likelihood $\ln\mathcal{L}$ is then maximized over all possible values of the parameters. This method does not work row-wise like the $\chi^2$-method, but takes all rows into account at once and includes angular effects. Due to the design of the fit function, the pad response is intrinsically taken into account and the unfolding of the hit positions using the PRC algorithm is not necessary. A more detailed description of the derivation of the fit function can be found in [KPR05].
In the MultiFit implementation of the Global Fit Method, the $x$ positions of the hits are being recalculated during the track fit and saved for the following calculation of the hit distances and residuals needed for the resolution analysis.

As mentioned before, MultiFit gives the possibility to set a fixed $\sigma$ which is calculated from the diffusion and defocussing coefficients in the configuration file. The values of the coefficients for the gas mixture can be computed by use of a MAGBOLTZ simulation. With a fixed $\sigma$ one parameter of the fit function is fixed and it gets more stable in situations where not many measurement points are available. Also, missing charge information at the edge of the pad plane has less impact, since with a fixed $\sigma$ the reconstruction of the hit $x$ position works basically by horizontally shifting a given Gaussian distribution. This is less sensitive than the free $\sigma$ fit and also the Center of Gravity method used in the Chi Squared fit. In these methods, the missing information has more influence because the reconstruction algorithms depend strongly on the width of the charge deposition.

### 5.2.2 Noise Value

Different from MultiFit, the JTPC reconstruction software does not have a built-in clustering algorithm that combines pulses to hits and filters out noise pulses. This leads to the problem that the measured charge values of an event still contain noise pulses during the fitting procedure (see Figure 5.23). These noise signals can have a negative effect on the likelihood calculation: Without a correction, the probability of measuring electrons on pads far from the track, that results from the log likelihood $\ln \mathcal{L}$, is very small. Therefore noise pulses that occur on these pads give a value that does not coincide with the log likelihood at that coordinate.

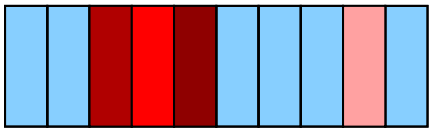

Figure 5.23: Sketch of pad signals from a hit (three red pads) and a noise pulse (one pink pad).

To make the likelihood fit more robust to spurious noise signals, the probability of measuring electrons on pads far from the track gets assigned a larger value in the fit function. Therefore, the formula for the probability $p_i = Q_{\mathrm{exp}}/(\sum_{pads} Q_{\mathrm{exp}})$ is modified by adding a constant offset. This *noise value* is denoted by $N$. The noise value is added to the probabilities $p_i$ of the single pads, which therefore have to be re-normalized through division by $[1 + N \cdot n_{row}]$, where $n_{row}$ denotes the number of pads per row:

$$p_i \rightarrow \frac{p_i + N}{1 + N \cdot n_{row}} \tag{5.15}$$

This leads to a modified formula for the log likelihood fit:

$$\log \mathcal{L} = \sum_{m=1}^{rows} \sum_{n=1}^{n_{row}} Q^{n,m}_{\text{measured}} \times \log \left[ \left( \frac{Q^{n,m}_{\text{exp}}}{\sum_{n=1}^{n_{row}} Q^{n,m}_{\text{exp}}} + N \right) \Big/ \left( 1 + \sum_{n=1}^{n_{row}} N \right) \right]. \quad (5.16)$$

On the left side in Figure 5.24 the Gaussian describing the probabilities $p_i$ with and without the correction with the noise value is shown for a row with ten pads. On the right side the corresponding histograms for the pad signals are shown (in this example the width of the Gaussian distribution is set to three quarters of the pad width). Without the noise value correction in Equation 5.16 the probability of measuring a signal would be nearly zero on the outer pads. With the noise value correction, these pads get assigned a higher – but still small – signal probability.

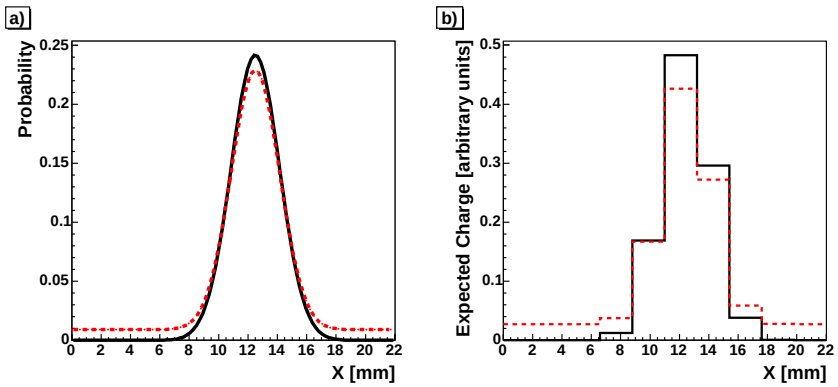


Figure 5.24: a) Gaussian and b) histogram of expected charge distribution $p_i$ without (black, solid line) and with a noise value of 0.01 (red, dashed line).

### 5.2.3 Systematic Studies of the Noise Value

In the original implementation in JTPC, the noise value is set to 0.01 [KPR05]. In the MultiFit implementation, the noise value should not be necessary, since a filtering of the noise hits is already done in the ClusterFinder by the hit reconstruction and only hits that belong to a track are taken into account during the fit due to the TrackFinder routine.
To analyze the effect of the noise value, a series of track fits with the five different values 0.0, 0.0001, 0.001, 0.01 and 0.05 has been run for a measurement run in P5 gas. The series has been run twice, once with $\sigma$ as a free

fit parameter and once with a fixed sigma that has been calculated from simulated diffusion coefficients. The fit with the fixed $\sigma$ can be taken as reference, because the main impact of the noise value is on the width of the track.

### Distance and Residuals

Because the noise value should affect the hit position reconstruction, the distances and the residuals have been analyzed. In both analyses the calculated values have been plotted separately for hits that consist of a different number of pulses.
The results of the hit distance analysis for a 4 T magnetic field are shown in Figure 5.25 for the fit with a fixed $\sigma$ and in Figure 5.26 for the fit with the free $\sigma$. In these figures the mean hit distance is plotted against the position of the reconstructed track relative to the pad the track crosses in the row of the hit. Depending on the number of pulses the hit consists of, different effects are expected:

- In the case of only one pulse, no correction of the pad response is possible. In this case MultiFit reconstructs all hits to a position in the center of the pad. The expected pattern is that in the middle of the pad there is a zero distance value and to both sides of the pad the distance of the hit to the track increases up to a value of half of the pad pitch. This pattern can be seen in both cases for all noise values (the non-zero value of the central bin is a result of the bin width).

- If the hit consists of four or more pulses, the Pad Response Function should not be needed: There is enough charge sharing and the reconstruction should be independent of the position of the track relative to the pads. In the case of the fit with a fixed $\sigma$ this is most of all given for noise values of 0.0 and 0.0001. For bigger values, the distribution deviates more and more from the expected pattern for tracks around the pad center. In the case of the fit with the free $\sigma$, this is especially distinct for the value of 0.05. For the noise values below 0.01, the dependency on the pad position is a little less and the overall distribution is nearer to the highest value of the $\sigma$ free case.

- In the cases of two or three pulses per hit, one expects – if at all – only a small dependency on the pad position. Here the intrinsic Pad Response Correction of the Global Fit should work properly, but in the plots a dependency on the track position is visible. The values of the fit with $\sigma$ free are overall a little bit smaller, which can be explained with the additional free parameter leading to a larger flexibility in the fit. Smaller noise values are closer to the expected pattern and therefore seem to give the most reliable results.

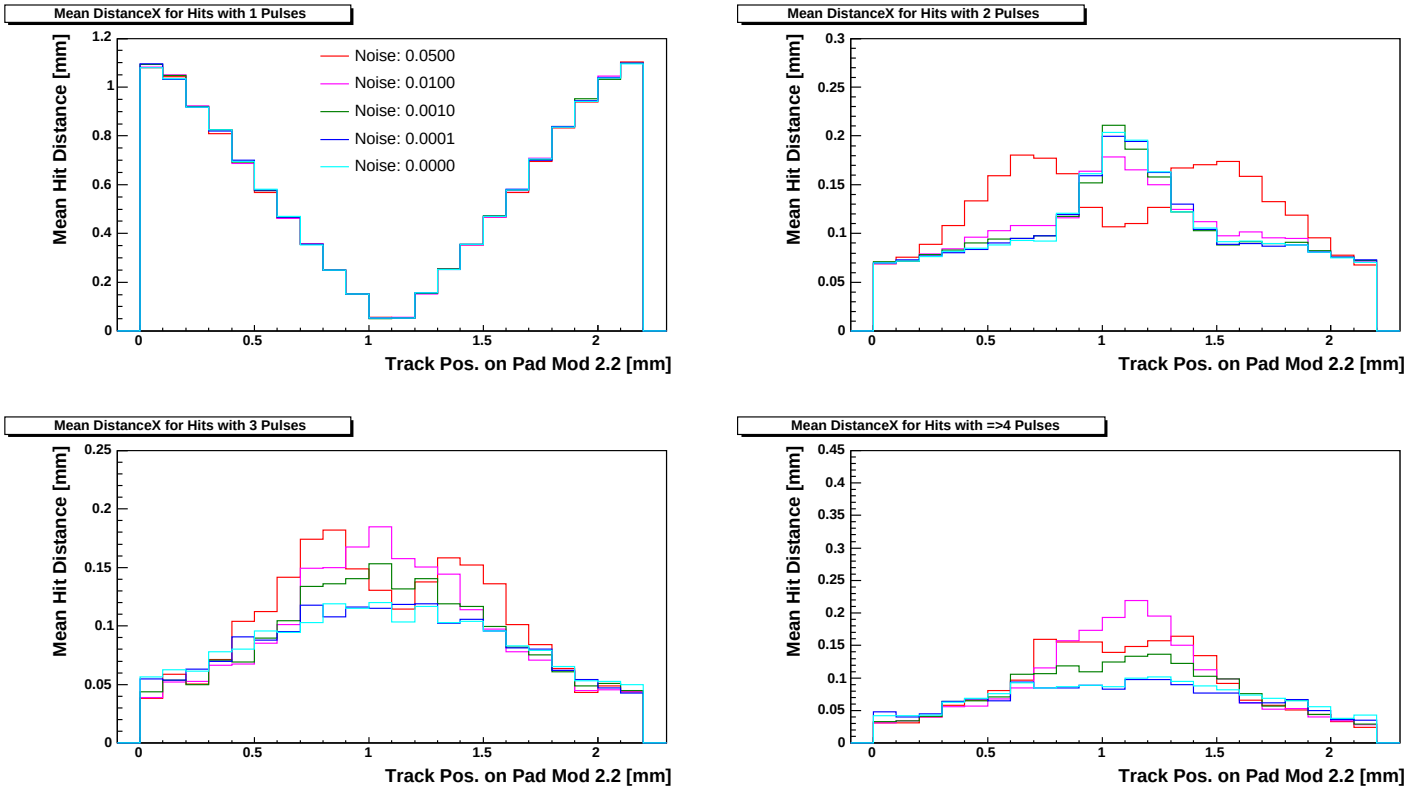


Figure 5.25: Mean hit distance in dependency on the track position relative to a pad for different noise values ($\sigma$ fixed).

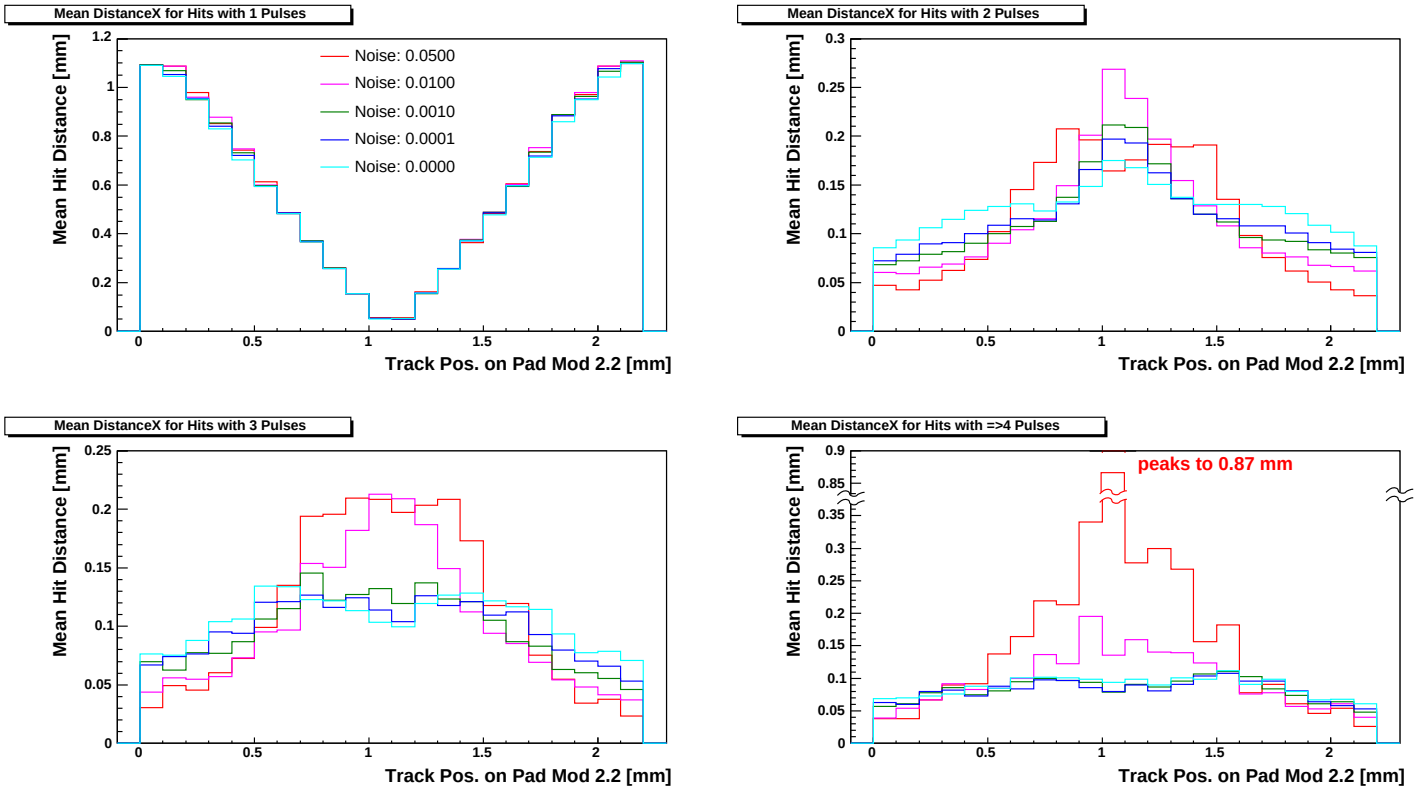


Figure 5.26: Mean hit distance in dependency on the track position relative to a pad for different noise values ($\sigma$ free).

In the residual results, similar patterns are observed, but here the dependency on the noise value is smaller and – as expected from the definition in Section 4.2.3 – the residuals are overall larger than the distances (the plots are contained in the Appendix A: Figure A.1 and A.2).

### Point Resolution

In the next step the point resolution resulting from these distance and residual values has been examined. This is shown in Figure 5.27 and 5.28. Figure 5.27 shows clearly that the resolution seems to be nearly independent from the noise factor in the case of the fit with a fixed $\sigma$. Only the fit with the largest noise factor differs significantly from the others. This can be explained with the effect, that in the case of a narrow charge deposition the outer pads show only a small signal. With a large noise value these pads have no impact on the fit of the hit position, since the signal height is below the noise level (see Figure 5.24).

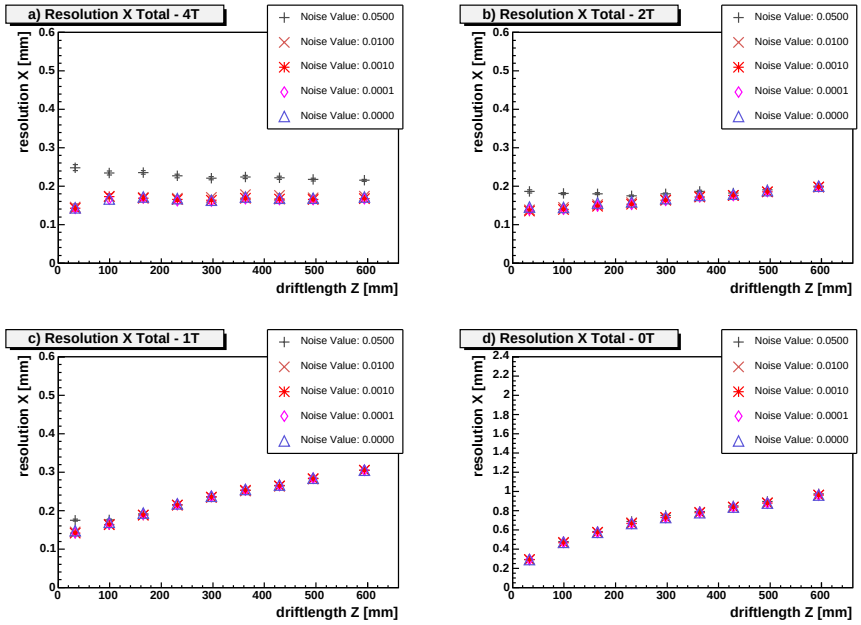


Figure 5.27: Global Fit: point resolution for different noise values ($\sigma$ fixed).

For the fit with a free $\sigma$, which is shown in Figure 5.28, a significant dependency of the point resolution on the noise value is seen: The smaller the noise value the more sensitive the point resolution gets on the signal width. Due to the dependency of the width on the magnetic field and the

drift length, this is seen at high magnetic fields and short distances. Here, the resolution values for the noise value of 0.01 show a good agreement with the values of the fit with a fixed $\sigma$.

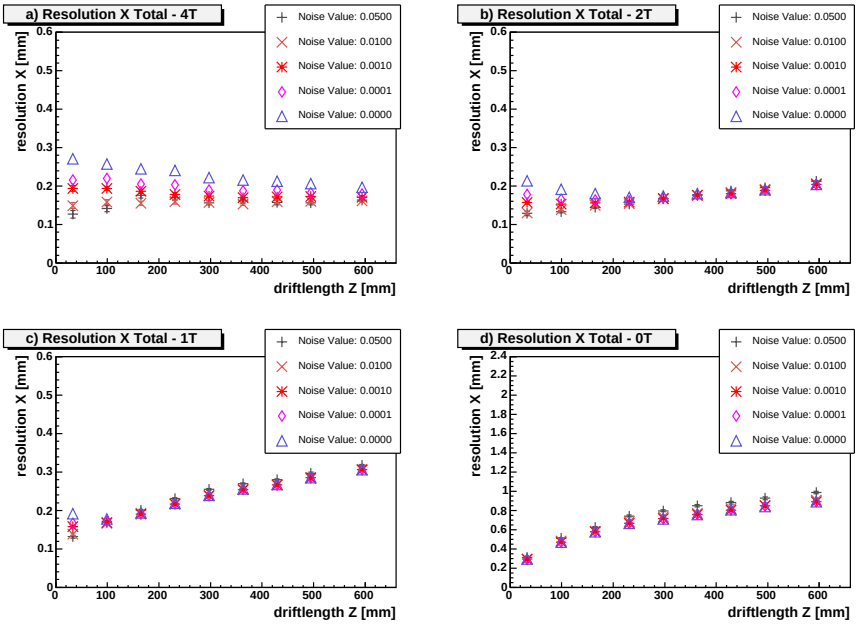


Figure 5.28: Global Fit: point resolution for different noise values ($\sigma$ free).

### Efficiency

In a third step the efficiencies of the fits have been compared. Since there is not external reference, the results can be evaluated only relatively. The percentages of fitted tracks relative to the biggest number are given in Table 5.2.

| **Noise Factor** | $\sigma$ **fixed** | $\sigma$ **free** |
|---|---|---|
| 0.0500 | 80.9 | 43.6 |
| 0.0100 | 81.3 | 68.1 |
| 0.0010 | 82.5 | 84.0 |
| 0.0001 | 83.2 | 91.7 |
| 0.0000 | 82.3 | 100.0 |

Table 5.2: Global Fit: percentage of fitted tracks relative to the biggest number (18496) as a function of the noise factor

Once again, the fit with the fixed $\sigma$ shows only a moderate dependency on the noise value, while it is very strong for the fit with the free $\sigma$. Here the noise value of 0.001 seems to match best in comparison with the results of the fit with the fixed $\sigma$.

Since the Global Method with the free $\sigma$ is more sensitive to missing charge information (at the edge of the pad plane or near damaged pads), the fit is in this case more likely to fail than the fit with the fixed $\sigma$. Therefore a lower efficiency is realistic and a perfect match is not expected.

**Conclusion**

Taking all shown results into account, a noise value of 0.01 seems to be a good choice. Here the results of the residuals and the distances are quite balanced and show a reasonable behavior. The resulting point resolution seems realistic in the $\sigma$ free case and matches well with the resolution values of the fit with a fixed $\sigma$.
The efficiency is still acceptable, judging from the comparison between the efficiency values of the $\sigma$ fixed and free fit and taking the sensitivity of the fit with the free $\sigma$ into account.
That the noise value of 0.0 is not the best value – as was naively expected – can be explained with a little noise still present in the data after the pedestal subtraction and the hit reconstruction.
Choosing this noise value has the further advantage that the fit and analysis results are comparable to the results of the TPC research group at the Victoria University [LC T05].

## 5.3 Performance and Systematics

### 5.3.1 Resolution Results

In this section, point resolution results of data measured in a 0 T, 1 T, 2 T and 4 T magnetic field for different setups are presented. Four fit methods have been used: The Chi Squared Method with and without use of the Pad Response Correction and the Global Fit Method with the width of the charge cloud $\sigma$ as a free fit parameter and with $\sigma$ being fixed to the value resulting from a diffusion coefficient calculated with a Monte Carlo simulation.

All fit methods have been set to fit a curved track hypothesis to the data, even in the case of a 0 T magnetic field, to make the results comparable. The Chi Squared Method without use of the PRC is included to show the effects of the pad response unfolding in the other methods and to illustrate the diffusion limits. The resolution values are plotted in dependency on the drift length.

The reconstruction process of all fits included eight pad rows and the resolution has been calculated from the inner six rows. The decision to include all eight pad rows in the fit and the resolution calculation has been made, because the Global Fit Method with $\sigma$ as a free parameter has four free parameters in the fit function. If one excludes the outer rows on the top and the bottom of the pad plane, only six measurement points are available. In the residual calculation one measurement point is excluded in the refitting of the track. So in this case there are four parameters and at most five data points.
If one or more hit coordinates have a large error, for example because of a damaged pad next to them, the fit becomes unstable. This lowers the efficiency and has an impact on the reliability of the fitting procedure, producing too good results for the residuals.
However, the top and bottom pad rows have the problem of cross-talk between them and the metal plane surrounding the sensitive area (see Section 3.2). This causes the effect that the signals on the outer pads are usually measured earlier than the signals on the inner pads and show a broader structure, which leads to a less accurate and reliable hit reconstruction. Resulting from this the track fit and the distance and residual calculation are less accurate and reliable. The calculated point resolution is probably worse than the one that could be reached for a given method with a setup without the cross-talk.

Figure 5.29 shows the result for a staggered pad layout and P5 gas. Except for the Chi Squared fit without the PRC, for which no correct results are expected in high magnetic fields, all fit methods give similar results. Except for very short drift distances, the resolution results in a magnetic

field of 4 T are independent of the drift distance (respectively the signal width). This indicates that the values are limited mainly by the pad size and probably by the problematic signals on the top and bottom row.

The small increase of the resolution values of the Chi Squared Method with PRC below a drift length of 100 mm show that the charge sharing in this region is too small for a correct Pad Response Correction in all cases. At 4 T, a point resolution of about 150 $\mu$m can be reached.

At lower magnetic fields ($\leq$2 T) the results of the Chi Squared Method with PRC and the Global Fit Method are nearly the same and show the expected dependency on the drift length. At 0 T the diffusion and charge sharing are large enough and even the Chi Squared Method without PRC agrees with the other methods.

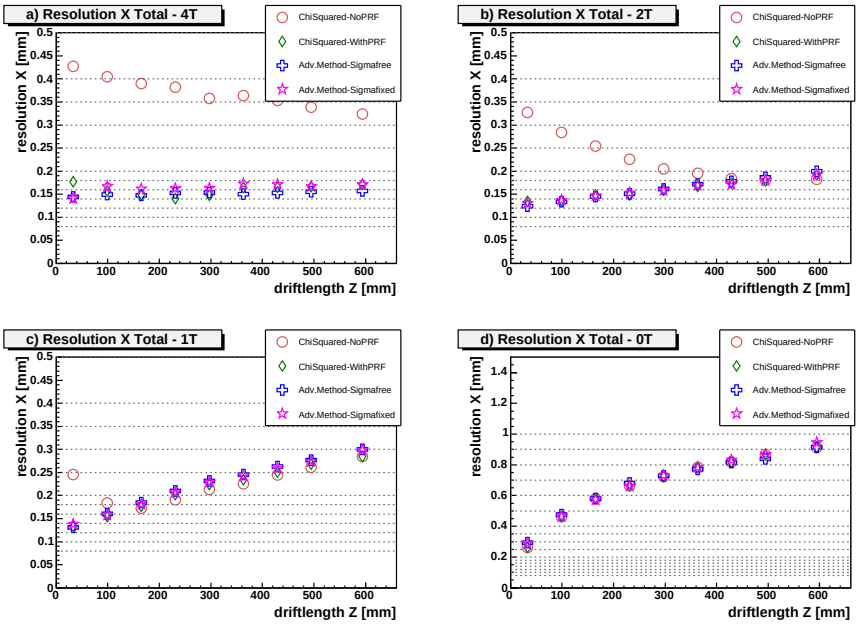


Figure 5.29: Point resolution for P5 gas with staggered pad layout.
Fit methods: Chi Squared fit with (green diamonds) and without (red circles) PRC unfolding and Global Fit with $\sigma$ free (blue crosses) and $\sigma$ fixed (purple stars).

The point resolution for a staggered pad layout and TDR gas is shown in Figure 5.30. At a magnetic field of 4 T, the dependency on the drift length at short drift distances is much stronger than in P5 gas, which was expected from the diffusion and defocussing properties of both gas mixtures (see Table 3.1 in Section 3.2).

Below a drift length of about 250 mm, the charge sharing in a 4 T magnetic field is too small for a accurate correction of the hit positions. In this region, a comparison between the Global Fit with a free $\sigma$ and the Chi Squared Method with PRC indicates that the hit position correction works better in the Global Fit Method. This seems reasonable since the PRC uses simulated values – which most likely do not match the data perfectly – to calculate the width of the charge deposition, while the Global Fit reconstructs the width during the fit to the data.
For the The Global Fit with a fixed $\sigma$, the small increase at 100 mm combined with the decrease at the shortest drift distance encourages the assumption that the results at very short drift distances are too small and not realistic. This assumption is endorsed by the comparison with the other methods.

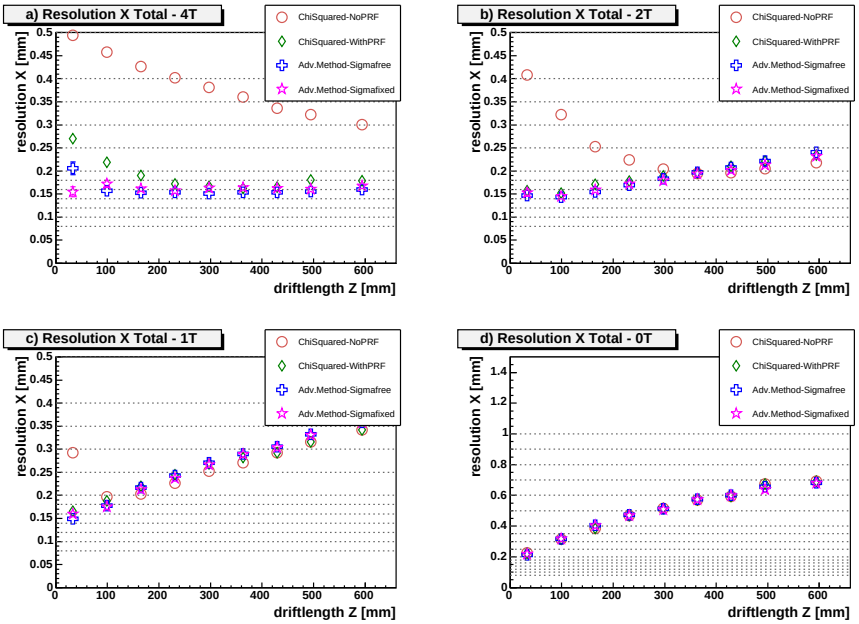


Figure 5.30: Point resolution for TDR gas with staggered pad layout.
Fit methods: Chi Squared fit with (green diamonds) and without (red circles) PRC unfolding and Global Fit with $\sigma$ free (blue crosses) and $\sigma$ fixed (purple stars).

In Figure 5.31 the point resolution for TDR gas and a non-staggered Pad Layout are shown. As expected, following the argumentation in Section 5.1.2 (Figure 5.5), the resolution values for a small charge charing are lower than in the case of a staggered pad layout. This can be clearly seen at short drift lengths in the plot for a 4 T magnetic field.

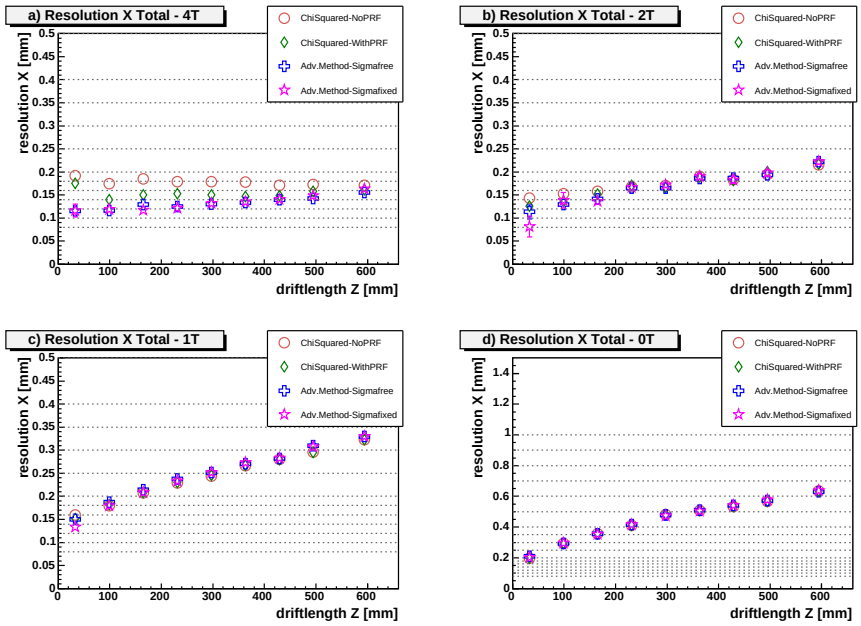


Figure 5.31: Point resolution for TDR gas with non-staggered pad layout. Fit methods: Chi Squared fit with (green diamonds) and without (red circles) PRC unfolding and Global Fit with $\sigma$ free (blue crosses) and $\sigma$ fixed (purple stars).

A possible assumption is, that realistic point resolution values lie in between the results of the calculation with eight and six pad rows. Therefore the results of a fit and resolution calculation including only the inner six pad rows for the reconstruction are shown in Figure 5.32 for all three measurement setups at a 4 T magnetic field (the resolution results for the other magnetic field strengths are shown in Appendix B). The comparison shows that the resolution values with six rows are in some cases a few 10 $\mu$m better and show in general a stronger dependency on the signal width respectively the drift distance.
Especially the Global Fit with six rows shows at short drift distances results well below 100 $\mu$m. Taking the results of the other fit methods and the ratio of free parameters to data points into account, the values do not seem very reliable and support the assumption that they are probably too optimistic.

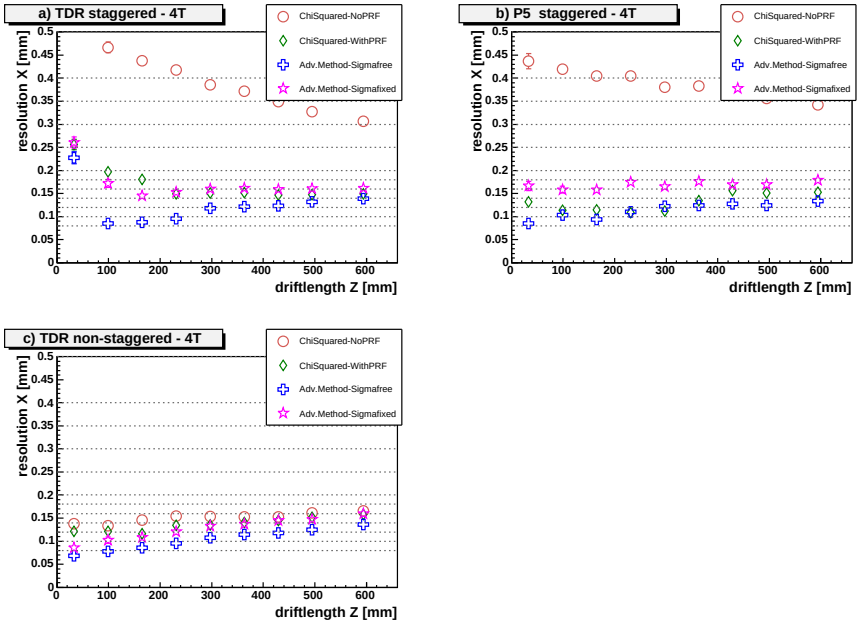


Figure 5.32: Point resolution for 6 rows at 4T for P5 gas with staggered pad layout and TDR gas with staggered and non-staggered pad layout.
Fit methods: Chi Squared fit with (green diamonds) and without (red circles) PRC unfolding and Global Fit with $\sigma$ free (blue crosses) and $\sigma$ fixed (purple stars).

### 5.3.2 Damaged Pads

To analyze how strong the effect of damaged pads on the point resolution is, the data of the Monte Carlo simulation for P5 gas, a staggered pad layout and a magnetic field of 4 T have been used. The Chi Squared Method with PRC and the Global Fit Method with and without a fixed $\sigma$ have been run for a setup where all pads were working. Additionally this has been done for a setup where the same five pad positions were marked damaged, on which there have been damaged pads in the measurement run with P5 gas. This has been done each for a straight and a curved track hypothesis.
The results are shown in Figure 5.33 (here the resolution axis has been scaled by the factor 0.5 in comparison to the previous figures). One can see that with damaged pads, the resolution results are about 10 to 20 $\mu$m worse than without damaged pads.
The numerical values of the calculated resolution probably do not reflect the reality, but they may give an estimation as to which resolution values

are possible with the different methods, if data from a better measurement is used. This assumption is supported by the fact, that the values of the Monte Carlo analysis are in the regime of the resolution values of the measured data, that has been calculated with six rows (see Figure 5.32 in the previous section).

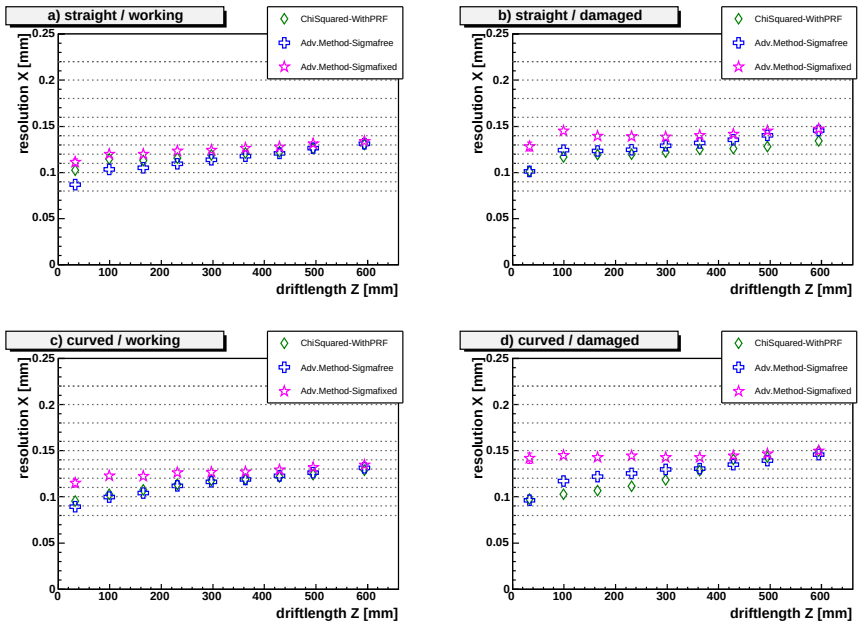


Figure 5.33: Point resolution for Monte Carlo data, calculated with straight and curved track hypothesis, each with and without pads marked as damaged.
Fit methods: Chi Squared fit with PRC unfolding (green diamonds) and Global Fit with $\sigma$ free (blue crosses) and $\sigma$ fixed (purple stars).

### 5.3.3 Number of Pad Rows

The Monte Carlo simulation has also been used to examine the effect of more pad rows on the fit and the point resolution. Therefore an analysis run with the four fit methods has been done using once the information of all nineteen and once only of eight pad rows. In the analysis a curved track hypothesis has been fitted to the Monte Carlo data. This has been done for a 2 and 4 T magnetic field. The resulting point resolution is shown in Figure 5.34.

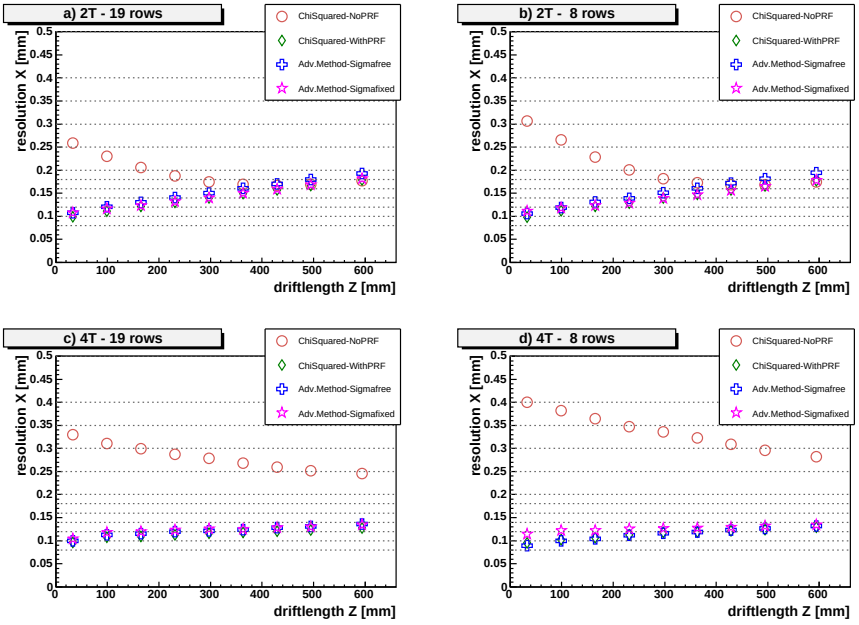


Figure 5.34: Point resolution for Monte Carlo data with 8 and 19 pad rows, for 2 and 4 T, calculated with curved track hypothesis.
Fit methods: Chi Squared fit with (green diamonds) and without (red circles) PRC unfolding and Global Fit with $\sigma$ free (blue crosses) and $\sigma$ fixed (purple stars).

In the case of a magnetic field of 2 T the effect is – except for the Chi Squared fit without PRC – marginal. The results of the Global Method with a free $\sigma$ are a little closer to the results fitted with a fixed $\sigma$. Since for the Monte Carlo data the diffusion and the defocussing are well known, the fit with the fixed $\sigma$ should reproduce accurate results. This leads to the conclusion that the fit with the free $\sigma$ runs more stable with more pad rows. The Chi Squared Fit with PRC shows the same results with eight and nineteen pad rows.

The results for a magnetic field of 4 T show that with more rows, the results of the Chi Squared Fit with PRC and the Global Fit with a free $\sigma$ get a little worse at shorter drift distances. At the same time the results of the Global Fit with a fixed $\sigma$ get a little better. So with nineteen rows, the three results show a better agreement than in the case of eight rows. This shows that the use of more rows stabilizes these three fit methods and leads to more accurate results.

The comparison shows that with more pad rows the resolution results get more reliable. Here, one should keep in mind that the Monte Carlo data reproduce a perfect measurement. In real data, the effects of more rows are probably stronger since the measured data contain irregularities which have a large impact on the reconstruction process if only a few measurement points are available.

## 5.4 Edge Effects

Figure 5.35 shows the Intercept $X_0$ of a Monte Carlo simulation for P5 gas, a 4T magnetic field and eight rows. Four track fitting methods have been used: The Chi Squared Method with and without use of the Pad Response Correction and the Global Fit Method with the width of the charge cloud $\sigma$ as a free fit parameter and with $\sigma$ being fixed to the value resulting from a diffusion coefficient calculated with a Monte Carlo simulation.

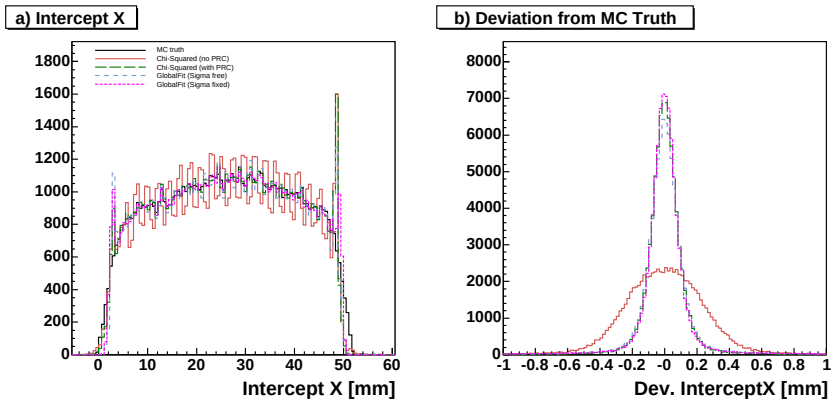


Figure 5.35: Intercept $X_0$ of two Chi Squared fits with (green, long dashed) and without (red, solid) PRC unfolding and of two Global Method fits with $\sigma$ free (blue, dashed) and $\sigma$ fixed (purple, short dashed):
a) comparison of fit results with the Monte Carlo truth (black)
b) deviation of reconstructed values from the Monte Carlo truth.

In the left figure, 5.35.a, two high peaks at the left (2.2 mm) and the right edge (50.6 mm) of the sensitive volume are visible.
These peaks are the results of wrongly reconstructed hits: Hits, whose center is lying near the pad plane, naturally produce signals only inside the pad area. So only this part of the charge cloud is used in the reconstruction and these hit positions are being reconstructed inside the pad area on the pads next to the edges. The angles of these tracks are therefore being recon-

structed to values around zero. This is the reason for the two large peaks in the Intercept $X_0$ distribution and the peak at zero degree in the Slope X distribution shown in Figure 5.36.a.

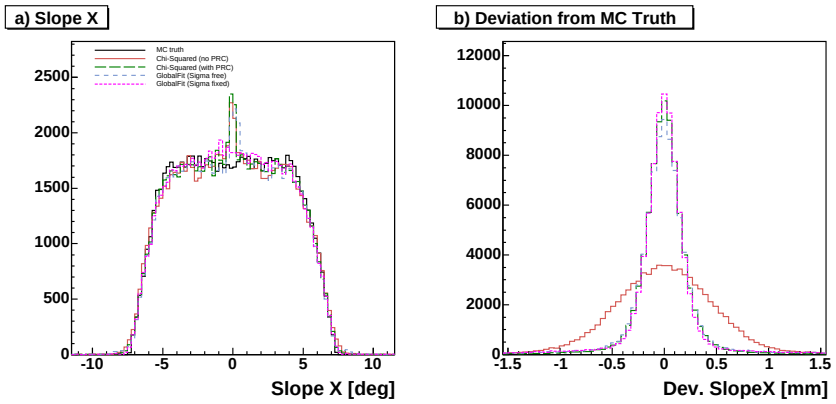


Figure 5.36: Slope X of Chi Squared fit with (green, long dashed) and without (red, solid) PRC unfolding and of Global Fit with $\sigma$ free (blue, dashed) and $\sigma$ fixed (purple, short dashed); 8 rows used for the fit:
a) comparison of both fits with the Monte Carlo truth (black)
b) deviation of reconstructed values from the Monte Carlo truth.

This edge effect is also illustrated in Figure 5.37. Figure 5.37.a shows the Slope X distribution at the edges of the pad plane and takes only tracks into account, for which the Monte Carlo tracks lie completely on the outer two pad columns on both sides. In Figure 5.37.b only the tracks for which the Monte Carlo tracks lie completely inside a central region excluding the two outer columns have been included.
In the region at the edges of the pad plane, the distributions show the expected disagreement (Figure 5.37.a). The results from all fit methods show a peak at angle values near zero which is not visible in the distribution of the Monte Carlo truth.
Because of the layout of the staggering of the pad plane, with the left edge of the pads in uneven rows at $x = 0.0$ and of the pads in even rows at $x = -1.1$, the peak is not centered exactly at zero, but at slightly smaller angle values. The top and the bottom row, which have the strongest lever arm, cause this effect.

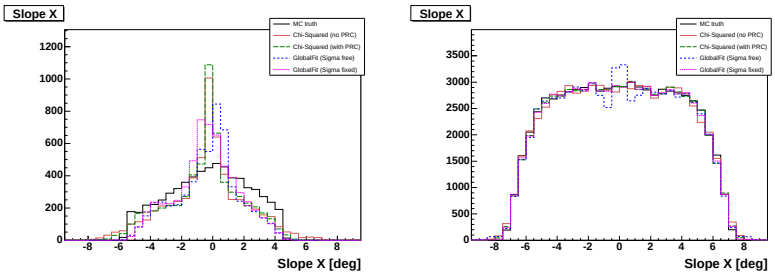


(a) Edge (b) Center

Figure 5.37: Slope X: Monte Carlo truth and fit results for 8 rows at the edge and center of the pad plane.
Chi Squared Fit with (green, long dashed) and without (red, solid) PRC unfolding and of Global Method Fit with $\sigma$ free (blue, dashed) and $\sigma$ fixed (purple, short dashed).

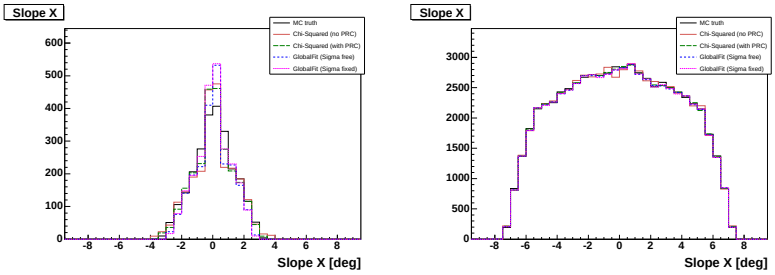


(a) Edge (b) Center

Figure 5.38: Slope X: Monte Carlo truth and fit results for 19 rows at the edge and center of the pad plane.
Chi Squared Fit with (green, long dashed) and without (red, solid) PRC unfolding and of Global Method Fit with $\sigma$ free (blue, dashed) and $\sigma$ fixed (purple, short dashed).

The distributions of the reconstructed values and the Monte Carlo truth show a good agreement in the central region (Figure 5.37.b). The peak at a Slope X of zero, that was clearly visible in Figure 5.36.a has vanished and is only slightly visible for the Global Fit Method with $\sigma$ as a free fit parameter, combined with two small dips on each side. This effect does not vanish if a broader edge region is chosen, which indicates that the Global Fit with a free $\sigma$ does reconstruct some tracks with an angle near zero incorrectly to a zero angle.

Figure 5.38 shows the same Slope X plots as Figure 5.37, but here all nineteen rows have been used in the reconstruction. In the plot for the central region, the peak at zero in the distribution of the Global Fit with a free $\sigma$ has vanished. This indicates that with only eight rows the ratio of free parameters to data points is not good enough for a reliable fit in all cases.

In the following, the efficiency of the fit methods in the edge regions is studied. Here, the efficiency of a fit method is given by how many tracks that have been found in the TrackFinder module are successfully fitted in the TrackFitter module.
In the central region, the fit efficiencies of all methods are good: Both Chi Squared Methods have an efficiency of 100.0±0 %[16]. The Global Fit Method has an efficiency of 99.6 % for $\sigma$ free and 99.8 % for $\sigma$ fixed (the statistical errors of both values are much smaller than 0.1 %). At the edges of the pad plane the efficiencies of the Chi Squared fits stays at 100 %. This was to be expected, since in the analysis only tracks with at least six hits have been included, which is enough for a simple Chi Squared fit. The fit efficiency of the Global Fit with a fixed $\sigma$ drops only slightly to 99.6±0.1 % while it decreases significantly for the fit with a free $\sigma$ to 94.5±0.3 %. This indicates that the Global Fit with free $\sigma$ is more sensitive to missing charge information, while the fixed width makes it more stable.

In the final TPC in a large detector the proposed fit methods will be used for tracks which are nearly straight and have a small curvature. Tracks with a high curvature can be reconstructed by simpler and faster methods with enough precision for a sufficient momentum resolution.
Since a complete coverage of the endplates with sensitive areas is not possible, there will be edges in this setup, too. So the case that nearly straight tracks run along these edges is possible and the effects in this region should be considered in the reconstruction and analysis process.

[16]The statistical error of an efficiency $\epsilon$ has been calculated by: $\Delta\epsilon = \sqrt{\epsilon(1-\epsilon)/N}$, with $N$ = number of events. Therefore, the error of an efficiency of 100 % is zero.

# Chapter 6

# Conclusion and Outlook

The study showed that both the Chi Squared and the Global Fit Method have the potential to be used in the reconstruction of data from a TPC with GEM amplification. The implementation of the Pad Response Correction in the Chi Squared Method lead to a significant improvement of the reconstruction process. The implementation of the Global Fit Method in MultiFit is now finished and many systematics have been understood.

The current resolution results look promising but are still quite far from the requirements a TPC in the LDC detector is supposed to meet (70 $\mu$m at 10 cm and 190 $\mu$m at 200 cm). The analysis of the measured data and the comparison with the Monte Carlo data shows that the current results – especially at 4 T – are most probably limited by the available data and the setup, meaning pad layout and size as well as the quality of the measurement regarding damaged pads.

New measurement runs are planned for the next months. They will include renewed measurements with the old pad planes with eight rows, in which more care will be taken to avoid and repair damaged pads. Additionally two new pad planes (staggered and non-staggered) with more rows and thinner pads will be used in further measurements. The pad plane will have eighteen rows of which sixteen will be connected to the read-out. Presumably only fourteen of the sixteen rows will be covered by the amplification structure due to the dimensions of the used GEMs. This leads to twelve to fourteen rows which can be used in the analysis. The pads will have a size of $1.12 \times 6.835$ mm and a pitch of $1.27 \times 6.985$ mm, which allows forty-eight sensitive pads per row.

Based on this data, many of the analyses presented in this work will be repeated. The availability of more data points in the measurement will probably lead to a more stable and accurate track fitting. With these data

more reliable resolution results and a better comparison of the performance and limits of the different reconstruction methods will be possible.

In the new measurements, a slow-control system [Sch05] will be included for the first time. This system measures slow changing environment parameters like water and oxygen content in the drift gas, pressure and temperature in- and outside the TPC prototype and the electric fields. The data from this system will help in the understanding of the data properties and help in the adjustment of the Monte Carlo simulation to the measurement.
Also, a new laser system will be tested: a laser ray can be shot into the prototype and is aligned by reflection on a movable mirror inside the TPC. This gives the possibility to measure well-known trajectories.

On a larger time scale the construction of a large TPC prototype including a large magnet test setup is planned. With this detector it will be possible to study the effects of a larger drift length and larger GEM and readout structures. The construction of this prototype will improve the understanding of the requirements on the field cage and the construction techniques.

# Appendix A

# Residuals for Different Noise Values in Global Fit

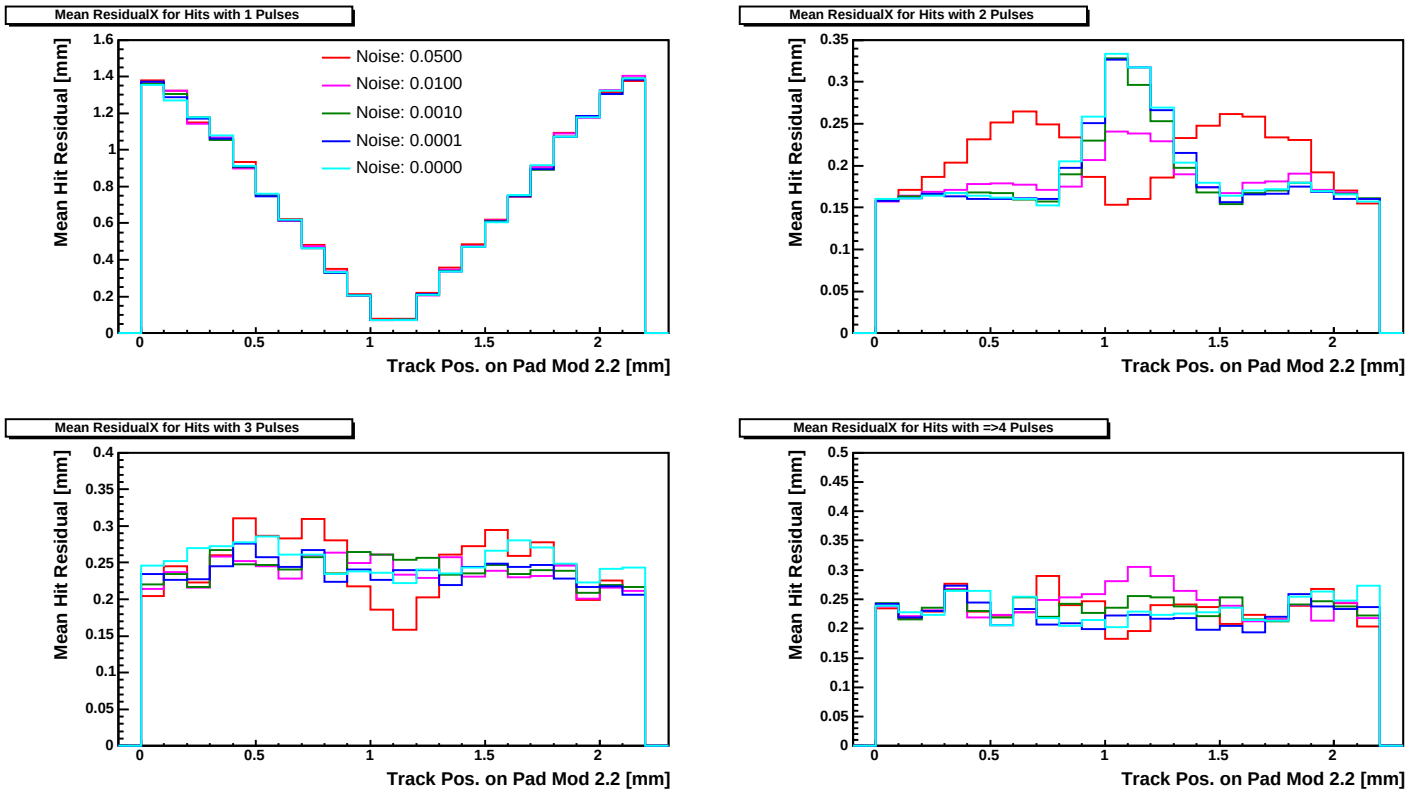


Figure A.1: Mean hit residual in dependency on the track position relative to a pad for different noise factor values ($\sigma$ fixed).

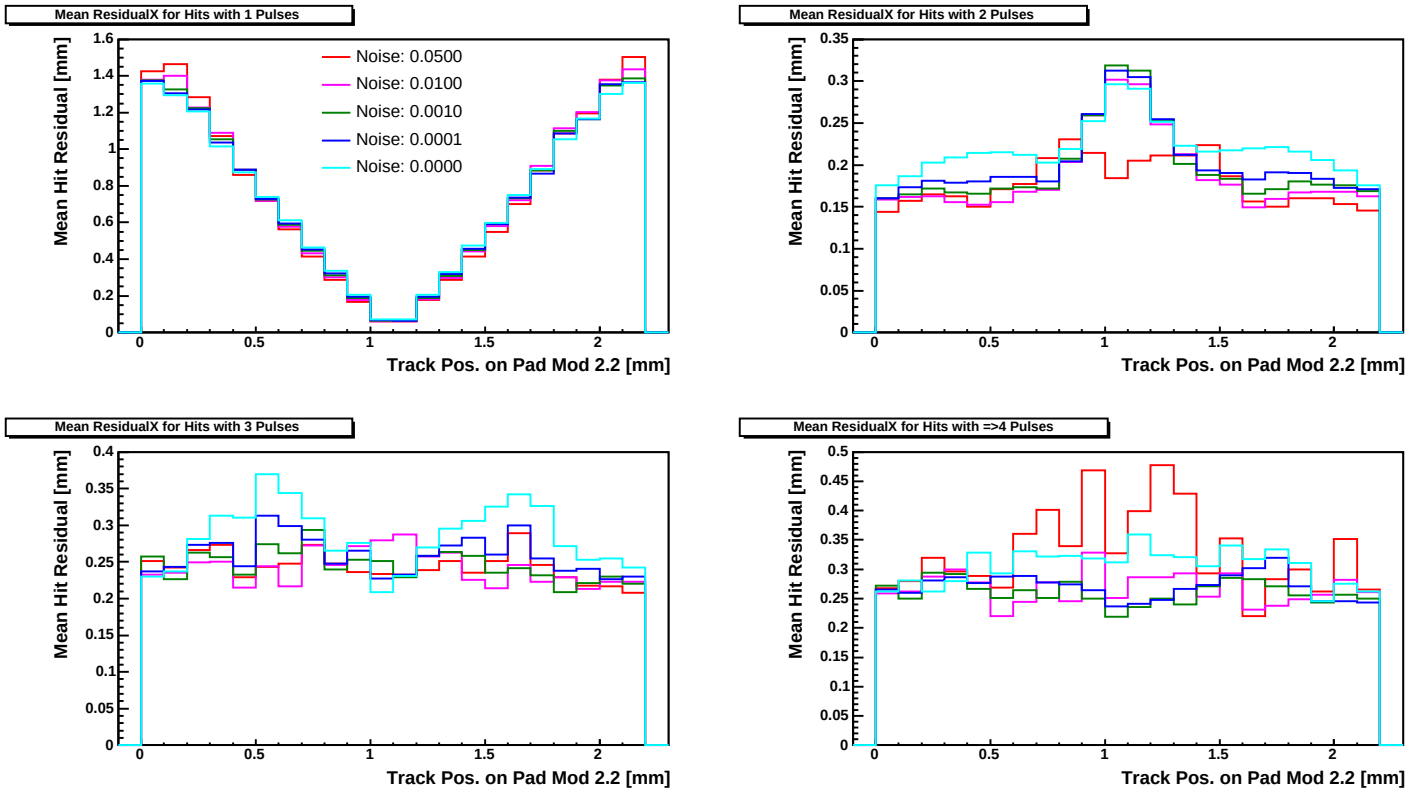


Figure A.2: Mean hit residual in dependency on the track position relative to a pad for different noise factor values ($\sigma$ free).

# Appendix B

# Point Resolution for Fit with 6 Pad Rows

Fit methods: Chi Squared fit with (green diamonds) and without (red circles) PRC unfolding and Global Fit with $\sigma$ free (blue crosses) and $\sigma$ fixed (purple stars).

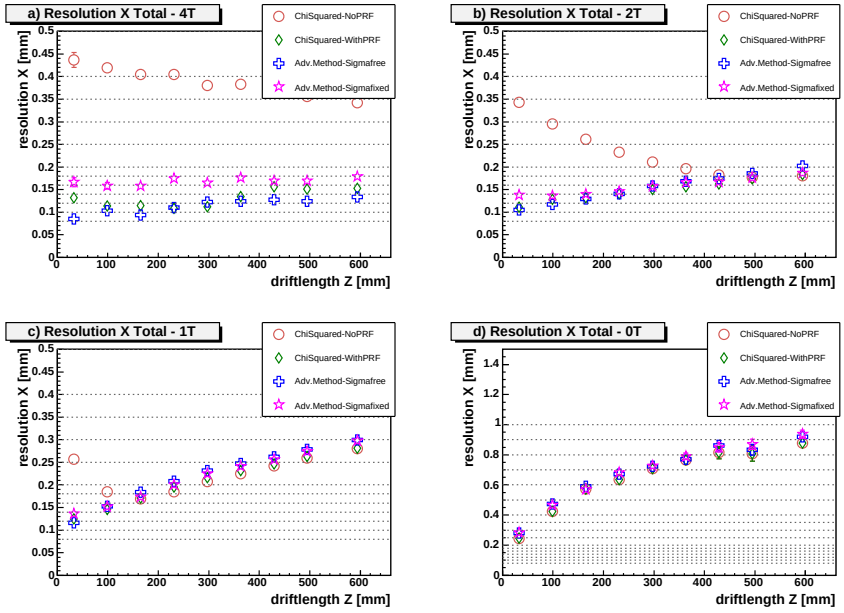


Figure B.1: Point resolution for P5 gas with staggered pad layout.

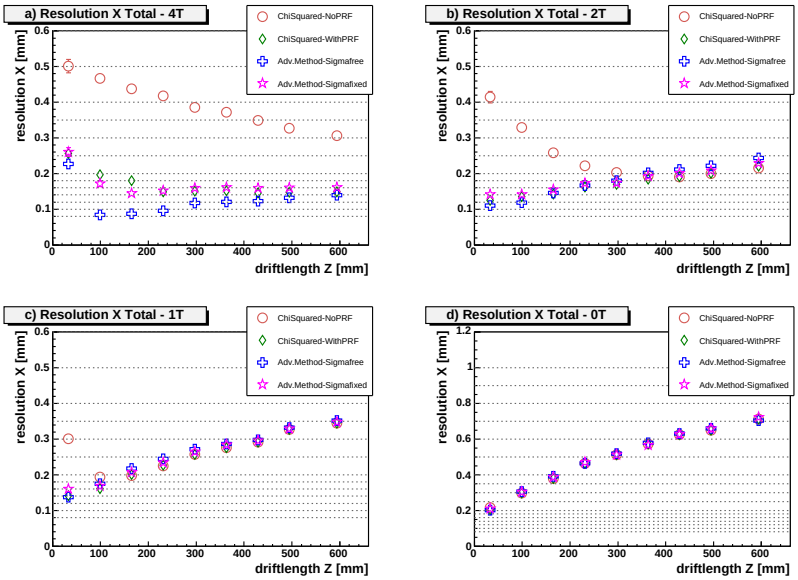


Figure B.2: Point resolution for TDR gas with staggered pad layout.

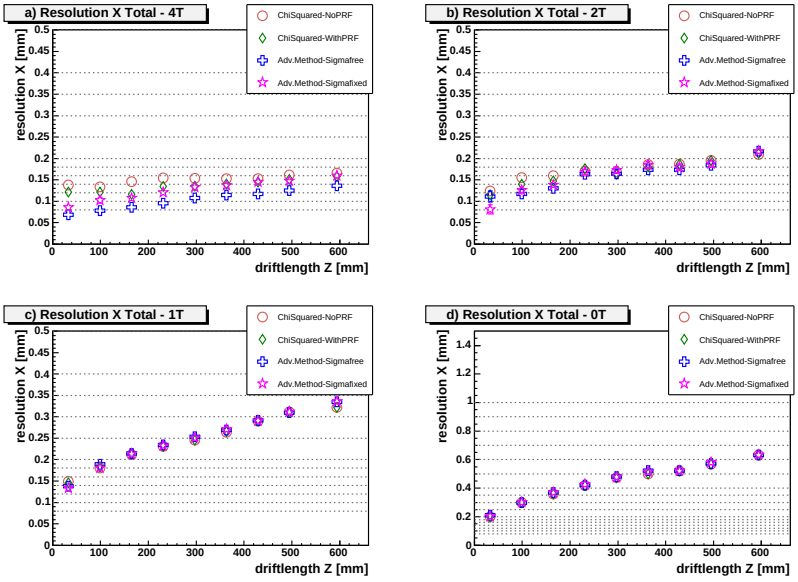


Figure B.3: Point resolution for TDR gas with non-staggered pad layout.

# List of Figures

# List of Tables

# Bibliography


[4th 05] Homepage: 4th Detector Concept, 2005, http://www.physics.iastate.edu/ilc/.

[ACPP] U. ANSOFT Co. Pittsburgh PA, MAXWELL 2D/3D Electric Field Simulator.

[ALEPH95] D. Buskulic et al. (ALEPH Collaboration), *Performance of the ALEPH detector at LEP*, Nucl. Instrum. Meth. **A360**, 481–506 (1995).

[ALEPH03] R. Barate et al. (ALEPH Collaboration), *Search for the standard model Higgs boson at LEP*, Phys. Lett. **B565**, 61–75 (2003), hep-ex/0306033.

[B$^+$80] A. Breskin et al., *High flux Operation of the Gated Multistep Avalanche Chamber*, Nucl. Instr. Meth. **178**, 11 (1980).

[B$^+$00] S. Bachmann et al., *Development and applications of the Gas Electron Multiplier*, Nucl. Instrum. Meth. **A471**, 115–119 (2000).

[Bar05] B. Barish, The ILC Global Design Effort, web, august 2005, http://www.linearcollider.org/pdf/EPP2010 08-02-05.pdf.

[BBSV03] A. Bondar, A. Buzulutskov, L. Shekhtman and A. Vasiljev, *Study of Ion Feedback in Multi-GEM Structures*, Nucl. Instrum. Meth. **A496**, 325–332 (2003).

[BHS05] G. Bertone, D. Hooper and J. Silk, *Particle Dark Matter: Evidence, Candidates and Constraints*, Physics Reports **405**, 279 (2005).

[Bia99] S. F. Biagi, *Monte Carlo simulation of electron drift and diffusion in counting gases under the influence of electric and magnetic fields*, Nuclear Instruments and Methods in Physics Research Section A: Accelerators, Spectrometers, Detectors and Associated Equipment, Vol. 421, Issues 1-2 (January 1999).

[Bic70] H. Bichsel, *Straggling of Heavy Charged Particles: Comparison of Born Hydrogenic-Wave-Function Approximation with Free-Electron Approximation*, Phys. Rev. B **1**, 28542862 (1970).

[Bic88] H. Bichsel, *STRAGGLING IN THIN SILICON DETECTORS*, Rev. Mod. Phys. **60**, 663–699 (1988).

[Bic06] H. Bichsel, *A method to improve tracking and particle identification in TPCs and silicon detectors*, Nuclear Instruments and Methods in Physics Research Section A (April 2006), Article in print.

[BL50] O. Blunck and S. Leisegang, *Zum Energieverlust schneller Elektronen in dünnen Schichten*, Zeitschrift für Physik 128 (1950).

[BNJW04] M. Ball, G. Nabil, M. E. Janssen and P. Wienemann, *A DAQ System for Linear Collider TPC Prototypes based on the ALEPH TPC Electronics*, (2004), LC-DET-2004-013, `http://www-flc.desy.de/lcnotes/`.

[Bow95] C. K. Bowdery, editor, *ALEPH Handbook*, volume 1, CERN, 2 edition, 1995.

[BR93] W. Blum and L. Rolandi, *Particle Detection with Drift Chambers*, Springer, 1993.

[Bri] M. P. Bringle, *Cosmic ray muon Monte Carlo generator using the hemisphere method*, SLAC-BABAR-NOTE-163.

[BS75] H. Bichsel and R. Saxon, *Comparison of calculational Methods for straggling in thin Absorbers*, Physical Review A 11 (1975).

[C+05] R. K. Carnegie et al., *Resolution studies of cosmic-ray tracks in a TPC with GEM readout*, Nucl. Instrum. Meth. **A538**, 372–383 (2005), physics/0402054.

[CERN05] Homepage: CERN, 2005, http://www.cern.ch.

[Col01] T. Collaboration, TESLA Technical Design Report, Technical Report DESY 2001 - 011, DESY, Notkestra"se 85, 22607 Hamburg, Germany, March 2001.

[DESY05] Homepage: DESY, 2005, http://www.desy.de.

[Dre96] M. Drees, *An introduction to supersymmetry*, (1996), hep-ph/9611409.

[EB64] F. Englert and R. Brout, *Broken Symmetry and the Mass of Gauge Vector Mesons*, Phys. Rev. Lett **13**, 321–322 (1964).

[EKM77] V. Ermilova, L. Kotenko and G. Merzon, *Fluctuations and the most probable values of relativistic charged particle energy loss in thin gas layers*, Nuclear Instruments and Methods 145 (1977).

[Fan46] U. Fano, *On the theory of ionization yield of radiations in different substances*, Phys. Rev. 70 (1 & 2) **70** (1946).

[Fan47] U. Fano, *Ionization yield of radiations ii. the fluctuation of the number of ions*, Phys. Rev. 72 (1) **72** (1947).

[Gar05] E. Garutti, Talk, 2005, IFAE - Incontri di Fisica delle Alte Energie.

[GC] GDD-CERN, Homepage: Gas Detectors Development Group, http://gdd.web.cern.ch/GDD/.

[GHK64] G. S. Guralnik, C. R. Hagen and T. W. B. Kibble, *Global Conservation Laws and Massless Particles*, Phys. Rev. Lett. **13**, 585–587 (1964).

[GLD05] Homepage: GLD, 2005, http://ilcphys.kek.jp/gld/.

[Glu63] R. L. Gluckstern, *Uncertainties in track momentum and direction, due to multiple scattering and measurement errors*, Nucl. Instrum. Meth. **24**, 381–389 (1963).

[Gri87] D. J. Griffith, *Introduction to Elementary Particles*, John Wiley & Sons, Inc., United States of America, 1987.

[GRRC96] Y. Giomataris, P. Rebourgeard, J. P. Robert and G. Charpak, *Micromegas: A High-Granularity Position-Sensitive Gaseous Detector for High Particle-Flux Environments*, Nucl. Instrum. Meth. **A376**, 29–35 (1996).

[Hig64a] P. W. Higgs, *Broken Symmetries and the Masses of Gauge Bosons*, Phys. Rev. Lett. **13**, 508–509 (1964).

[Hig64b] P. W. Higgs, *Broken Symmetries, Massless Particles and Gauge Fields*, Phys. Lett. **12**, 132–133 (1964).

[Hig66] P. W. Higgs, *Spontneous Symmetry Breakdown without Massless Bosons*, Phys. Rev. **145**, 1156–1163 (1966).

[HKC+98] D. Heck, J. Knapp, J. Capdevielle, G. Schatz and T. Thouw, *Corsica:A Monte Carlo Code to Simulate Extensive Air Showers*, Wissenschaftliche Berichte FZKA 6019, Forschungszentrum Karlsruhe (1998).

[HLS75] R. Haag, J. T. Lopuszański and M. Sohnius, *All possible generators of supersymmetries of the S-matrix*, Nuclear Physics B **88**, 257–274 (March 1975).

[ILC06] ILC, Homepage: ILC, 2006, http://www.linearcollider.org.

[Imh06] A. Imhof, Private Communication, 2006.

[Jan04] M. Janssen, Auflösungsstudien an einer Zeit-Projektions-Kammer (TPC) mit GEM Gasverstärkunssystem, December 2004, DESY-THESIS-2004-049.

[Jan06] M. Janssen, Private Communication, 2005/2006.

[K+04] M. Killenberg et al., *Charge transfer and charge broadening of GEM structures in high magnetic fields*, Nucl. Instrum. Meth. **A530**, 251–257 (2004).

[Kar05] D. Karlen, Homepage: Karlen, D., 2005, http://particle.phys.uvic.ca/ karlen/.

[Kaz00] D. I. Kazakov, *Beyond the standard model (in search of supersymmetry)*, (2000), hep-ph/0012288.

[KEK05] Homepage: KEK, 2005, http://www.kek.jp.

[KPR05] D. Karlen, P. Poffenberger and G. Rosenbaum, *TPC Performance in Magnetic Fields with GEM and Pad Readout*, NUCL.INSTRUM.METH.A **555**, 80 (2005).

[Lan44] L. Landau, *On the energy loss of fast particles by ionization*, J. Phys. USSR 8 (1944).

[LC T05] Homepage: LC TPC RnD of University of Victoria, Canada, 2005, http://www.linearcollider.ca/groups/uvic/.

[LCIO05] Homepage: LCIO - data model for ILC detector studies, DESY, D, 2005, http://lcio.desy.de/.

[LDC05] Homepage: LDC, 2005, http://www.ilcldc.org/.

[LE05] LEP-EWWG, Homepage: The LEP Electroweak Working Group, 2005, http://lepewwg.web.cern.ch/LEPEWWG/.

[Leo94] W. R. Leo, *Techniques for Nuclear and Particle Physics Experiments - A How-to Approach*, Springer-Verlag, New York Berlin Heidelberg, 1994, 2nd Edition.

[Lux03] T. Lux, Bau und Test einer Mini-TPC mit GEM-Auslese zur Messung des Ionen-Rückflusses, 2003.

[Lux05] T. Lux, Studies for a Time Projection Chamber for the International Linear Collider and Measurement of Beauty Cross Sections in Deep Inelastic Scattering at HERA, July 2005, DESY-THESIS-2005-019.

[LW92] T. Lohse and W. Witzeling, *The Time Projection Chamber*, Instrumentation in High Energy Physics (Advanced Series on Directions in High Energy Physics - Vol. 9) (June 1992).

[MAGB05] Homepage: MAGBOLTZ, 2005, http://ref.web.cern.ch/ref/CERN/CNL/2000/001/magboltz/.

[Mar97] S. P. Martin, *A supersymmetry primer*, (1997), hep-ph/9709356.

[Nyg] D. R. Nygren, *The Time Projection Chamber: A new 4 Pi Detector for Charged Particles*, PEP-0144.

[Par02] Particle Data Group, *Review of Particle Physics*, Physical Review D **66** (2002).

[Phy05] C. A. Physics, Homepage: Cornell University, Accelerator Physics, 2005, http://w4.lns.cornell.edu/accelphys/index.shtml.

[Ram21] C. Ramsauer, *Über den Wirkungsquerschnitt der Gasmoleküle gegenber langsamen Elektronen*, Annalen der Physik, 4. Folge, 64 , 513–540 (1921).

[ROOT05] Homepage: ROOT - Data Analysis Framework, CERN, CH, 2005, http://root.cern.ch/.

[Sau97] F. Sauli, *GEM: A new concept for electron amplification in gas detectors*, Nucl. Instrum. Meth. **A386**, 531–534 (1997).

[SB64] S. Seltzer and M. Berger, *Energy Loss Straggling and of Protons and Mesons: Tabulations of the Vavilov Distribution*, National Academy of Sciences Publication, Nuclear Science Series Report No. 39 (1964).

[Sch05] O. Schäfer, Ein Monitorsystem für gasbasierte Detektoren am International Linear Collider, December 2005.

[SiD05] Homepage: SiD, 2005, http://www-sid.slac.stanford.edu/.

[SLAC05] Homepage: SLAC, 2005, http://www.slac.stanford.edu/.

[Smi] I. Smirnov, HEED Simulation Programme for Energy Loss, http://consult.cern.ch/writeup/heed/.

[Sob02] B. Sobloher, Simulationsstudien zu GEM-Folien fr die Auslese einer TPC, March 2002, http://www.physik.rwth-aachen.de/group/IIIphys/TESLA/en/index.html.

[Tal79] R. Talman, *On the Statistics of Particle Identification using Ionization*, Nuclear Instruments and Methods 159 (1979).

[Uni05] C. University, Homepage: Cornell University, 2005, http://www.cornell.edu.

[Vav57] P. Vavilov, *Ionization losses of high-energy particles*, Sov. Phys.-JETP 5 (1957).

[Vee84] R. Veenhof, *GARFIELD - A Drift Chamber Simulation Program*, CERN Program Library W5050 (1984).

[Vee98] R. Veenhof, *GARFIELD, recent developments*, Nucl. Instrum. Meth. **A419**, 726–730 (1998).

[Vict05] Homepage: High Energy Physics, University of Victoria, Canada, 2005, http://particle.phys.uvic.ca/.

[Vog05] A. Vogel, Private Communication, 2005.

[WDH67] E. Wagner, F. Davies and G. Hurst, *Time-of-flight investigations of electron transport in some atomic and molecular gases*, J. Chem. Phys. **47**, 3138 (1967).

[Web03] M. Weber, Simulationen zur Verwendung von GEM-Folien als Auslesemodul einer TPC, October 2003, http://www.physik.rwth-aachen.de/group/IIIphys/TESLA/en/index.html.

[WZ74a] J. Wess and B. Zumino, *A lagrangian model invariant under supergauge transformations*, Physics Letters B **49**, 52–54 (March 1974).

[WZ74b] J. Wess and B. Zumino, *Supergauge transformations in four dimensions*, Nuclear Physics B **70**, 39–50 (February 1974).

## Acknowledgments

This diploma thesis would not have been possible (and would not have been so much fun) without the assistance of numerous people:

First of all, I want to thank Prof. Dr. Rolf-Dieter Heuer and Dr. Ties Behnke for giving me the opportunity to prepare this diploma thesis in the FLC working group at DESY. Furthermore, I want to thank them for the opportunity to attend the ECFA workshop 2005 in Vienna and the DPG Frühjahrstagung 2006 in Dortmund. I want to thank Prof. Dr. Beate Naroska for taking over the part of the second referee.

A tremendous thanks goes to my direct supervisor Dipl.-phys Matthias E. Janssen for his great assistance and for sharing his lexical knowledge (not only regarding physics). Without him, I would have been lost.

In the following, some people are mentioned who laid the groundwork for this thesis: I want to thank again Dipl.-phys Matthias E. Janssen for his always quick debugging of MultiFit and not getting tired of my countless questions regarding the implementations, Dipl.-phys Andreas Imhof for putting a lot of time in producing the used Monte Carlo data, Dr. Thorsten Lux for helping me understand the MediTPC prototype and Dr. Peter Wienemann who gave me my first introduction. Furthermore I want to thank all current and former members of the TPC group for their assistance, the interesting discussions and for always kindly answering my questions.
For proof-reading I want to thank Dr. Ties Behnke, Dipl.-phys Matthias E. Janssen and Dipl.-Übers. Sabine Pfeifer and for a quick last minute proof-reading Dr. Tobias Schlegelmilch.

I want to thank the whole FLC working group: Working in this group was a lot of fun and very inspiring. Due to the size of the group, not all members are listed here by name.

Especially, I want to thank my office mates Dipl.-phys Markus Ball and Dipl.-phys Hendrik Meyer for their good humor, for a great working atmosphere, for their general assistance and for keeping me up-to-date regarding – among other topics – the latest news, comic books, movies and computer matters. Some other members have to mentioned also: Ramona Matthes for taking care of all organizational matters, Dipl.-phys Blanka Sobloher for putting a lot of work into rescuing our measured data and the Monte Carlo simulation from a crashed hard disk raid array, Dr. Steve "*this is not a Landau*" Aplin for inspiring my studies of energy straggling distributions (which unfortunately could not be finished in the scope of this work), Dipl.-phys Adrian Vogel for helping me with Postscript and figure issues (and for baking cakes) and Dr. Roman Pöschl and Dipl.-phys Predrag Krstonosic for interesting conversations.

A special thanks goes to my friends Sabine Henssen and Matthias Krämer who subletted me a room in their flat and made me feel at home during the two and a half months between my last and my current flat and Gerold Berger and his family for letting me store my furniture and stuff in their attic during this time. For keeping my mood up and helping me in numerous ways during the last year I want to thank my friends Tobias Schlegelmilch, Susanne Pfeifer, Frank Sienz, Andreas von Manteuffel, Birgit Eberle, Pascale Kleysteuber, Henning Ruppersberg, Ines Schwang, Karin Nacken, Erik Bartscherer, Jörn Burkhard and all others which I may have forgotten. Additionally, a big thanks to my flatmate Stephan "*Kalle*" Voß and my "*Hamburg and conference night-life guide*" Tania Robens.
And last but definitely not at least, I want to thank my family for supporting me in all possible ways.

**Erklärung**

Hiermit versichere ich, die vorliegende Arbeit selbständig und nur unter Verwendung der angegebenen Quellen und Hilfsmittel verfasst zu haben. Ich gestatte die Veröffentlichung dieser Arbeit.